Universiteit Antwerpen

Master thesis

Renormalization group equations in Quantum Chromodynamics and precision physics at high-energy hadron colliders

Author:
Aaron Lau

Supervisor:
Prof. Dr. Francesco Hautmann

Thesis voorgelegd tot het behalen van
de graad 'Master in de fysica'

Faculteit Wetenschappen
Department Fysica
Academiejaar 2025-2026

Samenvatting

De hadronstructuur vormt één van de belangrijkste bronnen van systematische onzekerheden in theoretische voorspellingen voor fysische grootheden die worden gemeten in huidige experimenten bij hoogenergetische deeltjesversnellers. Om die reden is een aanzienlijk deel van toekomstige hoogenergetische fysica projecten gericht op het verbeteren van onze kennis van de parton-distributiefuncties (PDF's) van hadronen.

Om dezelfde reden wordt er momenteel een grote inspanning geleverd om de perturbatieve nauwkeurigheid van theoretische berekeningen voor de partonstructuur in de kwantumchromodynamica (QCD) uit te breiden, waarbij de huidige grens ligt bij de berekeningen op vier-lusniveau, oftewel next-to-next-to-next-to-leading order (N^3LO) in de QCD-perturbatietheorie.

Met deze sterke toename in precisie worden theoretische systematische onzekerheden die voortkomen uit de perturbatieve oplossing van de renormalisatiegroep vergelijkingen (RGE's) een belangrijke factor in het bepalen van de algehele nauwkeurigheid van theoretische voorspellingen voor processen bij deeltjesbotsingen.

Dit proefschrift onderzoekt een algemene methodologie die recent is voorgesteld om de systematische effecten van RGE's te evalueren, gebaseerd op technieken ontleend aan benaderingen voor zacht-gluon- en transversaal-impulsresommatie in QCD. Na een beschrijving van de belangrijkste concepten van deze methodologie en een samenvatting van de tot nu toe behaalde resultaten, verkent het proefschrift de toepassing ervan op structuurfuncties in diep-inelastische verstrooiing (DIS), die momenteel onze voornaamste bron van kennis vormen over de PDF van het proton.

Er wordt gekeken naar bijdragen aan de RGE-systematiek van DIS-structuurfuncties afkomstig van de QCD-koppeling en van PDF's, waarbij de gevallen van de F_2-structuurfunctie en de longitudinale structuurfunctie F_L afzonderlijk worden besproken, inclusief hoog-precisie resultaten op N^3LO.

Abstract

Hadron structure constitutes one of the main sources of systematic uncertainties in theoretical predictions for physical observables measured in current experiments at high-energy colliders. For this reason, a substantial part of future high-energy physics programs are devoted to improving our knowledge of hadrons' parton distribution functions (PDFs).

Also, for this reason, a major effort is ongoing to extend the perturbative accuracy of theoretical calculations for partonic structure in Quantum Chromodynamics (QCD), for which the frontier is currently the four-loop order, that is, next-to-next-to-next-to-leading order ($\mathrm{N^3LO}$) in QCD perturbation theory.

With this dramatic increase in precision, theoretical systematic uncertainties arising from the perturbative solution of renormalization group equations (RGEs) become an important factor in determining the overall accuracy of theory predictions for collider processes.

This thesis investigates a general methodology which has recently been proposed to evaluate RGE systematic effects, based on using techniques borrowed from soft-gluon and transverse-momentum resummation approaches in QCD. After providing a description of the main concepts of this methodology and a summary of the main results achieved so far, the thesis explores its application to deep inelastic scattering (DIS) structure functions, which are currently our main source of knowledge about proton's PDF.

It analyzes contributions to the RGE systematics on DIS structure functions from the QCD coupling α_s and from PDFs, and discusses separately the cases of the F_2 structure function and of the longitudinal structure function F_L, including high-precision results at $\mathrm{N^3LO}$.

Contents

Acknowledgements

First, I'd like to express my gratitude to Professor Pierre Van Mechelen for giving me the suggestion and opportunity to carry out a master's thesis in the field of particle physics and for being my teacher in courses on particle physics throughout the years. It is a dream and true honour to be a part of such a big research field.

Then, I'd like to thank Ola Lelek and Pieter Taels for guiding me through the early stages of the thesis and checking in on my situation from time to time. Even though the thesis took a different turn than originally planned, they set a good example to follow and taught me a lot about doing research and academics, as well as things outside of academics. Here is also a special thanks to Valerio Bertone for helping me set up everything on the technical side of things and staying in touch for other problems or questions regarding the code.

Next, I want to give many thanks to my supervisor Professor Francesco Hautmann. He was always patient and understanding throughout the whole project and gave me great advice when I needed it. I wouldn't have been able to finish up my thesis if not for his immense help and continuous support.

And finally, I want to thank my friends and family for always being supportive and kind to me during this project.

Introduction

When one wants to find out about the fundamental workings of this world, one comes across many different concepts and theories. However, behind each of those theories lies (at the moment) one theory that is more fundamental than any other one: the Standard Model. This is a theory that aims to describe the building blocks of our world using mathematical concepts and experimental data. What makes this theory special from other such theories is that experiments and theory agree with each other up to extreme precision. This makes it one of the most successful, but also most complicated theories ever, and also based on some of the biggest and most expensive experiments ever, such as high-energy lepton collision and hadron collision experiments.

Despite its success, it is known that at extreme energy scales, the theory still leaves many questions unanswered about fundamental interactions. One of the main avenues to advance in this field is to strive for higher and higher precision, both in experimental measurements and in theoretical predictions, so as to uncover clues to the mysteries still underlying the Standard Model.

At the level of theoretical accuracy currently reached in Standard Model predictions, it becomes very important to develop methods to investigate and control, with high precision, the physical effects associated with the evolution of the coupling constants, and of other fundamental quantities, from low to high energies, spanning a very large energy range. These effects are taken into account by Renormalization Group equation (RGE) methods.

A theoretical framework has recently been proposed to systematically take into account RGE effects in theoretical predictions for physical processes occurring in high-energy collisions via the strong interaction, which is described by the sector of the Standard Model embodied in Quantum Chromodynamics (QCD).

In this thesis we investigate this framework in detail. We apply it to study the role of the RGE systematics for the QCD coupling α_s and for the parton distribution functions (PDFs) in high-precision calculations of the proton's structure functions measured by deep-inelastic scattering (DIS) experiments in high-energy lepton-hadron collisions. The thesis is structured as follows.

In Chapter 1, we give a concise introduction to the basic elements of QCD as the theory of the strong interaction and of the theory of DIS in lepton-hadron collisions.

In Chapter 2, we describe the theoretical framework providing the methodology to evaluate RGE systematic effects, and discuss in detail the cases of the coupling α_s and of the PDF.

In Chapter 3, we turn to high-precision calculations of DIS structure functions. First we compute results at next-to-next-to-leading order (NNLO) in perturbation theory for RGE effects on the F_2 structure function, which is the sum of transversely-polarized and longitudinally-polarized components. Next we examine in more detail these RGE effects

by decomposing them into their α_s and PDF contributions. Then we study separately the transversely-polarized and longitudinally-polarized components of the structure function, particularly with a view to measurements of the longitudinal structure function F_L which will reach good accuracy for the first time at future colliders. Finally we go one order higher in perturbation theory, and present results from the application of the RGE systematics methodology at $\mathrm{N^3LO}$.

Conventions

Before tackling anything in particle physics, a set of conventions must be chosen and fixed.

- The Minkowski metric will be chosen as "mostly minus", which means that the time component is positive, and the spatial components are negative.

$$g_{\mu\nu} = \begin{pmatrix} 1 & 0 & 0 & 0 \\ 0 & -1 & 0 & 0 \\ 0 & 0 & -1 & 0 \\ 0 & 0 & 0 & -1 \end{pmatrix}$$

- The four-gradient is defined as:

$$\partial_\mu = \frac{\partial}{\partial x_\mu} = \left(\frac{\partial}{\partial t}, \nabla\right)$$

- The Dirac slashed notation applied on an object expresses a contraction of that object with the four gamma matrices, as shown below:

$$\not{p} = p_\mu \gamma^\mu = p_0\gamma^0 + p_1\gamma^1 + p_2\gamma^2 + p_3\gamma^3$$

$$\gamma^0 = \begin{pmatrix} 1 & 0 & 0 & 0 \\ 0 & 1 & 0 & 0 \\ 0 & 0 & -1 & 0 \\ 0 & 0 & 0 & -1 \end{pmatrix}, \quad \gamma^1 = \begin{pmatrix} 0 & 0 & 0 & 1 \\ 0 & 0 & 1 & 0 \\ 0 & -1 & 0 & 0 \\ -1 & 0 & 0 & 0 \end{pmatrix},$$

$$\gamma^2 = \begin{pmatrix} 0 & 0 & 0 & -i \\ 0 & 0 & i & 0 \\ 0 & i & 0 & 0 \\ -i & 0 & 0 & 0 \end{pmatrix}, \quad \gamma^3 = \begin{pmatrix} 0 & 0 & 1 & 0 \\ 0 & 0 & 0 & -1 \\ -1 & 0 & 0 & 0 \\ 0 & 1 & 0 & 0 \end{pmatrix}$$

  This set of gamma matrices can be interpreted as a basis in Minkowski space. An additional gamma matrix can be constructed as $\gamma_5 = i\gamma_0\gamma_1\gamma_2\gamma_3$ and represents the chirality operator.

- It is common in particle physics to use natural units. Most quantities will be expressed in GeV (gigaelectronvolt) and the constants $c = \hbar = 1$ will be chosen for ease of calculation and writing. Some useful and frequently used quantities are:

$$\begin{aligned}
[\text{Energy}] &= \text{GeV} \\
[\text{Mass}] &= m_e = \text{GeV}/c^2 = \text{GeV} \\
[\text{Length}] &= \hbar/m_e c = \text{GeV}^{-1} \\
[\text{Time}] &= \hbar/m_e c^2 = \text{GeV}^{-1}
\end{aligned}$$

Chapter 1

Quantum Chromodynamics (QCD) and Deep-Inelastic Scattering (DIS)

In this first chapter, the basics of QCD and DIS will be introduced. QCD describes one of the four fundamental forces of the universe, dealing with the binding of quarks, while DIS describes the scattering process of electrons (or muons and neutrinos) on hadrons (mostly protons and neutrons). This chapter is based on the treatments of QCD and DIS given in the textbooks and lectures [1, 2, 3, 4, 5, 6, 7, 8, 9, 10, 11, 12].

1.1 QCD as the theory of the strong interactions

QCD is a part of the Standard Model of fundamental interactions. The Standard Model is a field theory based on quarks and leptons as matter particles and different gauge symmetries of the lagrangian density. These are described by symmetry groups. The properties (more specifically, the Lie algebra) of these groups give rise to the force carriers that we know of in the Standard Model, as displayed in figure 1.1. The strong force corresponds to a SU(3) symmetry with gluons as mediators; the weak force to a SU(2) symmetry with the W/Z bosons; and the electromagnetic force to a U(1) symmetry with the photons. Gravity is, at the moment, still not part of the Standard Model. The strong force is responsible for nuclear interactions inside of atoms.

The Lagrangian density for QCD can be written as

$$\mathscr{L}_{QCD} = \sum_f \bar{\psi}_f (i\not{D} - m_f)\psi_f - \frac{1}{4}F^a_{\mu\nu}F^{a\mu\nu} - \frac{1}{2\xi}(\partial_\mu A^{\mu a})^2 - \bar{c}^a \partial_\mu D^\mu_{ab} c^b \tag{1.1}$$

Here follows a quick intuitive overview of the different terms in this expression: the first one is a term for kinetic energy and mass of Dirac fields and their interactions with gauge bosons, the second one is purely a term for kinetic energy of gauge bosons (similar to the EM field strength) and their self-interactions, the third one is a gauge-fixing term (therefore breaking gauge symmetry) that is needed to be able to quantize the theory, the fourth is a ghost term that is a consequence of gauge-fixing a non-abelian theory.

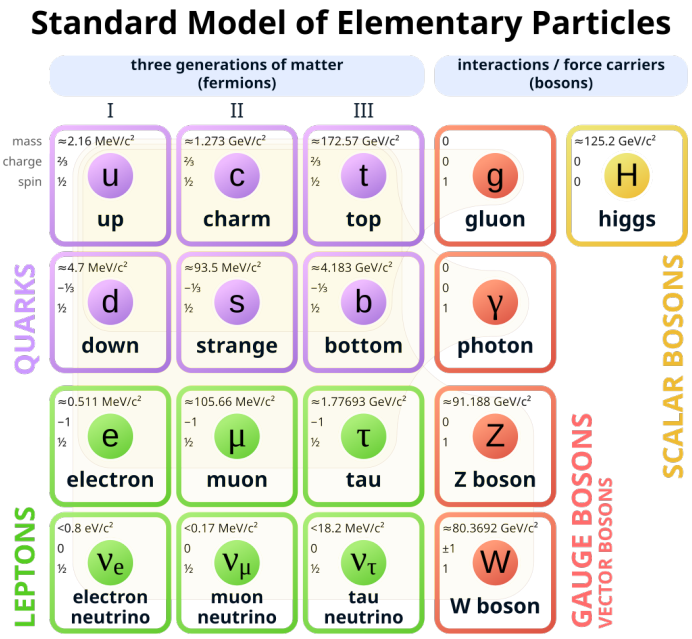

Figure 1.1: The picture of the Standard Model is divided into multiple parts: the particles (quarks and leptons), force carriers (gauge bosons) and the higgs particle (scalar boson), from [13]

1.1.1 Building blocks of QCD

QCD is based on a non-abelian gauge theory of fermion fields (the quarks) with a SU(3) symmetry. As for any gauge theory, the standard Lagrangian density of a Dirac field (when working with fermions) needs to be transformed into one that is gauge-invariant by implementing the so-called "covariant derivative", denoted by the letter D. The way this happens depends on the symmetry group of the theory.

A SU(3) local symmetry means that the following gauge transformation keeps the Lagrangian density invariant:

$$\psi(x) \to \psi'(x) = \psi(x) e^{i\alpha_j(x) T_j} \tag{1.2}$$

where $T_j = \lambda_j/2$ and λ_j are the Gell-Mann matrices, or the generators of the SU(3) group, $\alpha_j(x)$ is a spacetime-dependent phase factor and $\psi(x)$ is a fermionic field.

After applying this transformation naively to the classical Lagrangian density for a Dirac field, a problematic term appears:

$$\begin{aligned} \mathscr{L}_{Dirac} &= \bar{\psi}(x)(i\partial\!\!\!/ - m)\psi(x) \\ &\downarrow \\ \mathscr{L}'_{Dirac} &= \bar{\psi}'(x)\left(i\partial\!\!\!/ - m\right)\psi'(x) \\ &= \bar{\psi}(x) e^{-i\alpha_j(x)T_j}\left(i\partial\!\!\!/ - m\right)\psi(x) e^{i\alpha_j(x)T_j} \\ &= \bar{\psi}(x)\left(i\partial\!\!\!/ - m\right)\psi(x) - \bar{\psi}(x)\partial\!\!\!/\alpha_j(x) T_j \psi(x) \end{aligned} \tag{1.3}$$

The trick to getting rid of the last extra term is to introduce the covariant derivative with **new vector fields** and the appropriate field transformations. In the general case, the covariant derivative and the field transformation is given by

$$\begin{aligned} D_\mu &= \partial_\mu - igA^a_\mu(x)T^a \\ A^a_\mu &\to A^a_\mu + \frac{1}{g}\partial_\mu\alpha^a - f^{abc}\alpha^b A^c_\mu \end{aligned} \tag{1.4}$$

where g will be made clear to be the coupling constant, A^a_μ are the newly introduced vector fields (the gluons), T^a the generators of the group running over the index a and f^{abc} the structure constants of the group. After substituting the normal derivative with the covariant derivative, the expression becomes

$$\begin{aligned} \mathscr{L}_{QCD} &\supset \bar{\psi}(x)(i\not{D} - m)\psi(x) \\ &= \bar{\psi}(x)\left(i\not{\partial} - m\right)\psi(x) - \bar{\psi}(x)\not{\partial}\alpha_j(x)T_j\psi(x) \end{aligned} \tag{1.5}$$

Now that gluon fields have been added to the Lagrangian density, other potential terms involving these fields also need to be added. One such term is a gauge-invariant term containing the kinetic energy of the gluon fields through the **field strength tensor**, given by

$$\mathscr{L}_{QCD} \supset -\frac{1}{4}F^a_{\mu\nu}F^{a\mu\nu} \tag{1.6}$$

where

$$F^a_{\mu\nu} = \partial_\mu A^a_\nu - \partial_\nu A^a_\mu + gf^{abc}A^b_\mu A^c_\nu \tag{1.7}$$

In the case of QED with symmetry group U(1), the theory is abelian (which also means that the structure constants vanish) and there is only one generator, namely the identity matrix. The expression above then becomes the 'free electromagnetic field Lagrangian', yielding Maxwell's equations.

1.1.2 Gauge-fixing and ghosts

The QCD Lagrangian density is thus far composed of the following terms

$$\mathscr{L}_{QCD} \supset \bar{\psi}(i\not{D} - m)\psi - \frac{1}{4}F^a_{\mu\nu}F^{a\mu\nu} \tag{1.8}$$

However, this is not the full picture. By quantizing the theory, problems associated with gauge redundancy appear. They originate from the operator $P^\perp_{\mu\nu} = g_{\mu\nu} - k_\mu k_\nu/k^2$ in the field strength tensor which is in fact the transverse projection operator and has a zero mode, i.e. a vanishing eigenvalue. The longitudinal eigenvectors all map to the eigenvalue zero, which makes for a divergent sum over infinitely many eigenvectors with amplitude 1 (because the action is 0). The trick will be to fix the gauge (thus breaking gauge symmetry) so that these redundant eigenvectors are no longer gauge-equivalent.

Leaving the details aside, the fix requires adding a gauge-fixing term where a choice for the parameter ξ needs to be made:

$$\mathscr{L}_{\text{gauge}-\text{fixing}} = -\frac{1}{2\xi}(\partial_\mu A^{\mu a})^2 \tag{1.9}$$

The Landau gauge ($\xi = 0$) subtracts all unphysical (longitudinal) polarizations, whereas the Feynman gauge ($\xi = 1$) contains all four polarizations.

The fix for QCD needs one more ingredient, namely adding new fields, called ghost fields. These are a consequence of the non-abelian nature of QCD and the fact that unphysical (longitudinal) modes re-interact with gauge fields in the non-abelian gauge transformations. The ghosts are scalar, massless fields and interact only with other ghost fields and gluon fields:

$$\mathscr{L}_{\text{ghost}} = -\bar{c}^a \partial_\mu D^\mu_{ab} c^b \tag{1.10}$$

1.1.3 Feynman rules of QCD

To sum things up, all the Feynman rules of QCD have been laid out in this section.

Quark propagator 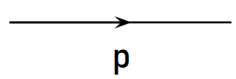

$\rightarrow \quad \frac{i}{\not{p}-m+i\epsilon}$

Gluon propagator 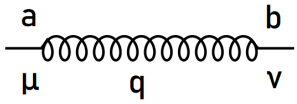

$\rightarrow \quad \frac{i\delta^{ab}}{q^2+i\epsilon}\left[g^{\mu\nu}-(1-\xi)\frac{\kappa^\mu\kappa^\nu}{\kappa^2}\right]$

Ghost propagator 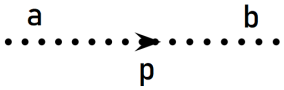

$\rightarrow \quad \frac{i\delta_{ab}}{p^2+i\epsilon}$

Quark-gluon vertex 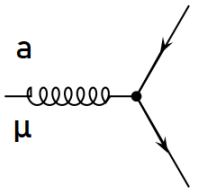

$\rightarrow \quad -ig_s\gamma^\mu T^a_{ij}$

Ghost-gluon vertex 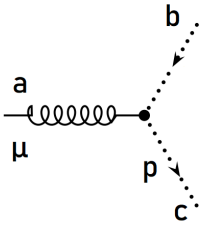

$\rightarrow \quad g_s f^{abc} p^\mu$

3-gluon vertex 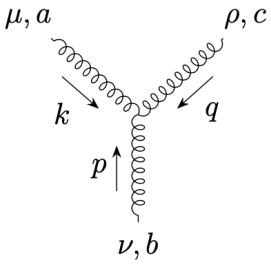

$\rightarrow \quad -g_s f^{abc}\left[g^{\mu\nu}(k-p)^\rho + g^{\nu\rho}(p-q)^\rho + g^{\rho\mu}(q-k)^\rho\right]$

4-gluon vertex 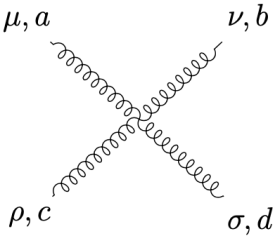

$\rightarrow \quad -ig_s^2\begin{bmatrix} f^{abe}f^{cde}(g^{\mu\rho}g^{\nu\sigma}-g^{\mu\sigma}g^{\nu\rho}) \\ +f^{ace}f^{bde}(g^{\mu\nu}g^{\rho\sigma}-g^{\mu\sigma}g^{\rho\nu}) \\ +f^{ade}f^{bce}(g^{\mu\rho}g^{\sigma\nu}-g^{\mu\nu}g^{\rho\sigma}) \end{bmatrix}$

with roman letters (a, b, c, d, e) representing the colour.

1.2 Deep inelastic scattering (DIS) and structure functions

Deep inelastic lepton-hadron scattering (DIS) is a process in which the innards of hadrons are probed using electrons, muons and/or neutrinos, much like an electron microscope. Hadrons are composite particles made up of any number of quarks. In the quark model, baryons are made up of 3 quarks (or 3 antiquarks) and mesons are made up of a quark-antiquark pair. This picture of hadrons is only an approximation, but is still widely used because of its applications, much like Niels Bohr's atomic model is only an approximation, but is accurate enough to have plenty of useful applications. A more accurate description is that of 'sea quarks' and 'valence quarks'. Because of quantum fluctuations, quarks can emit a gluon at any given time which can either decay into a quark-antiquark pair or emit another gluon, which leads to a cascade of reactions. Notice that the number of quarks added or subtracted by a gluon is always a quark-antiquark pair; these are called the sea quarks. On the other hand, there are quarks that do not originate from these quantum fluctuations which are called the valence quarks. Baryons have three valence (anti)quarks and mesons have one quark and one antiquark.

DIS has historically provided one of the most powerful tests of QCD as the theory of the strong interaction. Besides, DIS nowadays provides us with the best available information on the momentum distributions of quarks and gluons in hadrons, which are needed as inputs in computing theoretical predictions for cross sections in high-energy hadron-hadron collisions such as those at the Large Hadron Collider (LHC).

In this section we describe the basic features of DIS and introduce the DIS structure functions. DIS structure functions are the main physical observables investigated in this thesis: they will be at the center of the studies reported in chapter 3.

1.2.1 DIS kinematics

Consider an electron of momentum k scattering to one of momentum k' by exchanging a photon of momentum q with a proton of momentum p, as illustrated in Figure 1.2. The center-of-mass energy squared is $s = (k + p)^2$. Let Q^2 be the photon virtuality

$$Q^2 = -q^\mu q_\mu \quad , \tag{1.11}$$

and let x be the ratio

$$x = \frac{Q^2}{2p \cdot q} \quad . \tag{1.12}$$

In terms of Q^2 and x one can calculate two other variables which are commonly used to describe DIS kinematics,

$$W^2 \;=\; (p+q)^2 \;=\; Q^2 \frac{1-x}{x}, \tag{1.13}$$

$$y \;=\; \frac{p\cdot q}{p\cdot k} \;=\; \frac{Q^2}{xs}. \tag{1.14}$$

The kinematic limits are $Q^2 < s$, $x > Q^2/s$.

For low Q^2 ($Q^2 \ll R_p^{-2}$, where R_p is the proton radius) one only observes elastic proton scattering; but as Q^2 increases the photon can be absorbed by thecharged quark constituents of the proton. We will examine the deep-inelastic region, $\min\{Q^2, W^2\} \gg R_p^{-2}$.

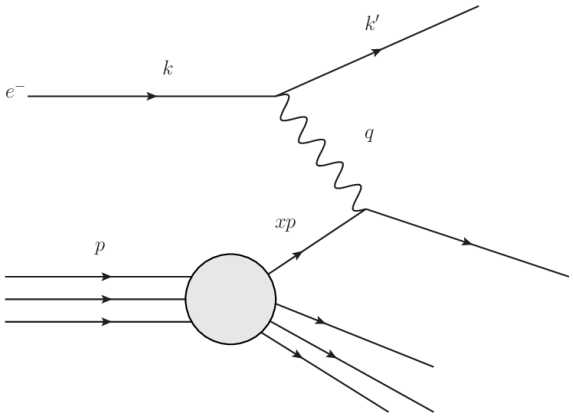

Figure 1.2: An electron with momentum k scatters on a proton with momentum p by exchanging a photon with momentum q. The actual collision happens with only a part of the proton-momentum xp, whose fraction is denoted by $x \in]0,1[$.

We will see next that the general structure of the DIS cross section as a function of s, for given Q^2 and x, may be parameterized, based on Lorentz and gauge invariance principles, in terms of so-called DIS structure functions.

1.2.2 DIS structure functions

Let us denote by $e\,T_\mu(p,q;\{p_X\})$ the scattering matrix element for a proton of momentum p to absorb a photon of momentum q and Lorentz index μ to produce a set of hadrons X with fixed momenta $\{p_X\}$. The scattering matrix element squared for the whole process is given by

$$|\mathcal{M}|^2 = \frac{e^4}{Q^4}\, L^{\mu\nu}\, T_\mu(p,q;\{p_X\})\, T^*_\nu(p,q;\{p_X\}), \tag{1.15}$$

where the leptonic tensor

$$L^{\mu\nu} = \mathrm{Tr}\left\{\not{k}\gamma^\mu \not{k}'\gamma^\nu\right\} \tag{1.16}$$

describes the electron-photon subprocess.

If the state X consists of n hadrons, then the n+1-body phase space for the whole process can be written as a part describing the electron kinematics times the n-body phase space for X,

$$dPS = \frac{Q^2}{16\pi^2 s x^2}\, dQ^2\, dx\, dPS_X. \tag{1.17}$$

We write the DIS cross section as

$$d\sigma = |\mathcal{M}|^2 dPS. \tag{1.18}$$

By integrating over the phase space of X and summing over all possible states X, we define the hadronic tensor

$$\sum_X \int dPS_X\, T_\mu(p,q;\{p_X\})\, T^*_\nu(p,q;\{p_X\}) = H_{\mu\nu}, \tag{1.19}$$

where $H_{\mu\nu}$ can only depend on the vectors p and q and, since the electromagnetic and strong interactions conserve parity, must be symmetric in μ and ν.

We now parameterize the hadronic tensor $H_{\mu\nu}$ by considering all possible symmetric two-index tensors that can be constructed from two vectors, and perform its contraction with $L_{\mu\nu}$ according to Eq. (1.15). We find that nonzero contributions come from the following terms,

$$H_{\mu\nu} = -H_1 g_{\mu\nu} + H_2 \frac{p_\mu p_\nu}{Q^2}, \tag{1.20}$$

where H_1 and H_2 are scalar functions of the only two Lorentz scalars available $q\cdot q = -Q^2$ and $p\cdot q = Q^2/2x$, i.e., of x and Q^2. More precisely, we get

$$L^{\mu\nu} H_{\mu\nu} = 4k\cdot k'\, H_1 + 4\frac{p\cdot k\; p\cdot k'}{Q^2}\, H_2. \tag{1.21}$$

By redefining $H_1 = 4\pi F_1$ and $H_2 = 8\pi x F_2$, we obtain the result for the scattering cross section

$$\frac{d^2\sigma}{dx\, dQ^2} = \frac{4\pi\alpha^2}{xQ^4}\left[y^2 x F_1(x,Q^2) + (1-y)F_2(x,Q^2)\right]. \tag{1.22}$$

We note that, for fixed x and Q^2, the s dependence of the scattering cross section enters through the y dependence, since $y = Q^2/(xs)$.

The functions F are called the structure functions of the proton. Other commonly-used linear combinations of the structure functions are

$$F_T(x,Q^2) = 2xF_1(x,Q^2), \tag{1.23}$$

$$F_L(x,Q^2) = F_2(x,Q^2) - 2xF_1(x,Q^2), \tag{1.24}$$

which correspond to scattering of transverse and longitudinally polarized photons respectively. The cross section can then be written as

$$\frac{d^2\sigma}{dx\, dQ^2} = \frac{2\pi\alpha^2}{xQ^4}\left[(1+(1-y)^2)F_T(x,Q^2) + 2(1-y)F_L(x,Q^2)\right]. \tag{1.25}$$

The most common parameterization of the cross section is in terms of F_2 and F_L,

$$\frac{d^2\sigma}{dx\, dQ^2} = \frac{2\pi\alpha^2}{xQ^4}\left[(1+(1-y)^2)F_2(x,Q^2) - y^2 F_L(x,Q^2)\right]. \tag{1.26}$$

For the majority of current measurements, y^2 is small and F_L can be neglected. However, it needs to be included in the region close to the kinematic limit $y = 1$, or for very precise data.

So far we have said nothing about how the structure functions F in Eq. (1.26) behave as functions of x and Q^2. In the next two subsections, we discuss the structure functions according to the parton model, originally proposed by Bjorken and Feynman, and in QCD. First, we discuss that, if the photon interacts with pointlike constituents of the proton (partons) and no dimensionful scale is involved in this interaction, then the dimensionless structure functions F in Eq. (1.26) cannot depend on Q^2, and are only functions of x. This behavior is known as Bjorken scaling, and the corresponding physical picture is the parton model. This behavior is, approximately, rather well satisfied by observations.

Next, we discuss that in QCD the basic picture of the photon interacting with pointlike partons, as constituents of the proton, is retained, but the interactions are characterized by a dimensionful scale, which leads to small, logarithmic corrections to Bjorken scaling, so that

the structure functions F in Eq. (1.26) become slowly (logarithmically) dependent on Q^2. This behavior is known as scaling violation, and constitutes the distinctive feature of the field-theoretic treatment of the scattering in QCD, beyond the original parton model. The scaling violation effects are numerically small; accurate DIS measurements are able to detect them, and the scaling-violation predictions are nowadays verified to very high precision.

1.2.3 Parton model: Bjorken scaling and parton distribution functions

The parton model can be conveniently introduced by considering DIS in a reference frame in which the incoming proton has very large momentum in the z direction ("infinite-momentum" frame). What happens can then be pictured as follows.

The proton is Lorentz-contracted in the longitudinal direction. The time it takes the electron to cross the proton, $\Delta t_{\rm scatter}$, shortens as the proton momentum becomes large. On the other hand, the proton's internal interactions are time-dilated. The typical timescale for interactions among quark constituents — call them "partons" — inside the proton, $\tau_{\rm parton}$, becomes larger and larger as the proton momentum increases. For

$$\Delta t_{\rm scatter} \ll \tau_{\rm parton} \tag{1.27}$$

the electron sees a hadronic state with definite number of partons, each of which is in a state of definite momentum, characterized by a fraction ξ of the proton's momentum p. We may denote by $f_{\rm q/p}(\xi)$ the distribution function of parton q in the proton, as a function of momentum fraction ξ.

For large Q^2 the distance traveled by the virtual photon is small,

$$\Delta l_\gamma \sim 1/\sqrt{Q^2} \ll R_p^{-1} \quad . \tag{1.28}$$

So if the density of partons is low enough the photon interacts with only one parton. The probability of its interacting with n partons is suppressed by a factor $(R_p^2 Q^2)^{-n}$, and we regard the process as dominated by single parton scattering.

Now, as the photon-parton scattering does not interfere with the interactions among partons occurring at time-dilated scales, we may compute the process by combining probabilities rather than amplitudes. In this situation the DIS cross section $\sigma_{\rm e-p}$ can be obtained, up to corrections down by powers of Q^2, from the cross section $\sigma_{\rm e-q}$ for the scattering of the electron from parton q, carrying momentum fraction ξ of the proton momentum, times the distribution function $f_{\rm q/p}$ of parton q in the proton, integrated over ξ and summed over q:

$$\frac{d^2\sigma({\rm e-p})}{dx\,dQ^2} = \sum_q \int d\xi\, f_{\rm q/p}(\xi) \frac{d^2\sigma({\rm e-q})}{dx\,dQ^2}. \tag{1.29}$$

To compute $\sigma_{\rm e-q}$ we need the scattering matrix element for $eq \to eq$. Using the kinematic variable y defined in Eq. (1.14), we obtain

$$|\mathcal{M}|^2 = 8(4\pi\alpha)^2\, e_q^2 N_c\, \frac{1+(1-y)^2}{y^2}, \tag{1.30}$$

where e_q is the parton's electric charge in units of e and N_c is the number of colors. As in Eq. (1.17), the phase space is given by

$$dPS = \frac{Q^2}{16\pi^2 s x^2} dQ^2\, dx\, dPS_X. \tag{1.31}$$

Since X consists only of one massless parton, we have

$$dPS_X = \frac{d^4p_X}{(2\pi)^3}\delta(p_X^2)\,(2\pi)^4\delta^4(\xi p + q - p_X) \tag{1.32}$$

$$= \frac{2\pi x}{Q^2}\delta(\xi - x). \tag{1.33}$$

The cross section is thus

$$\frac{d\sigma}{dx\,dQ^2} = \frac{1}{4N_c}\,\frac{1}{2\hat{s}}\,\frac{Q^2}{16\pi^2 s x^2}\,\frac{2\pi x}{Q^2}\,\delta(x-\xi)\,|\mathcal{M}|^2 \tag{1.34}$$

$$= \frac{1}{4N_c}\,\frac{y^2}{16\pi Q^4}\,\delta(x-\xi)\,|\mathcal{M}|^2, \tag{1.35}$$

where the factor of $1/N_c$ is the average over incoming colors. So we have

$$\frac{d\sigma(\mathrm{e}-\mathrm{q})}{dx\,dQ^2} = \frac{2\pi\alpha^2}{Q^4}\,\delta(x-\xi)\;e_q^2\,\Big(1+(1-y)^2\Big) \tag{1.36}$$

and hence

$$\frac{d\sigma(\mathrm{e}-\mathrm{p})}{dx\,dQ^2} = \frac{2\pi\alpha^2}{xQ^4}\,\Big(1+(1-y)^2\Big)\sum_q e_q^2\,x f_{\mathrm{q/p}}(x). \tag{1.37}$$

Comparing (1.37) with (1.26) we therefore get

$$F_2(x,Q^2) = \sum_q e_q^2\,x f_{\mathrm{q/p}}(x), \tag{1.38}$$

$$F_L(x,Q^2) = 0. \tag{1.39}$$

We thus see that in the parton model F_2 is Q^2-independent, showing Bjorken scaling, and is given by the charge-weighted sum of the parton distribution functions $f_{\mathrm{q/p}}$ (PDFs), while F_L vanishes.

1.2.4 QCD corrections to the parton model

In the parton model, DIS is schematized through the photon undergoing a single parton scattering, and partons do not have any further interactions. Partons, however, do interact via QCD. When we include QCD corrections, the Bjorken scaling is modified by small logarithmic violations of scaling, and the structure functions become Q^2-dependent.

The evaluation of QCD corrections to the parton model implies taking into account, besides the $eq \to eq$ scattering matrix element in Eq. (1.30), the contributions with real and virtual gluon emission from it, as well as new contributions with eg scattering. Fig. 1.3 shows an electron scattering on a proton with some examples of gluon interactions taken into account.

It can be shown that these contributions give rise to divergences corresponding to parton interactions occurring at long time scales before the hard interaction with the photon, and that a consistent way to take these into account is to associate all long-time, or low-momentum, interactions to the distribution function $f_{\mathrm{q/p}}$ introduced in the parton model in Eq. (1.29), and all short-time, or high-momentum, interactions to the $\sigma(\mathrm{e}-\mathrm{q})$ cross section in Eq. (1.29).

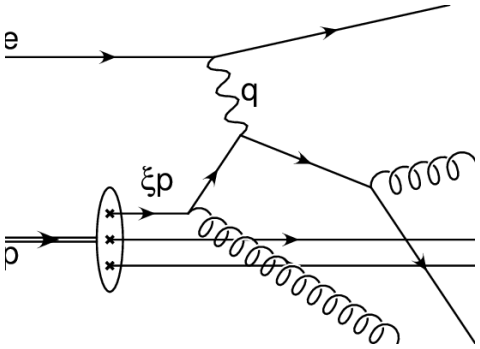

Figure 1.3: An electron scatters on a proton, just like in Fig. 1.2, but gluons are also produced, be it in an intermediate or final and real or virtual state. This adds a new range of feynman diagrams to take into account compared to the previous picture of DIS.

If we denote by μ the (arbitrary) momentum scale by which we separate low-momentum and high-momentum interactions, this means that in QCD both the $f_{\mathrm{q/p}}$ and $\sigma(\mathrm{e}-\mathrm{q})$ factors become dependent on μ, and the parton model formula (1.29) for the DIS cross section is modified to the QCD factorization formula

$$\frac{d^2\sigma(\mathrm{e}-\mathrm{p})}{dx\,dQ^2} = \sum_q \int_x^1 d\xi\, f_{\mathrm{q/p}}(\xi,\mu)\frac{d^2\sigma(\mathrm{e}-\mathrm{q})}{dx\,dQ^2}(x/\xi,Q,\mu). \tag{1.40}$$

The scale μ is termed factorization scale, and it is important that, although μ appears in the right hand side of Eq. (1.40), the left hand side is independent of μ. We come back to this shortly.

The parton distributions f_j have here been introduced heuristically from parton model ideas, but they can also be given a formal definition in terms of correlation functions of bilinear field operators. These, in turn, can be expanded in a series of local operators, with well-prescribed coefficient functions. In this case, the dependence of f_j on the scale μ can be understood as arising from the renormalization of the ultraviolet divergences of the non-local operators.

Corresponding to the above formula (1.40) for the cross section $\sigma(\mathrm{e}-\mathrm{p})$, the structure functions F_i are given, up to corrections down by powers of Q^2, by factorization formulas

$$F_k(x,Q) = \sum_j \int_x^1 d\xi\; C_{kj}(x/\xi,\alpha_s,Q/\mu)\; f_j(\xi,\mu) \tag{1.41}$$

where f are parton distributions and C are hard-scattering functions, computable in perturbation theory as power series expansions in α_s,

$$C_{kj}(x,\alpha_s,Q/\mu) = \sum_n\; C_{kj}^{(n)}(x,Q/\mu)\;\alpha_s^n\;\;. \tag{1.42}$$

The ξ dependence of Eq. (1.41) can be diagonalized by taking, for any function of ξ, N-moments defined as the Mellin transform

$$f_N(\mu) = \int_0^1 d\xi\,\xi^{N-1} f(\xi,\mu)\;\;, \tag{1.43}$$

so that

$$F_{k,N}(Q) = \sum_j \; C_{kj,N}(\alpha_s, Q/\mu) \; f_{j,N}(\mu) \tag{1.44}$$

The important point is that the physical structure functions F_k being independent of μ in Eq. (1.41) implies evolution equations for the PDFs f_j. Schematically, the structure of the equations is as follows. Since the left hand side of Eq. (1.41) does not depend on μ, we have

$$\frac{d}{d\ln\mu} F_N(Q^2) = 0 \;\; . \tag{1.45}$$

Then f and C must obey the equations

$$\frac{d}{d\ln\mu} \ln f_N = \gamma_N = -\frac{d}{d\ln\mu} \ln C_N \;\; , \tag{1.46}$$

with γ_N a function of α_s, computable as a perturbation expansion

$$\gamma_N(\alpha_s) = \sum_{n=1}^{\infty} \; b_N^{(n)} \; \alpha_s^n \;\; . \tag{1.47}$$

So although f_j, which depend on soft momentum scales, are not calculable perturbatively, their variation with the scale μ is. This result is of great importance, as it allows us to connect the outcomes of experiments at different scales of momentum transfer. From Eq. (1.46) we get

$$f_N(\mu) = f_N(\mu_0) \; \exp\left(\int_{\mu_0}^{\mu} \gamma_N(\alpha_s) \frac{d\mu'}{\mu'} \right) . \tag{1.48}$$

The exponential factor in Eq. (1.48) represents the violation of scaling, and the function γ_N controlling it via Eq. (1.48) is termed the anomalous dimension.

The complete theoretical framework to describe the QCD dynamics described here, including the μ dependence, the scaling violation and the anomalous dimension, is the Renormalization Group (RG). In the next chapter we will introduce the RG, and we will thus be able to revisit the results of this section from the RG viewpoint.

We have written Eqs. (1.46),(1.47) in moment space, suppressing parton indices. Transforming back to x space and restoring the parton indices, the evolution equations read

$$\boxed{\frac{d}{d\ln\mu^2} f_i(x,\mu) = \sum_j \int_x^1 \frac{d\xi}{\xi} \; P_{ij}(\alpha_s, x/\xi) \; f_j(\xi,\mu) \;\; ,} \tag{1.49}$$

where $P_{ij}(\alpha_s, z)$ are the so-called splitting functions, related to the anomalous dimensions $\gamma_{ij,N}(\alpha_s)$ by the Mellin transform

$$\gamma_{ij,N}(\alpha_s) \equiv \int_0^1 dz \; z^{N-1} \; P_{ij}(\alpha_s, z) \;\; . \tag{1.50}$$

Eqs. (1.49) are the Dokshitzer-Gribov-Lipatov-Altarelli-Parisi (DGLAP) evolution equations [14, 15, 16].

It is often useful to also introduce the momentum weighted parton distributions $\tilde{f}_i$

$$\tilde{f}_i(x,\mu^2) = x f_i(x,\mu^2) \;\; . \tag{1.51}$$

These obey the evolution equations

$$\frac{d\,\tilde{f}_i(x,\mu^2)}{d\ln\mu^2} = \sum_j \int_x^1 dz\; P_{ij}(\alpha_s,z)\;\tilde{f}_j(x/z,\mu^2)\;\;. \tag{1.52}$$

The splitting functions P_{ij} are computable in QCD perturbation theory as a power series expansion in α_s:

$$P_{ij}(\alpha_s,z) = \sum_{n=1}^{\infty}\left(\frac{\alpha_s}{2\pi}\right)^n P_{ij}^{(n-1)}(z)\;. \tag{1.53}$$

They have the following explicit expressions at leading order:

$$\begin{aligned}
P_{gg}^{(0)}(z) &= 2\,C_A\left[\left(\frac{1}{1-z}\right)_+ - 1 + \frac{1-z}{z} + z(1-z)\right] + \left(\frac{11}{6}\,C_A - \frac{2}{3}\,T_R\,N_f\right)\delta(1-z)\;\;,\\
P_{gq_i}^{(0)}(z) &= P_{g\bar{q}_i}^{(0)}(z) = C_F\,\frac{1+(1-z)^2}{z}\;\;,\\
P_{q_ig}^{(0)}(z) &= P_{\bar{q}_ig}^{(0)}(z) = T_R\left[z^2+(1-z)^2\right]\;\;,\\
P_{q_iq_j}^{(0)}(z) &= P_{\bar{q}_i\bar{q}_j}^{(0)}(z) = C_F\left(\frac{1+z^2}{1-z}\right)_+\delta_{ij}\;\;,\quad P_{q_i\bar{q}_j}^{(0)}(z) = P_{\bar{q}_iq_j}^{(0)}(z) = 0\;\;,
\end{aligned} \tag{1.54}$$

in terms of the $SU(N_c)$ color factors

$$C_A = N_c\;\;,\quad C_F = \frac{N_c^2-1}{2\,N_c}\;\;,\quad \mathrm{Tr}\,(t^at^b) = \delta_{ab}\,T_R = \frac{1}{2}\,\delta_{ab}\;\;. \tag{1.55}$$

Eqs. (1.41),(1.49) constitute the basic equations of the "QCD parton model", i.e., the QCD generalization of the parton model formulas (1.38),(1.39). In the next chapter we will discuss the renormalization group (RG), and we will study Eqs. (1.41),(1.49) from the RG point of view.

1.3 Summary of Chapter 1 and outlook

In this chapter we have introduced QCD (Quantum Chromodynamics) as the gauge theory of the strong interaction (Sec 1.1), and we have described DIS (Deep Inelastic Scattering) in lepton-hadron collisions as one of the classic probes of QCD (Sec 1.2).

We have introduced the DIS structure functions F_j which parameterize the scattering cross section in Eqs. (1.22)-(1.26). These structure functions will be the object of the detailed numerical studies performed in this thesis, which will be described in Chapter 3.

We have also introduced the QCD factorization formulas for DIS structure functions in Eq. (1.41), in terms of hard-scattering functions and parton distribution functions (PDFs), and the corresponding evolution equations in Eq. (1.49), the so-called DGLAP equations. These factorization formulas and evolution equations will be the object of investigations from the viewpoint of the theory of the Renormalization Group (RG) in Chapter 2. All the results presented in this thesis will be rooted in these factorization formulas and evolution equations.

We will next proceed as follows. In Chapter 2 we will discuss the concepts of renormalization and renormalization group, and we will apply this to examine perturbative solutions of the

RG evolution equations (RGEs). We here will describe a formalism to evaluate theoretical systematic uncertainties on PDFs due to perturbative RGE solutions. This formalism will constitute the basis for numerical studies of DIS structure functions, which will be carried out in Chapter 3. In Chapter 3 we will employ dedicated software to compute the F_2 and F_L structure functions of Eq. (1.26) at next-to-leading order (NLO), next-to-next-to-leading order (NNLO) and next-to-next-to-next-to-leading order ($\mathrm{N^3LO}$) in QCD perturbation theory, and to obtain the corresponding RGE systematic uncertainties.

Chapter 2

Renormalization Group (RG) and Perturbative Solutions

In this chapter, the concept of renormalization and the renormalization group equations will be introduced. This approach was an important breakthrough for multiple fields of modern physics: among them, particle physics. The theory provides us with a way to deal with quantum fluctuations at the shortest distances when calculating Feynman diagrams.

2.1 Loops and divergences

Feynman diagrams give a picture of what happens when particles interact with each other. A particle propagating through space-time can and will emit or absorb particles of any energy. These emitted and absorbed particles are called **'virtual particles'** and can in turn also produce other (virtual) particles. Their energy can take on any value for a short amount of time according to the Heisenberg uncertainty principle. This makes **loop diagrams** possible where a particle or a pair of particles is emitted and immediately re-absorbed. A simple propagating particle is then not so simple anymore because of these higher-order diagrams.

To calculate a physical cross section, one must sum over every single Feynman diagram that's allowed by the theory. Loop diagrams, in particular, are characterized by arbitrarily large momenta that may flow in the loop. To deal with the regions of large momenta (ultraviolet regions), the method of **'renormalization'** is introduced. In the following section, we'll take a look at the example of the photon self-energy.

2.1.1 Photon self-energy

In a general non-abelian gauge theory, for one ingoing boson and one outgoing boson the Feynman diagram at lowest order is given by

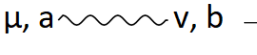

$$\rightarrow \quad \frac{-ig_{\mu\nu}\delta^{ab}}{k^2} \tag{2.1}$$

where a and b are the gauge-group indices of the boson.

At first order, the Feynman diagram is given by

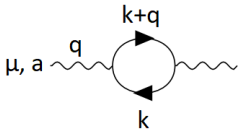

$$\rightarrow \quad \frac{-ig^{\mu\rho}\delta^{ab}}{q^2} i\pi^{ab}_{\rho\sigma} \frac{-ig^{\sigma\nu}\delta^{ab}}{q^2} \tag{2.2}$$

where the fermion loop contribution can be written as

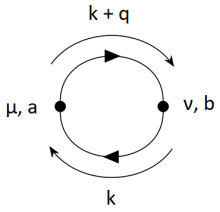

$$\rightarrow \quad (-ig)^2(-1)Tr(T^aT^b)\int \frac{d^4k}{(2\pi)^4} Tr\left[\gamma_\mu \frac{i}{\not{k}-m}\gamma_\nu \frac{i}{\not{k}+\not{q}-m}\right] \tag{2.3}$$

$$\equiv i\pi^{ab}_{\mu\nu}$$

We will focus on the abelian case of the *photon*. In this case, δ^{ab} is left out, and the trace $Tr(T^aT^b)$ is replaced by 1. (For QCD, this trace equals $\frac{1}{2}\delta^{ab}$.) Summing diagrams with multiple insertions of the one-loop contributions gives the following series

Figure 2.1: The photon self-energy on the left-hand side (LHS) as an infinite sum of one-loop feynman diagrams.

The amplitude on the LHS is a **primitively divergent amplitude**. For QED, there are 3 primitively divergent amplitudes: the photon self-energy, the electron self-energy and the electron-photon vertex. For QCD, there are 7 of them: the gluon self-energy, the quark self-energy, the ghost self-energy, the gluon 3- and 4-point vertex, the quark-gluon vertex and the ghost-gluon vertex.

The photon self-energy only has fermion loops as one-loop corrections to the amplitude (see figure in Eq. 2.2) (whereas the gluon self-energy has additional interactions other than with fermions, which makes for more Feynman diagrams to sum over at one loop, see Sec. 2.3).

Looking at the integral in the expression (2.3), one could count the powers of k in the numerator and in the denominator to find out the so-called **'superficial degree of divergence'** defined as

$$D := 4 + \text{powers of k in numerator} - \text{powers of k in denominator} \tag{2.4}$$

If $D \geq 0$, then the integral is **ultraviolet (UV) divergent**, because it blows up at infinite momenta/energies. In the case of equation (2.3), $\pi^{ab}_{\mu\nu}$ would give $D = 2$, but because of gauge invariance, for $\pi^{ab}_{\mu\nu}$ to only contain physical polarizations and no unphysical ones, it needs to be proportional to the transverse projector $g_{\mu\nu}q^2 - q_\mu q_\nu$, which gives

$$\pi^{ab}_{\mu\nu} = (g_{\mu\nu}q^2 - q_\mu q_\nu)\Pi^{ab}. \tag{2.5}$$

That is, the photon self-energy is purely transversal. Π^{ab} now needs 2 powers of k less which reduces the superficial degree of divergence by 2 and makes it 0, i.e., it reduces the divergence from quadratic to logarithmic. The method of **renormalization** will now be introduced to evaluate the fermion loop contribution.

2.1.2 Renormalization

For a theory to be renormalizable, it must have a finite amount of primitively divergent amplitudes, which is the case for QED and QCD. The procedure for renormalization can be summed up in the following steps:

1. The first step will be to choose a **regularization method**. This is a method to get rid of the infinity by paying the price of adding a so-called **renormalization scale** μ.
   One method is to set a **cutoff** Λ for the upper bound of the integrand. The integral is then separated into a finite part from zero to Λ and an infinite part from Λ to infinity.

   $$\int_0^\infty \to \int_0^\Lambda + \int_\Lambda^\infty$$

   The motivation for this cutoff regularization comes from an effective field theory viewpoint of the Standard Model. This is the idea that our current model is only an accurate prediction in the low-energy region, and that at high-energies (presumably at a scale Λ), physics beyond the Standard Model (BSM physics) will have substantial effects anyways.
   Another method is **dimensional regularization**. This complicated term actually just means to reduce the dimension of d^4k by a very small amount of 2ϵ to make integral non-divergent. However, the final result of this integral is the matrix element and should retain the same dimension, so a dimensionful mass scale parameter μ, called the **'renormalization scale'** is added to compensate for it.

   $$\frac{d^4k}{(2\pi)^4} \to (\mu^2)^\epsilon \frac{d^{4-2\epsilon}k}{(2\pi)^{4-2\epsilon}}$$

2. The second step will be to rescale the wave functions and parameters of the theory. The scaling factor for each quantity is called the **'renormalization constant'**.

   $$\psi \to \psi_0 = Z\psi$$

On the LHS, ψ is the unrenormalized quantity and on the RHS, ψ_0 is the unrenormalized quantity and ψ the renormalized quantity with Z the renormalization constant. These rescalings will be the trick to getting rid of infinities before they have even emerged. It is meaningful to do this because the rescalings themselves are not observables.

2.1.3 Renormalizing the QED coupling constant

We now give a concrete example for the calculations. With the γ matrix trace properties,

$$\begin{aligned} Tr\left[\gamma_\mu\gamma_\nu\right] &= 4g_{\mu\nu} \\ Tr\left[\gamma_{\alpha_1}\gamma_{\alpha_2}...\gamma_{odd}\right] &= 0 \\ Tr\left[\gamma_\mu\gamma_\nu\gamma_\rho\gamma_\sigma\right] &= 4(g_{\mu\nu}g_{\rho\sigma} - g_{\mu\rho}g_{\nu\sigma} + g_{\mu\sigma}g_{\nu\rho}) \end{aligned} \tag{2.6}$$

and the integration trick using Feynman parametrization,

$$\frac{1}{AB} = \int_0^1 \frac{dx}{[xA + (1-x)B]^2} \tag{2.7}$$

we can now apply dimensional regularization on the one-loop diagram from equation (2.3):

$$(-ig)^2(-1)Tr(T^aT^b)(\mu^2)^\epsilon \int \frac{d^{4-2\epsilon}k}{(2\pi)^{4-2\epsilon}} Tr\left[\gamma_\mu \frac{i}{\not{k} - m}\gamma_\nu \frac{i}{\not{k} + \not{q} - m}\right] \tag{2.8}$$

The trace part inside the integral gives

$$\begin{aligned} &\Rightarrow\ Tr\left[i\gamma_\mu \frac{\not{k} + m}{k^2 - m^2} i\gamma_\nu \frac{\not{k} + \not{q} + m}{(k+q)^2 - m^2}\right] \\ &= \frac{1}{k^2 - m^2}\frac{1}{(k+q)^2 - m^2}(-1)Tr\left[\gamma_\mu(\not{k} + m)\gamma_\nu(\not{k} + \not{q} + m)\right] \\ &= -\int_0^1 \frac{dx}{[x(k^2 - m^2) + (1-x)((k+q)^2 - m^2)]^2} \times \\ &\quad 4\left[(g_{\mu\alpha}g_{\nu\beta} - g_{\mu\nu}g_{\alpha\beta} + g_{\mu\beta}g_{\alpha\nu})k^\alpha(k^\beta + q^\beta) + m^2 g_{\mu\nu}\right] \\ &= -\int_0^1 \frac{dx}{[(k + q(1+x))^2 + x(1-x)q^2 - m^2]^2} \times \\ &\quad 4\left[2k_\mu k_\nu + \cancel{k_\mu q_\nu} + \cancel{k_\nu q_\mu} - g_{\mu\nu}(k\cdot(k + \cancel{q}) - m^2)\right] \\ &= -4\int_0^1 \frac{dx}{[l^2 + x(1-x)q^2 - m^2]^2}\left[2l_\mu l_\nu + q_\mu q_\nu(x-1) - g_{\mu\nu}(l^2 + q^2(x-1) + m^2)\right] \end{aligned} \tag{2.9}$$

with $l = k + q(1+x)$ and $dl = dk$, and terms with odd powers in k cancelled because of symmetry when integrating with respect to dk. Next up, according to equation (2.5), a part of the total amplitude $\pi^{ab}_{\mu\nu}$ contains a term proportional to $g_{\mu\nu}q^2$ which we can directly extract from equation (2.9) to get Π^{ab}. This lets us ignore the other more difficult terms in the integral and focus on the simpler part,

$$\begin{aligned} g_{\mu\nu}q^2\Pi^{ab} =&(-ig)^2(-1)Tr(T^aT^b)(\mu^2)^\epsilon \int \frac{d^{4-2\epsilon}l}{(2\pi)^{4-2\epsilon}}\times \\ &(-4)\int_0^1 \frac{dx}{[l^2+x(1-x)q^2-m^2]^2}\left[g_{\mu\nu}q^2(x-1)\right] \\ =&g_{\mu\nu}q^2 4g_s^2 Tr(T^aT^b)(\mu^2)^\epsilon \int_0^1 dx(x-1)\int \frac{d^{4-2\epsilon}l}{(2\pi)^{4-2\epsilon}}\frac{1}{[l^2+x(1-x)q^2-m^2]^2} \end{aligned} \tag{2.10}$$

To make sense of integration at non-integer dimensions, we look at the transformation $\int d^3p = \int_0^\infty dp 4\pi p^2$ in $n=3$ dimensions and extend the surface of the 2-sphere to a (n-1)-sphere for which the formula of the hypervolume is given as follows:

$$A_{n-1}(R) = \frac{2\pi^{n/2}}{\Gamma(n/2)}R^{n-1}$$

The transformation is then given by

$$\int d^Dl = \int dl \frac{2\pi^{D/2}}{\Gamma(D/2)}l^{D-1}$$

So equation (2.10) becomes,

$$\Pi^{ab} = 4g^2Tr(T^aT^b)(\mu^2)^\epsilon \int_0^1 dx(x-1)\frac{2\pi^{2-\epsilon}}{\Gamma(2-\epsilon)}\int_0^\infty \frac{dl}{(2\pi)^{4-2\epsilon}}\frac{l^{3-2\epsilon}}{[l^2+x(1-x)q^2-m^2]^2} \tag{2.11}$$

Continuing the calculation, the final result becomes

$$\Pi^{ab}(q^2) = -Tr(T^aT^b)\frac{g^2}{4\pi^2}\Gamma(\epsilon)\int_0^1 dx\left(\frac{4\pi\mu^2}{m^2-x(1-x)q^2}\right)^\epsilon 2x(1-x) \tag{2.12}$$

The Euler Γ function contains the logarithmic UV divergence, which appears as a pole at $\epsilon = 0$ in dimensional regularization. The UV divergent part of the self-energy can be extracted by computing the integral at $q^2 = 0$,

$$\Pi^{ab}(0) \approx -Tr(T^aT^b)\frac{g^2}{4\pi^2}\frac{1}{\epsilon}\frac{1}{3} \tag{2.13}$$

Specializing to the QED case, we have

$$\Pi(0) \simeq -\frac{\alpha}{3\pi}\ \frac{1}{\varepsilon} + \ldots \tag{2.14}$$

We can now use this result to evaluate the renormalized QED coupling, α. Suppose we consider a physical process occurring via photon exchange at momentum scale q^2, and we ask what the effect is from the multiple one-loop contributions in Figure 2.1 compared to the lowest order contribution in Eq. (2.1). By summing the series in Figure 2.1 through a geometric series, we obtain that the effect of renormalization amounts to

$$\begin{aligned} \frac{\alpha_0}{q^2} \quad &\longrightarrow \quad \frac{\alpha_0}{q^2}\frac{1}{1-\Pi(q^2)} \\ &\simeq \quad \frac{1}{q^2}\underbrace{\frac{\alpha_0}{1-\Pi(0)}}_{\alpha\equiv Z_3\alpha_0}\ \underbrace{\frac{1}{1-[\Pi(q^2)-\Pi(0)]}}_{q^2-\text{dependence}} \ . \end{aligned} \tag{2.15}$$

We see that the first effect of renormalization in Eq. (2.15) is that the strength of the coupling is modified to

$$\frac{\alpha_0}{1-\Pi(0)} \equiv \alpha \ , \tag{2.16}$$

from which we identify the rescaling, or renormalization constant Z_3,

$$\begin{aligned} Z_3 &\simeq 1+\Pi(0) \\ &= 1-\frac{\alpha}{3\pi}\,\frac{1}{\varepsilon}+\dots \quad , \end{aligned} \tag{2.17}$$

where in the last line we have used the explicit result for $\Pi(0)$ in Eq. (2.14). The coupling α in Eq. (2.16) is the physical coupling, that is, the renormalized coupling. This is obtained from the unrenormalized one, α_0, via a divergent, but unobservable, rescaling, according to the general procedure through the Z rescaling outlined in Sec. 2.1.2.

The second effect in Eq. (2.15) is that the coupling acquires a dependence on the momentum transfer q^2, controlled by the finite part of the self-energy, $\Pi(q^2)-\Pi(0)$. This dependence is free of divergences and observable. The q^2-dependence of the electromagnetic coupling is a new physical effect due to loop corrections. Using the explicit expression for Π given above, we obtain that for low q^2

$$\Pi(q^2)-\Pi(0) \to 0 \qquad \text{for} \quad q^2 \to 0 \ , \tag{2.18}$$

and for high q^2

$$\Pi(q^2)-\Pi(0) \simeq \frac{\alpha}{3\pi}\ln\frac{q^2}{m^2} \qquad \text{for} \quad q^2 \gg m^2 \ . \tag{2.19}$$

Thus α in Eq. (2.16) is the value of the coupling at $q^2=0$; the coupling increases as q^2 increases. Substituting Eqs. (2.16),(2.19) into Eq. (2.15) and rewriting it in terms of the fine structure, we have for large momenta

$$\alpha(q^2) = \frac{\alpha}{1-(\alpha/(3\pi))\ln(q^2/m^2)} \ . \tag{2.20}$$

The q^2-dependence of the coupling is referred to as running coupling. This phenomenon is shown in Figure 2.2, where α has been measured at different energies.

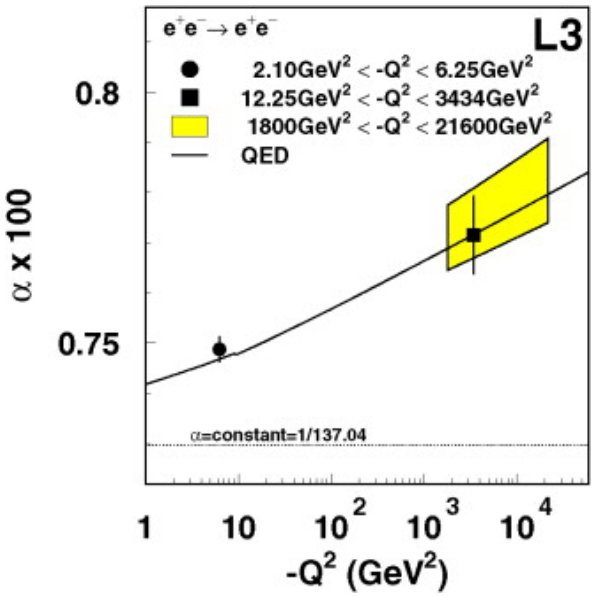

Figure 2.2: The QED running coupling obtained at LEP [17].

The result for the electromagnetic coupling that we have just found can be viewed as summing a series of perturbative large logarithms for $q^2 \gg m^2$. By expanding Eq. (2.20) in powers of α, we have

$$\begin{aligned} \alpha(q^2) &= \frac{\alpha}{1-(\alpha/(3\pi))\ln(q^2/m^2)} \\ &= \alpha\left(1+\frac{\alpha}{3\pi}\ln\frac{q^2}{m^2}+\cdots+\frac{\alpha^n}{(3\pi)^n}\ln^n\frac{q^2}{m^2}+\ldots\right) \quad . \end{aligned} \tag{2.21}$$

This is the simplest example of a conceptual framework referred to as resummation in QED and QCD. The point is that if the result (2.15) for the physical process is expressed in terms of an expansion in powers of α, as in Eq. (2.21), perturbative coefficients to higher orders are affected by large logarithmic corrections. On the other hand, one obtains a well-behaved perturbation series, without large higher-order coefficients, if the result is expressed in terms of the effective charge $\alpha(q^2)$.

2.2 Renormalization scale dependence and RG evolution equations (RGE)

In this section, the concept of renormalization group (RG) equations will be introduced. Let's take an observable quantity and rescale it according to the renormalization rules, for example:

$$\phi_0(p_i,\alpha_0) = Z\phi(p_i,\alpha,\mu) \tag{2.22}$$

where $\phi_0(p_i,\alpha_0)$ is the unrenormalized quantity, which is divergent, Z is the renormalization constant, and $\phi(p_i,\alpha,\mu)$ is the renormalized quantity after rescaling. Notice that because of

the method of regularization, a renormalization scale μ is added to ϕ after rescaling. However, ϕ_0 does not depend on μ, so the derivative of ϕ_0 with respect to μ gives zero.

$$\frac{d\phi_0}{d\mu} = 0$$

For the sake of convenience, $\ln(\mu^2)$ will be used instead of μ. Using the chain rule, this then becomes

$$\begin{aligned}
\frac{d\phi_0}{d(\ln\mu^2)} &= \frac{dZ}{d(\ln\mu^2)}\phi + Z\frac{d\phi}{d(\ln\mu^2)} \\
&= \frac{\partial Z}{\partial(\ln Z)}\frac{d\ln Z}{d(\ln\mu^2)}\phi + Z\left(\frac{\partial\phi}{\partial(\ln\mu^2)}\frac{d\ln\mu^2}{d(\ln\mu^2)} + \frac{\partial\phi}{\partial\alpha}\frac{d\alpha}{d(\ln\mu^2)}\right) \\
&= Z\left(\frac{d\ln Z}{d(\ln\mu^2)}\phi + \frac{\partial\phi}{\partial(\ln\mu^2)} + \frac{\partial\phi}{\partial\alpha}\frac{d\alpha}{d(\ln\mu^2)}\right) = 0 \\
\Leftrightarrow \quad &\left(\frac{d\ln Z}{d(\ln\mu^2)} + \frac{\partial}{\partial(\ln\mu^2)} + \frac{d\alpha}{d(\ln\mu^2)}\frac{\partial}{\partial\alpha}\right)\phi = 0
\end{aligned} \tag{2.23}$$

By defining the α and Z derivatives by

$$\beta(\alpha) := \frac{d\alpha}{d(\ln\mu^2)} \tag{2.24}$$

$$\gamma(\alpha) := \frac{d\ln Z}{d(\ln\mu^2)} \tag{2.25}$$

we can rewrite equation (2.23) as

$$\left(\frac{\partial}{\partial(\ln\mu^2)} + \beta(\alpha)\frac{\partial}{\partial\alpha} + \gamma(\alpha)\right)\phi(p_i,\alpha,\mu) = 0 \tag{2.26}$$

ϕ is a function of the renormalization scale μ, which is an unphysical scale. Now, suppose we can actually measure ϕ at a physical scale Q. Let us rescale p_i and μ by Q, and define

$$\begin{gathered}
x_i := \frac{p_i}{Q}, \qquad t := \ln\frac{Q^2}{\mu^2} \\
\text{so that} \quad \phi(p_i,\alpha,\mu) = F(x_i,t,\alpha)
\end{gathered} \tag{2.27}$$

Then one gets the **renormalization group evolution equation**

$$\left(-\frac{\partial}{\partial t} + \beta(\alpha)\frac{\partial}{\partial\alpha} + \gamma(\alpha)\right)F(x_i,t,\alpha) = 0 \tag{2.28}$$

or also called the *Callan–Symanzik* equation.

$\beta(\alpha)$ and $\gamma(\mu)$ are called, respectively, the **beta function** and the **anomalous dimension**. They describe a shift in the coupling constant and field strength that compensate for the shift in the renormalization scale μ. This equation can be simply generalized to other theories by adding a β term for each coupling and a γ term for each field. For example, QED abides by the following RGE equation:

$$\left(-\frac{\partial}{\partial t} + \beta(e)\frac{\partial}{\partial e} + n\gamma_2(e) + m\gamma_3(e)\right)G^{(n,m)}(x_i,t,\alpha) = 0 \tag{2.29}$$

where e is the QED coupling, n the number of electron fields and m the number of photon fields in the Green's function $G^{(n,m)}$, and γ_2 and γ_3 the rescalings of the electron and photon fields.

As an example, let us revisit the analysis of the electromagnetic coupling in Sec. 2.1.3 from the RG viewpoint. The divergent part of the renormalization constant Z_3 computed in Eq. (2.17) determines the QED β function at one loop. According to Eq. (2.24), the variation of the coupling α with the energy scale μ is governed by the β function, calculable as a function of α. In dimensional regularization, from

$$\alpha \left(\mu^2\right)^{\varepsilon} = Z_3 \ \alpha_0 \ , \tag{2.30}$$

by using Eq. (2.17) we have

$$\begin{aligned} \frac{\partial \alpha}{\partial(\ln \mu^2)} &= -\varepsilon \left(1 - \frac{\alpha}{3\pi}\frac{1}{\varepsilon}\right) \alpha_0 \left(\mu^2\right)^{-\varepsilon} \\ &= \frac{1}{3\pi}\, \alpha^2 \ . \end{aligned} \tag{2.31}$$

The leading term of the QED β function at small coupling is given by

$$\begin{aligned} \beta(\alpha) &= b\alpha^2 + \mathcal{O}(\alpha^3) \ , \\ b &= \frac{1}{3\pi} \ . \end{aligned} \tag{2.32}$$

Inserting the result (2.32) into Eq. (2.24) gives the differential equation

$$\frac{\partial \alpha}{\partial(\ln \mu^2)} = b\alpha^2 \ . \tag{2.33}$$

This can be solved by

$$\frac{d\alpha}{\alpha^2} = b\, \frac{d\mu^2}{\mu^2} \quad \Longrightarrow \quad -\frac{1}{\alpha(q^2)} + \frac{1}{\alpha} = b \ln \frac{q^2}{q_0^2} \ , \tag{2.34}$$

which gives

$$\alpha(q^2) = \frac{\alpha}{1 - b\alpha \ln(q^2/q_0^2)} \quad , \quad b = 1/(3\pi) \quad , \tag{2.35}$$

that is, the result (2.20) derived directly in Subsec. 2.1.3.

2.3 The beta function in QCD, the QCD running coupling, the QCD scale Λ

Let us now apply renormalization to the QCD coupling. The first step is to find the renormalization constants of the relevant quantities. If A is the gluon field, ϕ the quark field, c the ghost field, and m the quark masses, then the renormalization constants are defined in

the following way:

$$A_0 = \sqrt{Z_3} A \tag{2.36}$$

$$\phi_0 = \sqrt{Z_2} \phi \tag{2.37}$$

$$c_0 = \sqrt{\tilde{Z}_3} c \tag{2.38}$$

$$m_0 = \frac{Z_m}{Z_2} m \tag{2.39}$$

The different interaction vertices must also get renormalized. Due to coupling universality, the couplings for each of these four vertices are the same. This is why we get four relations for the same two couplings:

$$Z_2 \sqrt{Z_3} g_0 = Z_1 g_s \tag{2.40}$$

$$\tilde{Z}_3 \sqrt{Z_3} g_0 = \tilde{Z}_1 g_s \tag{2.41}$$

$$Z_3 \sqrt{Z_3} g_0 = Z_{1,3} g_s \tag{2.42}$$

$$Z_3^2 g_0^2 = Z_{1,4} g_s^2 \tag{2.43}$$

with the first being the quark-gluon vertex, the second the gluon-ghost, then the cubic gluon (or three-gluon), and finally the quartic gluon (or four-gluon). Eqs. (2.40)-(2.43) lead to relations between the renormalization constants. With a little algebraic manipulation, these are given by

$$\frac{\tilde{Z}_1}{\tilde{Z}_3} = \frac{Z_1}{Z_2} = \frac{Z_{1,3}}{Z_3} = \sqrt{\frac{Z_{1,4}}{Z_3}} \tag{2.44}$$

These relations are called the *Slavnov-Taylor identities* and they can be seen as a non-abelian generalization of the Ward identity $Z_1 = Z_2$ in QED.

The next step is to evaluate the renormalization constants. By defining the renormalized QCD coupling from the quark-gluon vertex, we have

$$\alpha_s \left(\mu^2\right)^{\varepsilon} = \frac{Z_2^2}{Z_1^2} \; Z_3 \; \alpha_{s0} \;\; , \tag{2.45}$$

where α_s in the left hand side and α_{s0} in the right hand side denote, respectively, the renormalized and unrenormalized coupling. Each of the renormalization constants Z_j has a perturbation series expansion, with the coefficients of the expansion being ultraviolet divergent. In dimensional regularization the ultraviolet divergences appear as poles at $\varepsilon = 0$, so that the Z_j have the form

$$Z_j = 1 + \alpha_s \; \frac{1}{\varepsilon} \; c_j + \text{ finite } \;\; , \tag{2.46}$$

where the coefficients c_j of the divergent terms are to be calculated.

The QCD β function is defined by

$$\beta(\alpha_s) = \frac{\partial \alpha_s}{\partial \ln \mu^2} \;\; . \tag{2.47}$$

By using Eqs. (2.45) and (2.46), the β function in Eq. (2.47) evaluates to

$$\begin{aligned}\beta(\alpha_s) &= -\varepsilon\alpha_{s0}\left(\mu^2\right)^{-\varepsilon}\left[1-2(Z_1-1)+2(Z_2-1)+(Z_3-1)\right] \\ &= 2\alpha_s^2(c_1-c_2-\frac{1}{2}\,c_3)\ .\end{aligned} \tag{2.48}$$

In order to determine the one-loop coefficients c_j of the renormalization constants, and thus obtain the QCD β function at one loop, we need to compute the one-loop corrections to the quark-gluon vertex, to the quark self-energy and to the gluon self-energy.

For instance, for the gluon self-energy there are four different Feynman diagrams contributing to the gluon self-energy at one loop, as shown below.

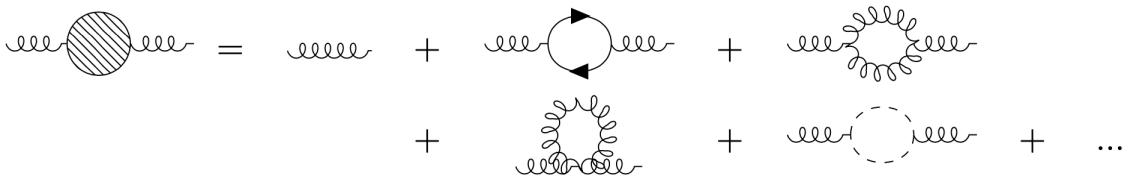

Figure 2.3: LHS: one of the primitively divergent amplitudes in QCD, called the gluon self-energy; RHS: contributions to the gluon self-energy through one loop.

The calculations for these one-loop corrections may be found in standard textbooks, and only the results are shown below. By working in Feynman gauge, we obtain

$$Z_1 = 1-\frac{\alpha_s}{4\pi}\,\frac{1}{\varepsilon}\,(C_F+C_A)\ , \tag{2.49}$$

$$Z_2 = 1-\frac{\alpha_s}{4\pi}\,\frac{1}{\varepsilon}\,C_F\ , \tag{2.50}$$

$$Z_3 = 1+\frac{\alpha_s}{4\pi}\,\frac{1}{\varepsilon}\,(\frac{5}{3}\,C_A-\frac{4}{3}\,N_fT_F)\ , \tag{2.51}$$

where N_f is the number of quark flavors and the color charge factors are

$$C_A = N_c = 3\ ,\quad C_F = \frac{N_c^2-1}{2N_c} = \frac{4}{3}\ ,\quad T_F = \frac{1}{2}\ . \tag{2.52}$$

From Eqs. (2.49)-(2.51) we read the coefficients c_j to be put into Eq. (2.48) to determine the β function. We obtain

$$\begin{aligned}\beta(\alpha_s) &= 2\alpha_s^2(c_1-c_2-\frac{1}{2}\,c_3) \\ &= 2\,\frac{\alpha_s^2}{4\pi}\left(-C_F-C_A+C_F-\frac{1}{2}\,\frac{5}{3}\,C_A+\frac{1}{2}\,\frac{4}{3}\,N_fT_F\right) \\ &= \frac{\alpha_s^2}{4\pi}\left(-\frac{11}{3}\,C_A+\frac{4}{3}\,N_fT_F\right) \\ &= -\frac{\alpha_s^2}{12\pi}\,(11N_c-2N_f)\ .\end{aligned} \tag{2.53}$$

Eq. (2.53) shows that for $N_f < 11N_c/2$ the β function in the non-abelian case has negative sign at small coupling, that is,

$$\beta(\alpha_s) = -\beta_0 \alpha_s^2 + \mathcal{O}(\alpha_s^3) \ , \tag{2.54}$$

where

$$\beta_0 = \frac{1}{12\pi}(11N_c - 2N_f) \ . \tag{2.55}$$

This sign of the β function is opposite to the sign of the β function in QED, see Eq. (2.32). The behavior of the β function in Eqs. (2.54),(2.55) implies that QCD is asymptotically free, i.e., weakly coupled at short distances. By inserting Eq. (2.54) into the renormalization group evolution equation,

$$\frac{\partial \alpha_s}{\partial \ln \mu^2} = \beta(\alpha_s) \simeq -\beta_0 \alpha_s^2 \ \ , \tag{2.56}$$

and solving Eq. (2.56), we obtain

$$\alpha_s(q^2) = \frac{\alpha_s(\mu^2)}{1 + \beta_0 \ \alpha_s(\mu^2) \ln q^2/\mu^2} \ \ , \tag{2.57}$$

where β_0 is given in Eq. (2.55). Eq. (2.57) expresses the q^2-dependence of the QCD running coupling at one loop. The QCD coupling decreases logarithmically as the momentum scale q^2 increases, as shown in Fig. 2.4. This property of asymptotic freedom is the basis for the perturbative calculability of scattering processes due to strong interactions at large momentum transfers. From Eq. (2.57) we also see that QCD becomes strongly coupled in the infrared, low-momentum region, in contrast to what happens in QED from Eq. (2.20). Figures 2.2 and 2.4 clearly demonstrate this behavior, due to the different sign in the denominator.

Calling Λ the mass scale at which the denominator in Eq. (2.57) vanishes, we have

$$1 + \beta_0 \ \alpha_s(\mu^2) \ln \frac{\Lambda^2}{\mu^2} = 0 \quad \Longrightarrow \quad \Lambda^2 = \mu^2 e^{-1/(\beta_0 \alpha_s(\mu^2))} \ . \tag{2.58}$$

The scale Λ in Eq. (2.58) is renormalization-group invariant, i.e., it is independent of μ. Under transformations

$$\begin{aligned} \mu^2 \ &\longrightarrow \ \mu'^2 = \mu^2 e^t \ , \\ \alpha_s(\mu^2) \ &\longrightarrow \ \alpha_s(\mu'^2) = \frac{\alpha_s(\mu^2)}{1 + \beta_0 \alpha_s(\mu^2) t} \ , \end{aligned} \tag{2.59}$$

we have

$$\begin{aligned} \Lambda^2 \ &\longrightarrow \ \mu'^2 e^{-1/(\beta_0 \alpha_s(\mu'^2))} \ , \\ &= \ \mu^2 e^t e^{-(1+\beta_0 \alpha_s(\mu^2) t)/(\beta_0 \alpha_s(\mu^2))} = \mu^2 e^t e^{-1/(\beta_0 \alpha_s(\mu^2))} e^{-t} = \Lambda^2 \ . \end{aligned} \tag{2.60}$$

The scale Λ is a physical mass scale of the theory of strong interactions. Its measured value is about 200 MeV. The running coupling (2.57) can be equivalently expressed in terms of this Λ,

$$\begin{aligned} \alpha_s(q^2) \ &= \ \frac{\alpha_s(\mu^2)}{1 + \beta_0 \ \alpha_s(\mu^2) \left[\ln(q^2/\Lambda^2) - 1/(\beta_0 \ \alpha_s(\mu^2))\right]} \\ &= \ \frac{1}{\beta_0 \ln(q^2/\Lambda^2)} \ \ . \end{aligned} \tag{2.61}$$

The rewriting (2.61) of Eq. (2.57) makes it manifest that the running coupling α_s does not depend on the choice of the renormalization scale μ.

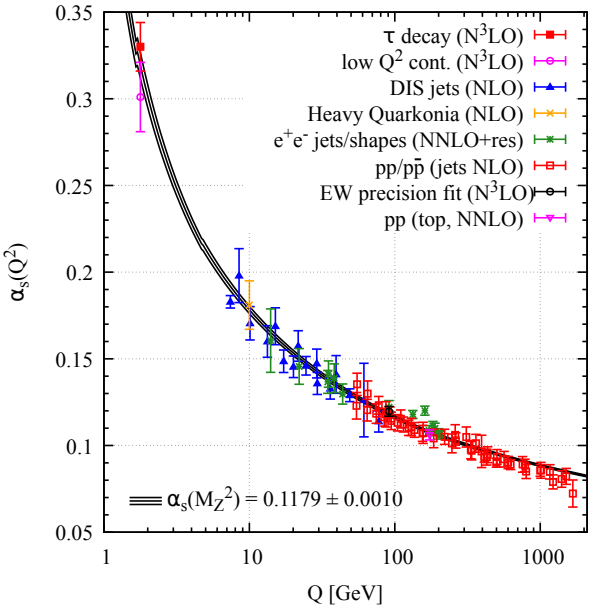

Figure 2.4: A summary of the value of the QCD running coupling at different energies with data from different experiments (Ref: P.A. Zyla et al. (Particle Data Group), Prog. Theor. Exp. Phys. 2020, 083C01 (2020)).

To finish off this section, we give a quick overview on the current experiments for obtaining α_s. Fig. 2.4 shows experiments that calculate α_s using different methods and channels. Each of these contribute by probing α_s in a new region of Q, or by confirming with other experiments with a different independent approach.

- *Low energy decays:* τ leptons decay into a τ neutrino and a W boson, which then decay into hadrons (and lepton-neutrino pairs). The decay probability $\Gamma(\tau \to \textit{hadrons})$ is related to α_s and is known up to N^{3}LO and thus provides a very precise determination of α_s at the τ mass scale ($m_\tau = 1.777$ GeV). Low Q^2 continuum refers to the incorporation of non-perturbative effects on top of perturbative ones when calculating the τ decay.

- *Heavy Quarkonia:* This category focuses on the decay of heavier quarks such as the bottom and charm quarks. The results were produced at NLO, but recently two determinations have been done at N^{3}LO.

- *Deep inelastic scattering (DIS) and PDF fits:* a combination of precision measurements at HERA, based on NLO fits to inclusive jet cross sections in neutral current DIS at high Q^2, provides combined values of α_s at different energy scales Q. Another class of studies, analyzing structure functions at NNLO QCD (and partly beyond), provides results for α_s.

- *Event shapes of e^+e^-:* Event-shape observables are quantities used to characterize the geometry of the outcome of a collision between two particles. By combining

these observables, it is possible to obtain α_s. These analyses need careful control of hadronization corrections via resummation and Monte Carlo techniques.

- *Hadron collider results:* Determinations of α_s, using jets or $t\bar{t}$ production processes, in hadron collisions are calculated at NLO. Recently though, NNLO calculations for $t\bar{t}$, dijet and inclusive jet production have become available. This advancement is interesting, because future experiments are going to higher energies and will need more precise calculations, which has now been achieved.

- *Electroweak (EW) precision fit:* The EW sector has very precise measurements of the decay width of the Z boson into hadrons. This is used to determine α_s at NNLO for EW and QCD contributions, and at partial $\mathrm{N^3LO}$ for QCD corrections.

2.4 Perturbative solution of RG equations: g-functions and resummation scales

Now let's take a look at a general scheme for solving RG equations perturbatively. From equation (2.25), the anomalous dimension is defined as

$$\frac{d\ln R(\mu)}{d\ln \mu} = \gamma(\alpha_s(\mu)) \tag{2.62}$$

where R is a renormalized quantity and μ is the renormalization scale. One can expand $\gamma(\alpha_s(\mu))$ as a power series of α_s and analyze equation (2.62) order by order.

$$\gamma(\alpha_s(\mu)) = \sum_{n=0}^{k} \left(\frac{\alpha_s(\mu)}{4\pi}\right)^{n+1} \gamma_n \tag{2.63}$$

Two equivalent approaches will be used to solve equation (2.62) **at a finite truncation order of k**. The terminology for the accuracy of γ is called leading order (LO) for $k = 0$, next-to-leading order (NLO) for $k = 1$, next-to-next-to-leading order ($\mathrm{N^2LO}$) for $k = 2$ and $\mathrm{N^kLO}$ for any order k. The first approach is by solving the equation *analytically* at some order by expressing $R(\mu)$ with boundary condition $R(\mu_0)$ in a closed analytic form. The second approach is *numerically*. An analytic solution enables fast computations to be made, but requires making use of perturbative expansions which violate equation (2.62) by subleading terms, whereas a numerical solution guarantees an exact equality between the LHS and the RHS but is computationally very time-consuming. Introducing the operator G that connects R at two scales μ and μ_0,

$$R(\mu) = G(\mu, \mu_0)R(\mu_0), \tag{2.64}$$

due to subleading terms in the analytic solution one may have for any given scale μ' that

$$G(\mu, \mu_0) \neq G(\mu, \mu')G(\mu', \mu_0). \tag{2.65}$$

This is referred to as **perturbative hysteresis** in Ref. [18]. On the other hand, the numerical solution does not show such an effect by definition.

Here, we note that both solutions are equivalent in terms of perturbative accuracy and none is more accurate than the other. However, the existence of a hysteresis is an indicator of

a theoretical uncertainty originating from other perturbative approximations. These affect any solution found using a perturbatively computed anomalous dimension. The purpose of the work described in the rest of this chapter is to investigate this uncertainty and estimate its effect on certain physical quantities.

Concretely, the analytic solution can be obtained via techniques borrowed from soft-gluon and transverse-momentum **resummation** [19, 20, 21]. This method brings along a so-called **resummation scale**, denoted by $\kappa\mu$. By varying this scale, it is possible to generate subleading terms and therefore quantify the uncertainty of the current accuracy. Expanding on this, a similar concept can be achieved with the numerical solution.

One way to generate subleading terms for the numerical solution is through scale variations. A scale is inserted by displacing μ by a factor ξ in the strong coupling $a_s(\xi\mu)$. Unlike the analytical case, the scale appears in the anomalous dimension before solving for it. To be more precise, let's consider the anomalous dimension at NLO accuracy, where $a_s := \alpha_s/4\pi$:

$$\gamma = a_s(\mu)\gamma_0 + a_s^2(\mu)\gamma_1. \tag{2.66}$$

$a_s(\mu)$ is written in its expanded form and ξ is inserted as follows,

$$a_s(\mu) = a_s(\xi\mu) - a_s^2(\xi\mu)\beta_0 \ln\xi + \mathcal{O}(\alpha_s^3). \tag{2.67}$$

Substituting (2.67) in (2.66) gives

$$\gamma = a_s(\xi\mu)\gamma_0 + a_s^2(\xi\mu)\gamma_0[\gamma_1 - \beta_0\gamma_0 \ln\xi] + \mathcal{O}(\alpha_s^3). \tag{2.68}$$

The difference between (2.66) and (2.68) can be interpreted as an estimate of the perturbative uncertainty associated to the solution of the RGE obtained using an anomalous dimension truncated at NLO accuracy. In some way, $\xi\mu$ can also be called a resummation scale, because it essentially does the same thing as $\kappa\mu$ in the analytic solution. It is shown in [22] that they indeed have a one-on-one correspondence with each other. In the calculations performed in this thesis, we will mainly use the resummation scale $\xi\mu$.

2.4.1 RGE of the strong coupling

As an example and an important foundation for other expressions, let us apply equation (2.62) to the coupling constant, with $R = a_s := \alpha_s/4\pi$ and $\gamma = \beta$:

$$\frac{d\ln a_s(\mu)}{d\ln\mu} = \beta(a_s(\mu)) = \sum_{n=0}^{k} a_s^{n+1}(\mu)\beta_n \tag{2.69}$$

The coupling is now expanded in its perturbative form around μ_0:

$$a_s(\mu) = \sum_{n=0}^{p} c_n a_s^{n+1}(\mu_0) \tag{2.70}$$

Substituting (2.70) in (2.69) gives a series of equations for each power of $a_s(\mu_0)$.

$$\begin{aligned}
\frac{dc_0}{d\ln\mu} &= 0,\\
\frac{dc_1}{d\ln\mu} &= \beta_0 c_0^2,\\
\frac{dc_2}{d\ln\mu} &= 2\beta_0 c_0 c_1 + \beta_1 c_0^3,\\
\frac{dc_3}{d\ln\mu} &= \beta_0(c_1^2 + 2c_0c_2) + 3\beta_1 c_0^2 c_1 + \beta_2 c_0^4,\\
\frac{dc_4}{d\ln\mu} &= 2\beta_0(c_0c_3 + c_1c_2) + 3\beta_1(c_0c_1^2 + c_0^2c_2) + 4\beta_2 c_0^3 c_1 + \beta_3 c_0^5,\\
&\vdots
\end{aligned}$$

Integrating these equations from μ to μ_0, and using the boundary condition $a_s(\mu_0)$ gives

$$\begin{aligned}
c_0 &= 1,\\
c_1 &= \beta_0 \ln\left(\frac{\mu}{\mu_0}\right),\\
c_2 &= \beta_0^2 \ln^2\left(\frac{\mu}{\mu_0}\right) + \beta_1 \ln\left(\frac{\mu}{\mu_0}\right),\\
c_3 &= \beta_0^3 \ln^3\left(\frac{\mu}{\mu_0}\right) + \frac{5}{2}\beta_0\beta_1 \ln^2\left(\frac{\mu}{\mu_0}\right) + \beta_2 \ln\left(\frac{\mu}{\mu_0}\right),\\
c_4 &= \beta_0^4 \ln^4\left(\frac{\mu}{\mu_0}\right) + \frac{13}{3}\beta_0^2\beta_1 \ln^3\left(\frac{\mu}{\mu_0}\right) + \left(3\beta_0\beta_2 + \frac{3}{2}\beta_1^2\right)\ln^2\left(\frac{\mu}{\mu_0}\right) + \beta_3 \ln\left(\frac{\mu}{\mu_0}\right),\\
&\vdots
\end{aligned}$$

The coefficients c_n can be calculated up to any order p, but contain terms of β_n. This means that $a_s(\mu)$ is effectively only accurate up to order k of the beta function instead of p. The current state of the art calculation of beta coefficients goes up to β_4. This is a very long and tedious task; historically, it took around ten years to calculate the next order of beta coefficient. They are summarized here [23] [24]:

$$
\begin{aligned}
\beta_0 &= 11 - \frac{2}{3}n_f \\
\beta_1 &= 102 - \frac{38}{3}n_f \\
\beta_2 &= \frac{2857}{2} - \frac{5033}{18}n_f + \frac{325}{54}n_f^2 \\
\beta_3 &= \frac{149753}{6} + 3564\zeta_3 - n_f\left[\frac{1078361}{162} + \frac{6508}{27}\zeta_3\right] + n_f^2\left[\frac{50065}{162} + \frac{6472}{81}\zeta_3\right] + \frac{1093}{729}n_f^3 \\
\beta_4 &= \frac{8157455}{16} + \frac{621885}{2}\zeta_3 - \frac{88209}{2}\zeta_4 - 288090\zeta_5 \\
&\quad + n_f\left[\frac{336460813}{1944} - \frac{4811164}{81}\zeta_3 + \frac{33935}{6}\zeta_4 + \frac{1358995}{27}\zeta_5\right] \\
&\quad + n_f^2\left[\frac{25960913}{1944} + \frac{698531}{81}\zeta_3 - \frac{10526}{9}\zeta_4 - \frac{381760}{81}\zeta_5\right] \\
&\quad + n_f^3\left[-\frac{630559}{5832} - \frac{48722}{243}\zeta_3 + \frac{1618}{27}\zeta_4 + \frac{460}{9}\zeta_5\right] \\
&\quad + n_f^4\left[\frac{1205}{2916} - \frac{152}{81}\zeta_3\right]
\end{aligned}
$$

with n_f the number of flavours and ζ_n the Riemann zeta values.

On top of the restriction by β_n, the coefficients c_n can become arbitrarily large due to terms such as $\ln^n(\mu/\mu_0)$. This makes the perturbative expansion of $a_s(\mu)$ possibly unvalid, which calls for a need to collect all the terms and *resum* the $a_s(\mu)$ expansion to all orders. This process is called *resummation* and can be done in different ways according to the physical context, logarithms, and the desired precision, and will not be tackled in detail. We hereby also introduce a **resummation scale** $\kappa\mu$ by adding and subtracting a κ-term for each logarithm:

$$
a_s(\mu_0)\ln\left(\frac{\mu}{\mu_0}\right) = a_s(\mu_0)\ln\left(\frac{\kappa\mu}{\mu_0}\right) - a_s(\mu_0)\ln\kappa. \tag{2.71}
$$

κ is of order $\mathcal{O}(1)$, so that the second term is perturbatively small.

Let us consider the solution of Eq. (2.69) at successive orders of logarithmic accuracy. At leading order ($k = 0$), Eq. (2.69) can be solved in closed form, giving the leading-logarithmic (LL) *resummation* of the running coupling:

$$
a_s^{\mathrm{LL}}(\mu) = \frac{a_s(\mu_0)}{1 - a_s(\mu_0)\beta^{(0)}\ln(\mu/\mu_0)}\,. \tag{2.72}
$$

Beyond leading order ($k \geq 1$), Eq. (2.69) gives rise to a transcendental equation and cannot be solved in closed form, so that one has to resort to either a numerical or an analytic solution based on perturbative expansions. For $k = 1$ we have the transcendental equation in $a_s(\mu)$

$$
\beta^0\ln\left(\frac{\mu}{\mu_0}\right) = -\frac{1}{a_s(\mu)} + \frac{1}{a_s(\mu_0)} + b_1\ln\left(\frac{a_s(\mu_0)(1 + a_s(\mu)b_1)}{a_s(\mu)(1 + a_s(\mu_0)b_1)}\right)\,, \tag{2.73}
$$

where $b_n = \beta^{(n)}/\beta^{(0)}$. This can be rearranged as

$$
a_s(\mu) = a_s(\mu_0)\left[1 - a_s(\mu_0)\beta^{(0)}\ln\left(\frac{\mu}{\mu_0}\right) + a_s(\mu_0)b_1\ln\left(\frac{a_s(\mu_0)(1 + a_s(\mu)b_1)}{a_s(\mu)(1 + a_s(\mu_0)b_1)}\right)\right]^{-1}\,, \tag{2.74}
$$

which yields

$$a_s(\mu) = \frac{a_s^{\rm LL}(\mu)}{1 + a_s^{\rm LL}(\mu) b_1 \ln\left(a_s(\mu_0)/a_s^{\rm LL}(\mu)\right)} + \mathcal{O}(\alpha_s^3)\,. \tag{2.75}$$

By further expanding Eq. (2.75), we obtain the analytic next-to-leading-logarithmic (NLL) expression for the strong coupling

$$a_s^{\rm NLL}(\mu) = a_s^{\rm LL}(\mu) - \left(a_s^{\rm LL}(\mu)\right)^2 b_1 \ln\left(\frac{a_s(\mu_0)}{a_s^{\rm LL}(\mu)}\right)\,. \tag{2.76}$$

The above procedure can be applied to higher k as well. For example, for $k = 2$ we obtain the analytic next-to-next-to-leading-logarithmic (NNLL) result

$$\begin{aligned} a_s^{\rm NNLL}(\mu) &= a_s^{\rm LL}(\mu) - \left(a_s^{\rm LL}(\mu)\right)^2 b_1 \ln\left(\frac{a_s(\mu_0)}{a_s^{\rm LL}(\mu)}\right) + \left(a_s^{\rm LL}(\mu)\right)^3 \left[b_2 \left(1 - \frac{a_s(\mu_0)}{a_s^{\rm LL}(\mu)}\right)\right. \\ &- \left. b_1^2 \left(1 - \frac{a_s(\mu_0)}{a_s^{\rm LL}(\mu)} + \ln\left(\frac{a_s(\mu_0)}{a_s^{\rm LL}(\mu)}\right) - \ln^2\left(\frac{a_s(\mu_0)}{a_s^{\rm LL}(\mu)}\right)\right)\right]\,. \end{aligned} \tag{2.77}$$

Note however that the procedure to arrive at Eq. (2.76) or Eq. (2.77) implies perturbative expansions at the level of the RGE. For instance, comparing the expressions in Eq. (2.76) and Eq. (2.73), we recognize that they are equivalent from the standpoint of NLL perturbative accuracy but, while Eq. (2.73) exactly satisfies the RGE in Eq. (2.69) with $k = 1$, Eq. (2.76) violates it by subleading terms. That is, one has

$$\frac{d \ln a_s^{\rm NLL}(\mu)}{d \ln \mu} = a_s^{\rm NLL}(\mu)\beta^{(0)} + (a_s^{\rm NLL}(\mu))^2 \beta^{(1)} + \mathcal{O}(\alpha_s^3)\,. \tag{2.78}$$

As a consequence, Eq. (2.76) bears the feature that, by evolving α_s from μ_0 to μ and then back from μ to μ_0 one does not reobtain the initial value. This behavior is referred to as perturbative hysteresis in Ref. [18]. Fig. 1 of Ref. [18] illustrates this quantitatively with a numerical example.

To describe the hysteresis and model the influence of (uncalculated) higher-order contributions to the RGE, it is useful to recast the solution for the running coupling in terms of the so-called g-functions and resummation scales. To this end, on the right hand side of Eq. (2.72) we decompose the product of the beta function coefficient, the strong coupling at scale μ_0 and the logarithm of the ratio μ/μ_0 as follows,

$$a_s(\mu_0)\beta^{(0)} \ln\left(\frac{\mu}{\mu_0}\right) = \lambda - a_s(\mu_0)\beta^{(0)} \ln\kappa\,, \tag{2.79}$$

where

$$\lambda = a_s(\mu_0)\beta^{(0)} \ln\left(\frac{\mu_{\rm Res}}{\mu_0}\right)\,, \quad \kappa = \frac{\mu_{\rm Res}}{\mu}\,, \tag{2.80}$$

and $\mu_{\rm Res}$ is the resummation scale, taken to be of order μ but otherwise arbitrary. Thus, we have $\kappa \sim \mathcal{O}(1)$. Next, for arbitrary order k in Eq. (2.69), we write the solution for $a_s(\mu)$ as a power series expansion in $a_s(\mu_0)$, by iterating the procedure described earlier in this section. This gives

$$a_s^{{\rm N}^k{\rm LL}}(\mu) = \sum_{l=0}^{k} a_s^{l+1}(\mu_0) g_{l+1}^{(\beta)}(\lambda, \kappa) \tag{2.81}$$

where the coefficients $g^{(\beta)}$ can be determined explicitly, order by order, as functions of the variables λ and κ introduced in Eq. (2.80). k still determines the truncation of the beta function and LL in N^{k}LL stands for "leading-logarithm", because the resummation reorders new terms according to their logarithm. The first three functions $g^{(\beta)}$ are given by

$$\begin{aligned} g_1^{(\beta)}(\lambda,\kappa) &= \frac{1}{1-\lambda}\,, \\ g_2^{(\beta)}(\lambda,\kappa) &= -\frac{b_1\ln(1-\lambda)+\beta^{(0)}\ln\kappa}{(1-\lambda)^2}\,, \\ g_3^{(\beta)}(\lambda,\kappa) &= \Big[b_2\lambda - b_1^2\left(\lambda+\ln(1-\lambda)-\ln^2(1-\lambda)\right) \\ &+ \beta^{(0)}b_1\left(2\ln(1-\lambda)-1\right)\ln\kappa + (\beta^{(0)})^2\ln^2\kappa\Big]/(1-\lambda)^3\,, \end{aligned} \tag{2.82}$$

One may verify that Eqs. (2.72), (2.76), and (2.77) coincide, up to subleading orders, with the first three terms of the expansion (2.81).

An alternative strategy to the one described above is to solve Eq. (2.69) at order k numerically. It remains possible to estimate higher-order corrections to the β function also when using the numerical solution. This can be done by performing scale variations at the level of the β function. To be specific, by displacing the scale μ by a factor ξ we obtain

$$\begin{aligned} \beta(\alpha_s(\mu)) = a_s(\xi\mu)\beta_0\Big[1 + a_s(\xi\mu)(b_1-2\beta_0\ln\xi) + a_s^2(\xi\mu)\left(-5b_1\beta_0\ln\xi+3\beta_0^2\ln^2\xi+b_2\right) \\ + a_s^3(\xi\mu)\left(13b_1\beta_0^2\ln^2\xi - 3b_1^2\beta_0\ln\xi - 6b_2\beta_0\ln\xi - 4\beta_0^3\ln^3\xi + b_3\right)\Big] + \mathcal{O}(\alpha_s^5), \end{aligned} \tag{2.83}$$

where $b_n = \beta_n/\beta_0$. This effectively defines a new β-function that differs from the original one by subleading corrections. The difference between the solution obtained with the original $\beta(\mu)$ and that obtained with Eq. (2.83) gives an estimate of the effect of higher-order corrections to the RGE kernel, much as variations of the resummation scale do for the analytic solution.

In fact, at NLL accuracy the β-function corresponding to the analytic solution (2.81) can be recast in the same form as Eq. (2.83) by setting $\kappa = \xi$. To see this, let us denote by $a_s^{\rm NLL}(\mu,\kappa)$ the coupling computed analytically at the scale μ with resummation scale set to $\kappa\mu$, so that

$$a_s^{\rm NLL}(\mu,\kappa) = a_s^{\rm NLL}(\kappa\mu,1) - \left(a_s^{\rm LL}(\kappa\mu,1)\right)^2\beta^{(0)}\ln\kappa\,. \tag{2.84}$$

Taking the logarithmic derivative with respect to $\ln\mu$, one gets

$$\frac{d\ln a_s^{\rm NLL}(\mu,\kappa)}{d\ln\mu} = a_s^{\rm NLL}(\kappa\mu,1)\beta^{(0)} + \left(a_s^{\rm LL}(\kappa\mu,1)\right)^2\left[\beta^{(1)} - 2\left(\beta^{(0)}\right)^2\ln\kappa\right] + \mathcal{O}(\alpha_s^3)\,, \tag{2.85}$$

where the higher-order terms are the same as those neglected in Eq. (2.78). The right hand side of Eq. (2.85) coincides with the right hand side of Eq. (2.83) provided that $\kappa = \xi$.

One unfortunate feature of the beta function in Eq. (2.83) is that $\beta(\alpha_s(\mu))$ is dependent on $\alpha_s(\xi\mu)$. This gives rise to a "retarded" or an "advanced" differential equation, which is more difficult to solve. To get rid of this, the analytic solution from (2.81) can be used to write $\alpha_s(\xi\mu)$ in terms of $\alpha_s(\mu)$. Both solutions and its variations are shown and compared in figure 2.5, taken from [22].

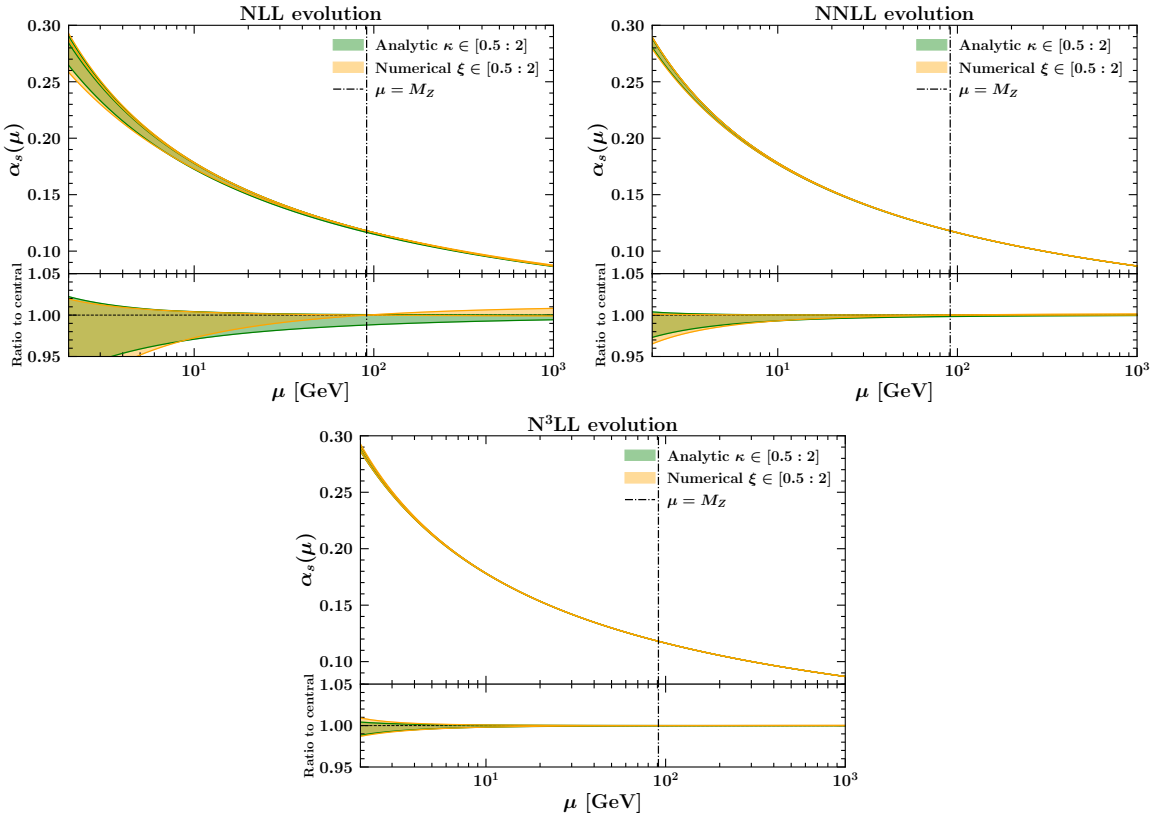

Figure 2.5: α_s is calculated in the range [2:1000] GeV at NLL (top-left plot), NNLL (top-right plot) and N^{3}LL (bottom plot) accuracies. The bands contain every curve with a different κ and ξ in the range [0.5:2]. The bottom panel in each plot shows the ratio-to-central value, which calculates the ratio of the current value with the one obtained with $\kappa = \xi = 1$ (no variation). The dotted line shows the boundary condition chosen at $\mu = M_Z$.

The size difference between the analytic and numerical case is relatively small in each plot, which suggests a link between the two. In both cases, the bands shrink the higher the accuracy. The numerical plot goes to zero uncertainty at $\mu = M_Z$ because of the chosen boundary condition, where there is no theoretical uncertainty. This feature is not shared by the analytic solution.

2.4.2 RGE of parton distribution function (PDF)

In this section, the same scheme will be applied on a Mellin moment of flavour non-singlet collinear PDF f. Similarly to (2.69), equation (2.62) now becomes

$$\frac{d \ln f(\mu)}{d \ln \mu} = \gamma(\alpha_s(\mu)) \tag{2.86}$$

As in the case of the running coupling in the previous subsection, an analytic solution to the RGE can only be obtained by relying on perturbative expansions. Using the perturbation expansion of γ in Eq. (2.63), we obtain the following solution for the PDF f at the scale μ in

terms of f at scale μ_0,

$$\begin{aligned} f(\mu) &= \exp\left[\int_{\mu_0}^{\mu} d\ln\mu'\,\gamma(a_s(\mu'))\right] f(\mu_0) \\ &= \exp\left[\sum_{n=0}^{k}\gamma^{(n)}\int_{\mu_0}^{\mu} d\ln\mu'\,a_s^{n+1}(\mu')\right] f(\mu_0) \\ &= \prod_{n=0}^{k}\exp\left[\gamma^{(n)}I_n\right]\, f(\mu_0), \end{aligned} \tag{2.87}$$

with

$$\begin{aligned} I_n &= \int_{\mu_0}^{\mu} d\ln\mu'\,a_s^{n+1}(\mu') \\ &= \int_{a_s(\mu)}^{a_s(\mu_0)} \frac{da_s\,a_s^{n+1}}{2\beta(a_s)}\,, \end{aligned} \tag{2.88}$$

where in the second line of Eq. (2.88) we have used the β function (2.69).

We note that, for $n \geq 1$, $I_n = \mathcal{O}(\alpha_s^n)$, so that the exponential in Eq. (2.87) can be expanded as

$$\exp\left[\gamma^{(n)}I_n\right] = 1 + \gamma^{(n)} \times \mathcal{O}(\alpha_s^n)\,, \quad n \geq 1\,, \tag{2.89}$$

while, for $n = 0$, I_0 cannot be expanded due to the presence of a logarithm of $a_s(\mu)/a_s(\mu_0)$ which, as can be seen from Eq. (2.72), is potentially large,

$$\exp\left[\gamma^{(0)}I_0\right] = \exp\left[\frac{\gamma^{(0)}}{\beta^{(0)}}\ln\left(\frac{a_s(\mu)}{a_s(\mu_0)}\right)\right] + \mathcal{O}(\alpha_s) = \left(\frac{a_s(\mu)}{a_s(\mu_0)}\right)^{\frac{\gamma^{(0)}}{\beta^{(0)}}} + \mathcal{O}(\alpha_s)\,. \tag{2.90}$$

To achieve N^{k}LL accuracy for the evolution of the PDF, the contributions in both Eq. (2.90) and Eq. (2.89) are required to the corresponding order. The former depends on higher-order contributions to the β function, while the latter depends on higher-order contributions to both the β and γ functions.

For example, the solution at NLL accuracy can be written as

$$f^{\rm NLL}(\mu) = \left[1 + \frac{1}{\beta^{(0)}}\left(\gamma^{(1)} - b_1\gamma^{(0)}\right)\left(a_s^{\rm LL}(\mu) - a_s(\mu_0)\right)\right]\left(\frac{a_s^{\rm NLL}(\mu)}{a_s(\mu_0)}\right)^{\frac{\gamma^{(0)}}{\beta^{(0)}}} f(\mu_0)\,. \tag{2.91}$$

In the square bracket, a_s can be replaced by $a_s^{\rm LL}$ because the difference is $\mathcal{O}(\alpha_s^2)$, *i.e.* N^{2}LL. For the same reason, $a_s(\mu)$ in the last factor has to be computed using NLL evolution. The analytic solution (2.91) fulfills

$$\frac{d\ln f^{\rm NLL}(\mu)}{d\ln\mu^2} = [a_s(\mu)\gamma^{(0)} + a_s^2(\mu)\gamma^{(1)}] + \mathcal{O}(\alpha_s^3)\,, \tag{2.92}$$

that is, it obeys the RGE up to subleading $\mathcal{O}(\alpha_s^3)$ terms. In Ref. [18], this is related to the onset of hysteresis in PDF evolution.

To model the effect of (uncalculated) higher-order contributions to the RGE and describe hysteresis, it is useful to recast the solution for the collinear PDF in terms of g-functions and resummation scales. To do this, we employ the variables λ and κ introduced in Eq. (2.80). Using the structure of the evolution in Eq. (2.87), the solution of the RGE at perturbative order k can be written as

$$\boxed{f^{\mathrm{N^kLL}}(\mu) = g_0^{(\gamma),\mathrm{N^kLL}}(\lambda,\kappa)\exp\left[\sum_{l=0}^{k} a_s^l(\mu_0) g_{l+1}^{(\gamma)}(\lambda,\kappa)\right] f(\mu_0),} \tag{2.93}$$

where the coefficients $g_n^{(\gamma)}$ can be determined as functions of the λ and κ variables (2.80). The $g_n^{(\gamma)}$ for $n \geq 1$ can equivalently be expressed in terms of the coefficients $g^{(\beta)}$ in Eq. (2.82). The functions $g_n^{(\gamma)}$ through N^{2}LL accuracy are given by

$$\begin{aligned} g_0^{(\gamma),\mathrm{N^3LL}}(\lambda,\kappa) &= 1 + \frac{a_s(\mu_0)\lambda}{\beta^{(0)}(1-\lambda)}\left(\gamma^{(1)} - b_1\gamma^{(0)}\right) + \frac{a_s^2(\mu_0)}{2\beta^{(0)}(1-\lambda)^2} \\ &\times \Big[\lambda(\lambda-2)\left(\gamma^{(2)} - b_1\gamma^{(1)} + \left(b_1^2 - b_2\right)\gamma^{(0)}\right) + \lambda^2(\gamma^{(1)} - b_1\gamma^{(0)})^2/\beta^{(0)} \\ &- 2\left(\gamma^{(1)} - b_1\gamma^{(0)}\right)\left(b_1\ln(1-\lambda) + \beta^{(0)}\ln\kappa\right)\Big] \\ &+ \mathcal{O}(a_s^3(\mu_0))\,, \end{aligned} \tag{2.94}$$

$$\begin{aligned} g_1^{(\gamma)}(\lambda,\kappa) &= \frac{\gamma^{(0)}}{\beta^{(0)}}\ln\left(g_1^{(\beta)}(\lambda)\right) = -\frac{\gamma^{(0)}}{\beta^{(0)}}\ln(1-\lambda)\,, \\ g_2^{(\gamma)}(\lambda,\kappa) &= \frac{\gamma^{(0)}}{\beta^{(0)}}\frac{g_2^{(\beta)}(\lambda)}{g_1^{(\beta)}(\lambda)} = -\frac{\gamma^{(0)}}{\beta^{(0)}}\frac{b_1\ln(1-\lambda) + \beta^{(0)}\ln\kappa}{1-\lambda}\,, \\ g_3^{(\gamma)}(\lambda,\kappa) &= \frac{\gamma^{(0)}}{\beta^{(0)}}\left[\frac{g_3^{(\beta)}(\lambda)}{g_1^{(\beta)}(\lambda)} - \frac{1}{2}\left(\frac{g_2^{(\beta)}(\lambda)}{g_1^{(\beta)}(\lambda)}\right)^2\right] \\ &= \frac{\gamma^{(0)}}{\beta^{(0)}}\left[b_2\lambda - b_1^2\left(\lambda + \ln(1-\lambda) - \frac{1}{2}\ln^2(1-\lambda)\right)\right. \\ &+ \left.\beta^{(0)}b_1\left(\ln(1-\lambda) - 1\right)\ln\kappa + \frac{1}{2}\left(\beta^{(0)}\right)^2\ln^2\kappa\right]/(1-\lambda)^2\,. \end{aligned} \tag{2.95}$$

The $g^{(\gamma)}$ functions in Eq. (2.93) are written in terms of the variables given in Eq. (2.80), automatically allowing for resummation scale variations. Such variations can be used to probe higher-order corrections to the γ anomalous dimensions.

Analogously to the case of the running coupling in the previous subsection, if we take numerical solutions to the RGE it is still possible to estimate the influence of higher-order corrections to the anomalous dimension γ by varying by a factor ξ the argument of the strong coupling α_s in the expansion of γ. This effectively defines a new anomalous dimension differing from the previous one by subleading terms. For example, at NNLL this leads to

$$\begin{aligned} \gamma(\alpha_s(\mu)) &= a_s(\xi\mu)\gamma_0 + a_s^2(\xi\mu)\gamma_0[\gamma_1 - \beta_0\ln\xi] \\ &+ a_s^3(\xi\mu)\Big[\gamma_2 - (\beta_1\gamma_0 + 2\beta_0\gamma_1)\ln\xi + \beta_0^2\gamma_0\ln^2\xi\Big] + \mathcal{O}(\alpha_s^4). \end{aligned} \tag{2.96}$$

By this technique, Ref. [18] evaluates hysteresis effects in PDFs, and presents RGE uncertainty bands from resummation scale variations in the case of the analytic solution and the numerical solution (see Figs. 3 and 4 of Ref. [18]).

One can relate the variation parameterized by κ in the analytic solution (2.93) with that parameterized by ξ in the numerical solution. Let us denote by $f^{\rm NLL}(\mu,\kappa)$ the PDF computed analytically at NLL at the scale μ with resummation scale set to $\kappa\mu$. Then

$$f^{\rm NLL}(\mu,\kappa) = f^{\rm NLL}(\kappa\mu,1)\exp\left[-\gamma^{(0)}a_s^{\rm LL}(\kappa\mu)\ln\kappa\right]\,, \tag{2.97}$$

so that

$$\frac{d\ln f^{\rm NLL}(\mu,\kappa)}{d\ln\mu} = a_s^{\rm NLL}(\xi\mu)\gamma^{(0)} + \left(a_s^{\rm LL}(\xi\mu)\right)^2\left[\gamma^{(1)} - \beta^{(0)}\gamma^{(0)}\ln\kappa\right] + \mathcal{O}(\alpha_s^3)\,. \tag{2.98}$$

The right hand side of this equation can be identified with that of Eq. (2.96) if $\xi=\kappa$. This is consistent with the numerical results of [18, 22] that similar uncertainty bands are found from scale variations in the analytic and numerical solutions.

2.4.3 RGE for the Sudakov form factor

The method described in the previous sections for the strong coupling and the PDFs can also be applied to the Sudakov form factor, which controls the evolution of transverse-momentum-dependent (TMD) parton distributions [25]. These distributions are generalizations of the PDFs, and they extend the one-dimensional, longitudinal picture of hadron structure embodied by the PDFs to include transverse degrees of freedom and provide a full three-dimensional (3D) tomography of hadrons. TMD distributions have wide applications in contemporary particle and nuclear physics. They are however outside the main subject area of this thesis. For this reason, we do not describe the case of Sudakov evolution and TMDs in detail here; rather, we limit ourselves to giving a brief discussion to illustrate basic concepts and provide relevant references to current applications of TMDs and studies of 3D hadron structure.

The TMD parton distributions can be defined analogously to the case of the ordinary parton distributions, PDFs, in terms of matrix elements of bilocal field operators [26, 27, 28, 29, 30], with the main difference that they now depend on three, rather than two, variables, x, k_T and μ. Owing to the additional k_T dependence, extra singularities appear in the TMD distributions compared to the case of ordinary PDFs, that is, the rapidity, or endpoint, singularities [31, 32]. Appropriate methods to treat them, based on subtraction [33, 34] or cut-off [27, 28] techniques, are required. The TMD distribution F satisfies the evolution equations [12]

$$\begin{aligned}\frac{\partial\ln F}{\partial\ln\sqrt{\zeta}} &= \bar{K}(\mu)\\ \frac{\partial\ln F}{\partial\ln\mu} &= \gamma(\mu,\zeta)\end{aligned} \tag{2.99}$$

where γ and $\overline{K}$ are the anomalous dimensions of the evolution in the mass μ and rapidity $\sqrt{\zeta}$, respectively. The γ and $\overline{K}$, in turn, satisfy

$$\frac{d\overline{K}}{d\ln\mu} = \frac{d\gamma}{d\ln\sqrt{\zeta}} = -\gamma_K(a_s(\mu))\,, \tag{2.100}$$

where γ_K is the cusp anomalous dimension. Eq. (2.100) can be solved for $\overline{K}$ and γ, using appropriate boundary conditions at scales $\mu = \mu_b$ and $\zeta = \mu^2$, yielding

$$\begin{aligned} \overline{K}(\mu) &= K(a_s(\mu_b)) - \int_{\mu_b}^{\mu} \frac{d\mu'}{\mu'} \gamma_K(a_s(\mu'))\,, \\ \gamma(\mu,\zeta) &= \gamma_F(a_s(\mu)) - \gamma_K(a_s(\mu)) \ln \frac{\sqrt{\zeta}}{\mu}\,, \end{aligned} \tag{2.101}$$

with $K(a_s(\mu_b)) = \overline{K}(\mu_b)$ and $\gamma_F(a_s(\mu)) = \gamma(\mu, \mu^2)$.

The solution to the evolution equations for the TMD distribution can be written as

$$F(M, M^2) = \exp\left[\frac{1}{2} S(M, \mu_b)\right] F(\mu_b, \mu_b^2) \tag{2.102}$$

where $S(M, \mu_b)$ is called the *Sudakov form factor*, and is given by

$$S(M, \mu_b) = 2K(a_s(\mu_b)) \ln \frac{M}{\mu_b} + 2\int_{\mu_b}^{M} \frac{d\mu'}{\mu'} \left[\gamma_F(a_s(\mu')) - \gamma_K(a_s(\mu')) \ln \frac{M}{\mu'}\right] \tag{2.103}$$

As mentioned above, the same method described earlier for α_s and for the PDFs can be, and has been [22], employed to study the perturbative hysteresis of the Sudakov form factor, and to evaluate RGE systematic uncertainties on TMD distributions, arising from both the analytic and the numerical solutions of the corresponding evolution equations. One special feature of Sudakov evolution, compared to the cases of the coupling and the PDFs, is its double-logarithmic nature: while the evolution equations for the coupling and the PDFs resum, to all orders of perturbation theory, logarithmic towers with the structure of one logarithm for each power of α_s, the evolution equations (2.99) resum logarithmic towers with the structure of two logarithms for each power of α_s.

One of the primary applications of Sudakov evolution and TMD distributions is to the transverse momentum spectra of electroweak vector bosons in Drell-Yan (DY) [35] production of lepton pairs in hadron-hadron collisions [36, 37, 38]. Events with DY lepton pairs are used for a wide range of collider physics studies, from precision electroweak measurements to PDF determinations (in particular, from DY asymmetries [39, 40, 41, 42, 43, 44, 45, 46]) to searches for Beyond-Standard-Model signals (for instance, in models with new heavy gauge bosons [47, 48, 49, 50] and in Standard Model Effective Field Theory [51, 52]). TMD perturbative resummations and nonperturbative distribution functions dominate the kinematic regions in which the lepton-pair transverse momentum q_T is small compared to the lepton-pair invariant mass M.

Small-q_T DY distributions were originally investigated in [53, 54, 55, 56, 57]. Phenomenological studies of these distributions are performed at present using a variety of computational approaches. These include, for instance, event generators [58, 59, 60, 61, 62, 63] based on the CSS [57] analytic resummation methodology in transverse coordinate space; event generators [64, 65, 66, 67, 68, 69] based on the soft-collinear effective theory; Monte Carlo calculations based on the parton-branching (PB) TMD methodology [70, 71, 72, 73, 74]; Monte Carlo calculations based on resummation in momentum space [75, 76]; determinations of TMD parton distributions from fits to DY experimental data based on CSS [77, 78, 79, 80] or PB TMD [81, 82, 83, 84, 85] approaches. Investigations of the rapidity evolution kernel in

Eq. (2.99) and its nonperturbative contributions are also being carried out, e.g. by lattice [86, 87, 88, 89, 90] and PB TMD methods [91, 92].

Besides the case of color-singlet final states such as DY production, the application of TMDs to final states involving jets is also starting to be investigated, see e.g. [93, 94, 95, 96, 97, 98].

To this end, Monte Carlo event generators based on parton-shower algorithms and including TMD distributions are being developed [99, 100, 101, 102, 103, 104].

A web-based library which collects fits and parameterizations for TMD parton distributions, providing a platform for studies of 3D hadron structure, is available [105, 106], in a similar style to the PDF library [107].

2.5 Summary and outlook

In this chapter, after a brief description of renormalization from the perspective of renormalization group equations (RGE) we have discussed the role of RGE solutions in applications of QCD to high-energy collider physics, focusing on the cases of the strong coupling, the PDFs, and the Sudakov form factor.

In the rest of this thesis, we will perform detailed studies of the physical effects of RGE solutions illustrated in this chapter, especially in Secs. 2.4.1 and 2.4.2. In particular, we will investigate their impact on theoretical predictions for specific collider observables, namely, the DIS structure functions introduced in Sec. 1.2. These structure functions play an essential role in modern particle physics to extract information on PDFs of protons and other hadrons from experimental data.

Chapter 3

RGE Systematics in DIS

In this chapter we apply the method for RGE perturbative solutions, described in Sec. 2.4, to the study of RGE systematic uncertainties in deep inelastic scattering (DIS) structure functions, discussed in Sec. 1.2. We start by illustrating the motivation and outline of our studies; then we present results for the F_2 structure function and F_L longitudinal structure function, first at next-to-next-to-leading order (NNLO), and then at N^{3}LO.

3.1 Motivation and outline

Many applications of QCD to physics at high-energy colliders involve the solution of RGEs. In the present era of high-precision collider physics, theoretical systematic uncertainties from RGE solutions become an important factor in determining the overall accuracy of theoretical predictions for collider processes.

In the previous chapter we have studied these systematics in the cases of the QCD coupling α_s and the PDFs, respectively in Sec. 2.4.1 and Sec. 2.4.2, using the method of Refs. [18, 22] to evaluate the perturbative uncertainty associated with the solution of the corresponding RGEs.

In this chapter we apply this method to study the impact of RGE systematics on the DIS structure functions introduced in Sec. 1.2.2. These structure functions are important for current determinations of proton's PDF from global fits [108, 109, 110, 111, 112, 113, 114, 115, 116] to collider data, as well as for extractions from future collider experiments [117, 118, 119, 120]. As discussed in Refs. [18, 121, 122], the fact that modern PDF fits do not account for these systematics is likely to lead to an underestimate of their uncertainties.

The presence of logarithmically-enhanced higher-order contributions to the RGE kernels for PDF evolution at small values of Bjorken's $x_{\rm B}$ [123, 124] underlines the relevance of these systematics. While these effects can be tamed by means of dedicated resummation techniques [124, 125, 126, 127, 128, 129, 130, 131, 132, 133] based on QCD high-energy factorization [134, 135, 136], a reliable estimate of RGE theoretical uncertainties is essential to assess the applicability region of fixed-order calculations.

Furthermore, the estimate of theoretical RGE uncertainties in DIS at small $x_{\rm B}$ is important for the investigation of various approaches to parton saturation, see e.g. [137, 138, 139, 140, 141, 142, 143, 144] for recent works.

In the studies that follow, the concepts of RGE systematics described in Secs. 2.4.1 and

2.4.2 are applied to quantities such as the total structure function F_2 (see Eqs. (1.23),(1.26)) and the longitudinal structure function F_L (see Eqs. (1.25),(1.26)). For these studies, the splitting functions, given in Eqs. (1.49) and (1.53), and hard scattering functions, given in Eqs. (1.41) and (1.42), have been calculated at LO [14, 15, 16], NLO [145, 146], NNLO [147, 148] and, recently, N^{3}LO [149, 150, 151, 152, 153]. Each order corresponds to the number of loops taken into account. Recent extractions of PDFs from global fits at N^{3}LO are performed in [154, 155, 156, 157].

The results which we will obtain are computed using the dedicated software provided in the code APFEL++ [158], which itself is a C++ rewriting of the Fortran 77 code APFEL [159]. APFEL is an open-source software devoted to computing solutions of the DGLAP evolution equations. The new rewriting allows for more efficient performance and a wider range of tasks, such as solving the RG equations, more specifically those for PDFs. The software can be easily run on a personal computer.

Our results through NNLO agree with results presented in [18, 22]. Our results at N^{3}LO are new.

To present results of the resummation scale formalism, we will choose one of the standard available PDF sets, which are collected in the LHAPDF library [107] and may be found at `https://www.lhapdf.org/pdfsets.html`. The set used throughout this thesis as a default set will be *MSHT20nnlo_as118* [111]. While the detailed numerics depends on the chosen PDF set, the main qualitative features of the results are independent of this, and apply to any of the standard available PDF sets.

In the next sections, plots will be shown for F_2 and F_L with different parameters, scales and at different orders. Alternatively, the transversal structure function F_T can also be found by subtracting F_L from F_2.

3.2 Resummation scale uncertainties in the F_2 DIS structure function

In this section we perform numerical calculations, using the code APFEL++ [158], for the DIS structure function F_2, introduced in Eqs. (1.22),(1.26), through NNLO and estimate the size of its theoretical uncertainties by means of variations of the resummation-scale parameter ξ (introduced in Sec. 2.4), the factorisation scale $\mu_{\rm F}$ and the renormalisation scale $\mu_{\rm R}$ (introduced in Secs. 1.2, 2.2 and 2.3).

3.2.1 Behaviour of the F_2 structure function in x and Q^2

We begin by showing what F_2 looks like on different scales without variations. In the first graph in figure 3.1, every curve of F_2 starts from $Q_0 = 2$ GeV and evolves to $Q = 5, 15, 50, 150, 500$ GeV. The second graph in figure 3.1 shows the evolution of F_2 starting from $Q_0 = 2$ GeV, for some fixed value of $x = 10^{-5}, 10^{-3}, 0.1, 0.5, 0.9$. There exists a graph for each order of calculation, but because the difference does not change the qualitative behaviour of the curves versus x and Q^2, we only show it at NLO for a general idea of the shape.

The calculations are done by using the factorisation formula for F_2 in Eq. (1.41), with hard scattering coefficient functions given by perturbative expansions in Eq. (1.42) and PDFs

given by solutions of the RG evolution equations in Eq. (1.49). This is thus how the evolution of the F_2 structure function is obtained.

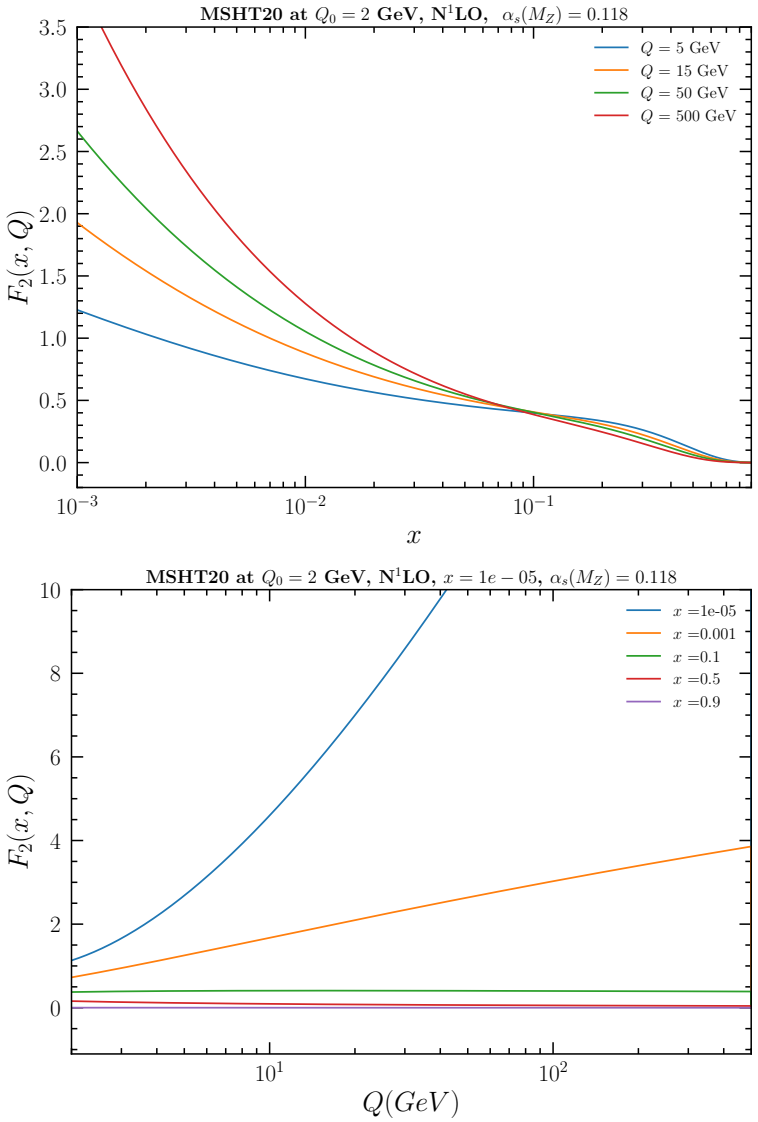

Figure 3.1: An overview of F_2 at different values of x and Q^2. Both plots are equivalent and differ only on the point of view of choosing either x or Q on the x-axis. For upcoming experiments, the center-of-mass energy (or $\sqrt{s}$, with the relation $xs = Q^2/y$, as described in Sec. 1.2.1) is planned to be around 140 GeV at the Electron-Ion Collider [120], and around 1-2 TeV at the LHeC and FCC-eh [118]. For the past HERA collider experiments, whose data feature prominently in global PDF fits, the center-of-mass energy is about 300 GeV [116].

Fig. 3.1 shows that F_2 rises with decreasing x at fixed Q. This reflects the growth of the density of partons in the incoming hadronic state when the partonic momentum fraction decreases. It also shows that F_2 is increasing with increasing momentum scale Q for x fixed and small, and (mildly) decreasing or nearly constant for x fixed and large.

3.2.2 The F_2 structure function up to NNLO

We next present the computation of the theoretical uncertainty bands for F_2 which result from variations of the resummation scale ξ, factorisation scale $\mu_{\rm F}$ and renormalisation scale $\mu_{\rm R}$. We organize the presentation of the results as follows: first we plot results versus x, by giving results first at NLO and then at NNLO of perturbation theory; next we plot results versus Q, again by giving results first at NLO and then at NNLO of perturbation theory.

Figs. 3.2 - 3.5 show the difference between the varied $F_2(\mu_{\rm R}, \mu_{\rm F}, \xi, x, Q)$ and the non-varied $F_2(x, Q)$ divided by $F_2(x, Q)$, which we note as $\Delta F_2/F_2(x, Q)$. This value will be called the relative difference of F_2.

First, the resummation scale ξ inside of F_2 is varied from 0.5 to 2 in 15 steps. Then, the relative differences of the 15 curves are calculated. After that, all variations of F_2 are bundled in one band. The boundaries of these bands are therefore not individual curves, but rather the extremes of all the values generated at each point. Because curves with different ξ can cross each other, discontinuities may be present in some plots. Fig. 3.2 shows these F_2 bands versus x, each for an evolution of Q up to a different value. In addition to ξ, other theoretical uncertainties, such as the renormalization scale $\mu_{\rm R}$ and the factorization scale $\mu_{\rm F}$, have gone through the same procedure for comparison.

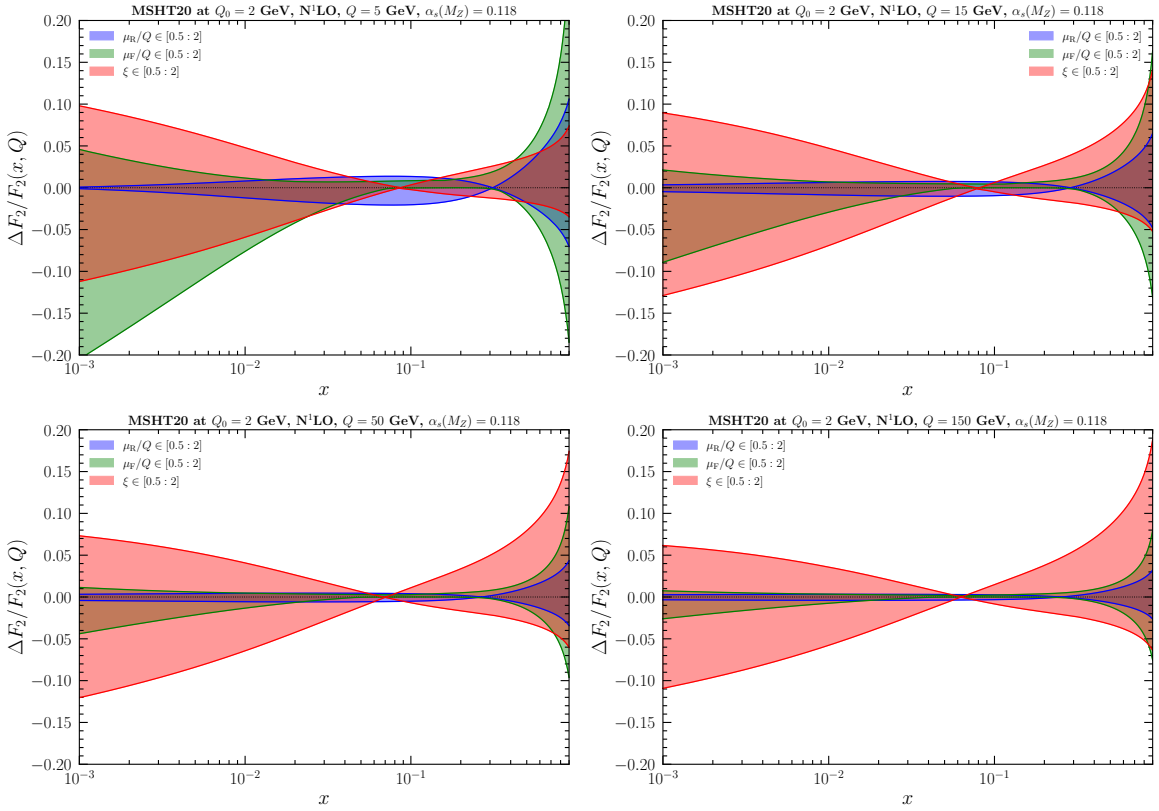

Figure 3.2: F_2 is computed at NLO for $Q \in [5, 15, 50, 150]$ GeV, respectively from top-left, top-right, bottom-left to bottom-right and the relative difference is calculated and shown on the graphs. The blue, green and red bands include the largest variation at each point with varying μ_R/Q, μ_F/Q and $\xi \in [1/2 : 2]$. The x-axis ranges from $x = 0.001$ to $x = 0.9$ (and will stay the same for the rest of the thesis).

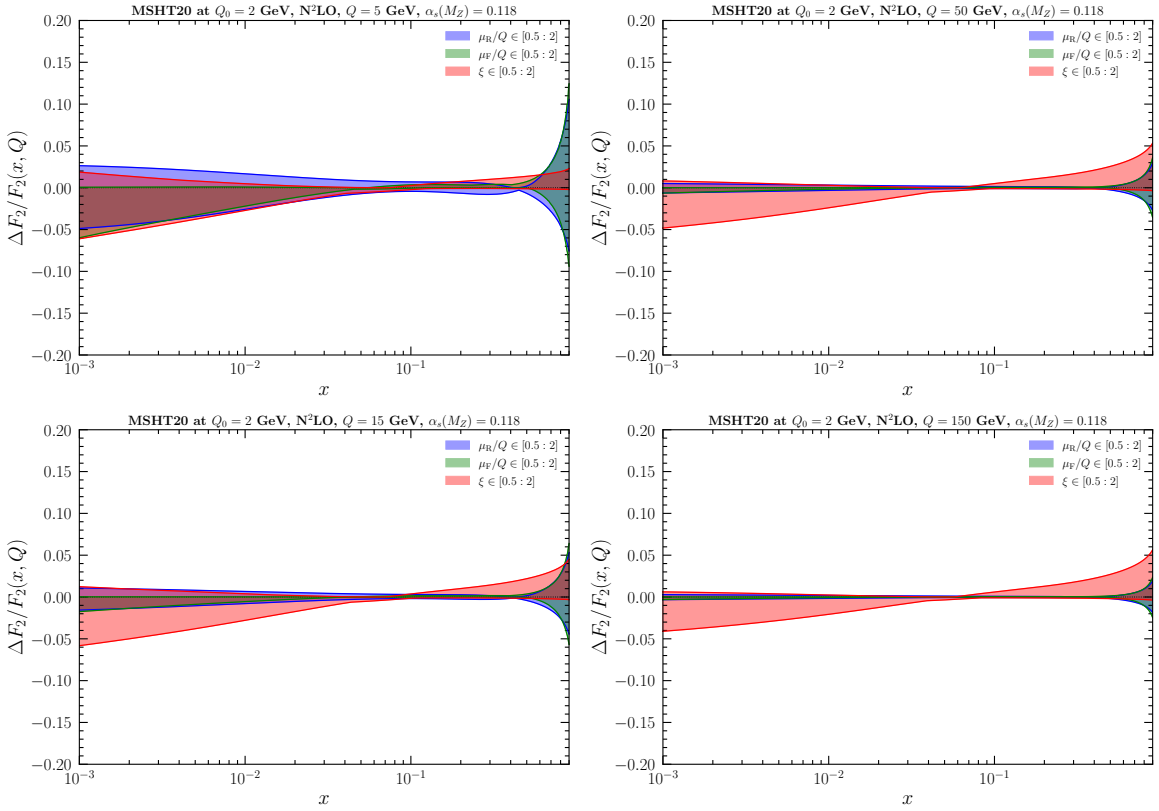

Figure 3.3: Same as Fig. 3.2, but at NNLO

We see that the RGE uncertainties on the resummation scale in F_2 are always relevant compared to the other uncertainties, and remain so at NNLO. On the other hand, μ_F and μ_R become significantly smaller across the whole x region, except in the low Q region. At around $x = 0.1$, the ξ band reaches a minimal size and expands on both sides to make a "bow tie" shape. This is the case for NLO and NNLO. The position of this minimum, where the curves cross each other, decreases in x as Q increases. This is a feature of the theory that comes with combining gamma and beta functions when calculating the structure function. Because the splitting functions are calculated by linear combinations of gamma and beta functions, a collection of roots must exist at the corresponding values of x and Q.

At high x, we see all the bands increasing rapidly. This is due to the constraint of $0 < x < 1$ and the structure functions tending to zero as x approaches 1. If $x = 1$, the process is not inelastic anymore and relies on so-called form factors instead of structure functions to describe the collision.

The next graphs represent the same results as the previous ones, but from another perspective, namely with $\Delta F_2/F_2$ plotted versus Q. Fig. 3.4 gives the NLO result, while Fig. 3.5 gives the NNLO result.

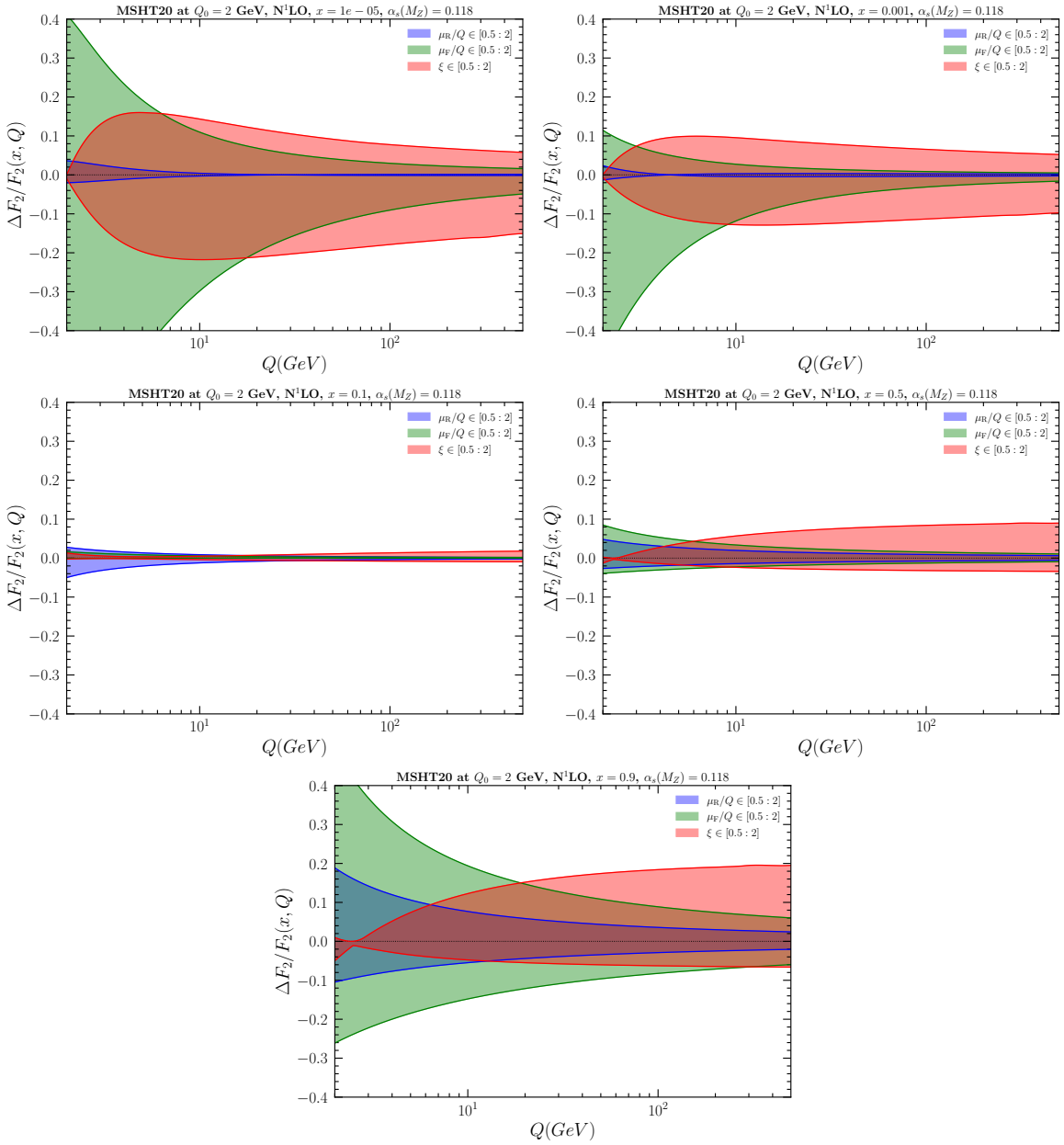

Figure 3.4: F_2 at NLO for $x \in [10^{-5}, 10^{-3}, 0.1, 0.5, 0.9]$, respectively from top-left, top-right, middle-left, middle-right to bottom. The x-axis ranges from $Q = 2$ GeV to $Q = 500$ GeV (and will stay the same for the rest of the thesis).

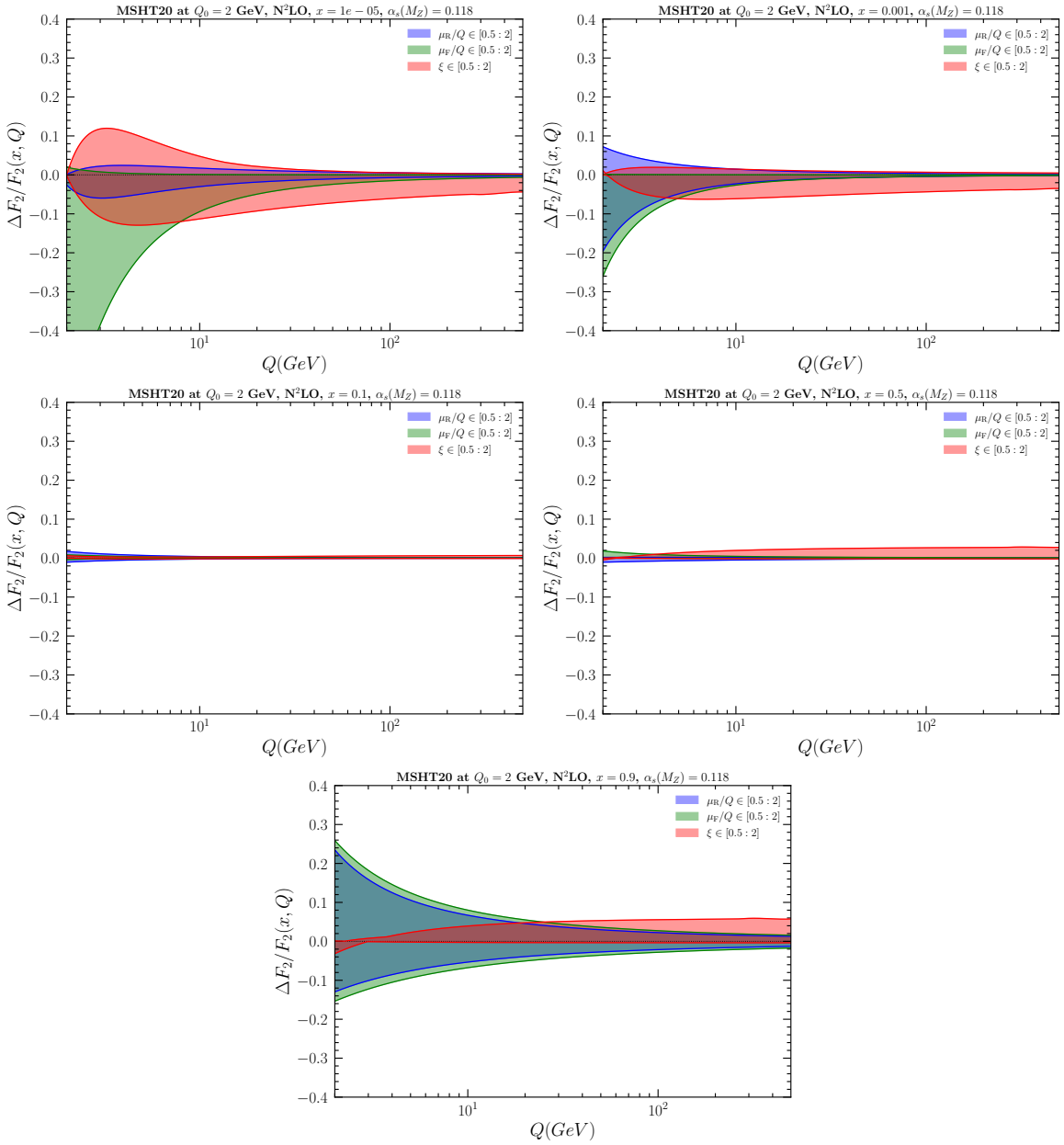

Figure 3.5: Same as Fig. 3.4, but at NNLO

We see here that the plots demonstrate a significant contribution from μ_R and μ_F only at low Q, which is consistent with the previous sets of plots. At low Q, the μ_R and μ_F bands seem sizeable, whereas the ξ band is small at Q_0 and grows to a certain value, while the other bands decrease with increasing Q. Eventually, at high Q, the RGE effects represented by the ξ bands dominate over the other uncertainty sources. We also notice how the ξ band does not grow larger over Q. This can be seen in Fig. 3.4 where the F_2 band initially grows from 0 to some value, then falls to a plateau after around 10 GeV. This constant band width over Q is due to the cumulative effect of evolving a varied F_2.

Sizeable RGE bands (larger than $\mu_{\rm F}$ and $\mu_{\rm R}$ bands) at small x reflect singularities of the splitting functions for small momentum transfers $z \to 0$ [123], and indicate the need for taking into account the singular contributions to higher orders in the RGE equations.

These contributions can be resummed through high-energy factorization [124, 134]; they are known to influence, e.g., gluon-initiated processes such as Higgs-boson production in hadron-hadron collisions at very high energies [160, 161, 162], open heavy-flavor [135, 163, 164, 165, 166, 167], quarkonia [168, 169, 170, 171, 172, 173, 174] and jet [175, 176, 177] production, forward production of jets [178, 179, 180, 181] and electroweak bosons [182, 183, 184, 185, 186, 187, 188, 189]. (Extensions to transverse momentum dependent splitting functions have also been recently studied, see [190] and references therein).

The results in Figs. 3.2-3.5 therefore indicate that the RGE systematics will significantly influence precision collider phenomenology especially at high momentum scales Q^2 and high energies s.

3.3 Longitudinal structure function F_L

The longitudinal DIS structure function F_L is defined in Eqs. (1.23),(1.26) from the DIS differential cross section. It measures the contribution to DIS from longitudinally polarized virtual photons. The contribution of longitudinal polarizations exists because the photon is off the mass shell.

At LO of perturbation theory, that is, in the parton model (i.e., $\mathcal{O}(\alpha_s^0)$), the structure function F_L vanishes (see Eq. (1.39), $F_L = 0$, that is, $F_2 = 2xF_1$, which is known as the Callan-Gross relation), due to quarks having spin 1/2.

Starting from $\mathcal{O}(\alpha_s^1)$, F_L is non-zero, and measures the density of gluons in the incoming hadronic state. This makes it especially important for phenomenological studies of PDFs.

Measurements of F_L are experimentally difficult. They require accessing contributions suppressed by coefficients of order y^2 in the DIS cross section in Eq. (1.26). So they require going to large values of y in Eq. (1.14), and varying the energy of the photon-hadron scattering. For this reason, accurate measurements of F_L could not be performed at the HERA collider. They are however planned for the future experiments at the EIC [120] and LHeC and FCC-eh [118]. The physics program revolving around F_L is very important for these future colliders.

Analogously to what we have done in the previous section for F_2, in this section we perform numerical calculations, using the code APFEL++ [158], for the DIS structure function F_L through NNLO, and estimate the size of its theoretical uncertainties by means of variations of the resummation-scale parameter ξ, the factorisation scale $\mu_{\rm F}$, and the renormalisation scale $\mu_{\rm R}$.

3.3.1 Behaviour of F_L in x and Q^2

We begin by showing F_L at different values of x and Q^2 without variations, in the same way as for F_2.

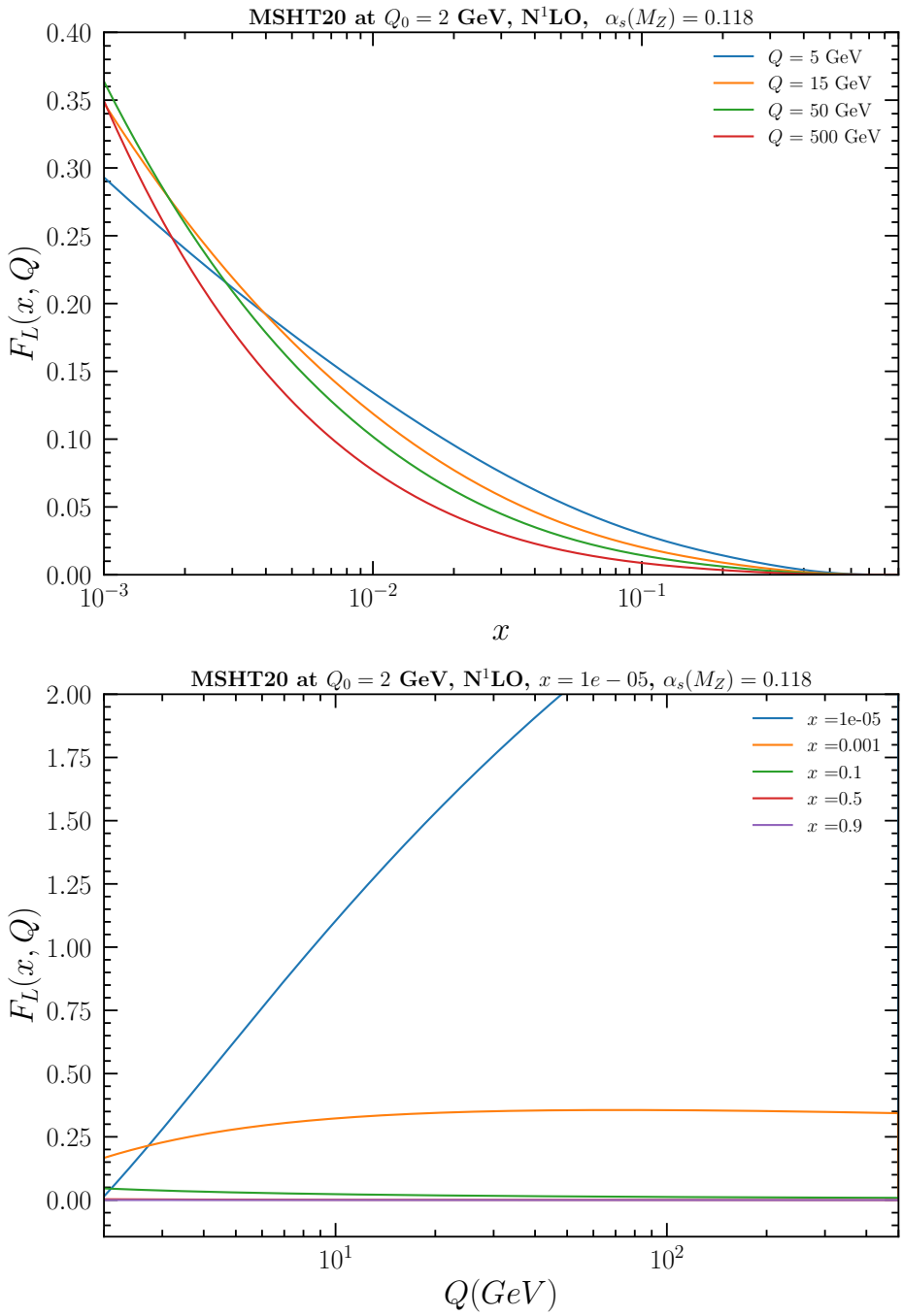

Figure 3.6: An overview of F_L at different scales

3.3.2 F_L through NNLO

Figs. 3.7, 3.8, 3.9, 3.10 show the F_L bands, versus Bjorken-x and versus Q^2, at **NLO** and **NNLO**.

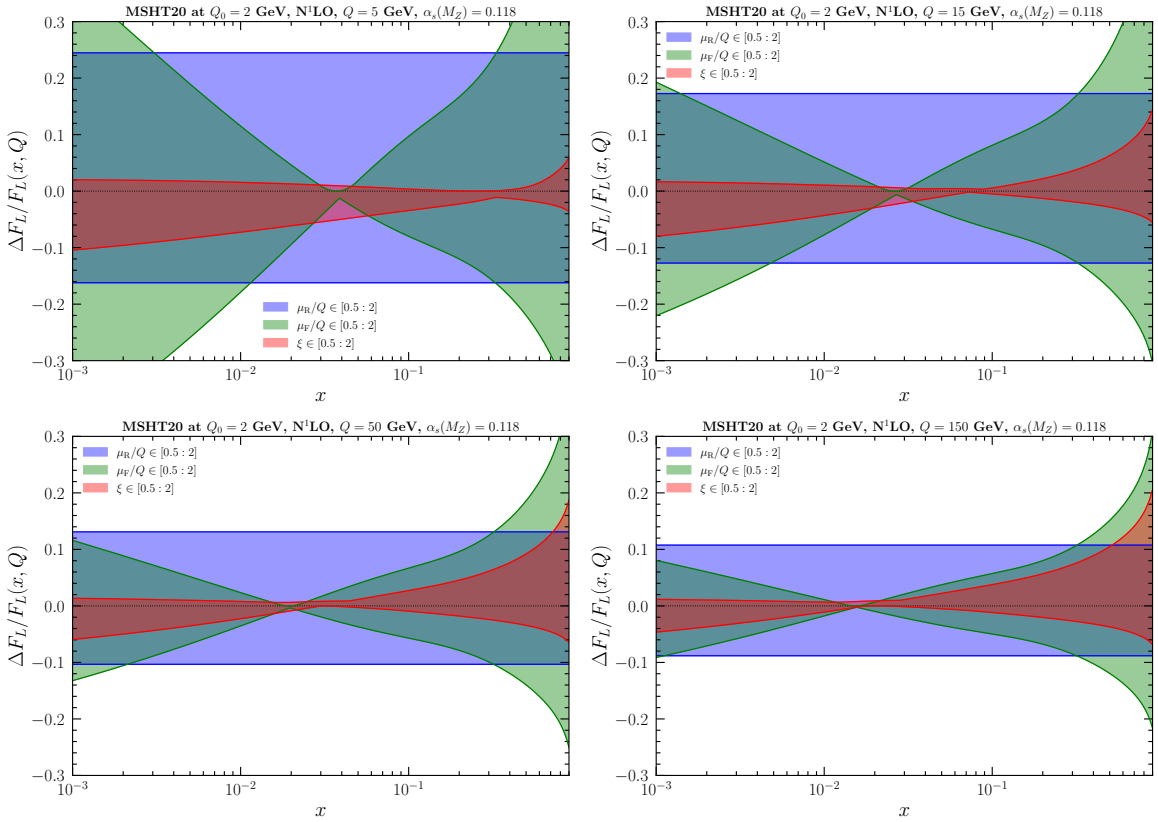

Figure 3.7: F_L is computed at NLO for $Q \in [5, 15, 50, 150]$ GeV and the relative difference is shown on the graphs. The blue, green and red bands include the largest variation at each point with varying μ_R/Q, μ_F/Q and $\xi \in [1/2 : 2]$

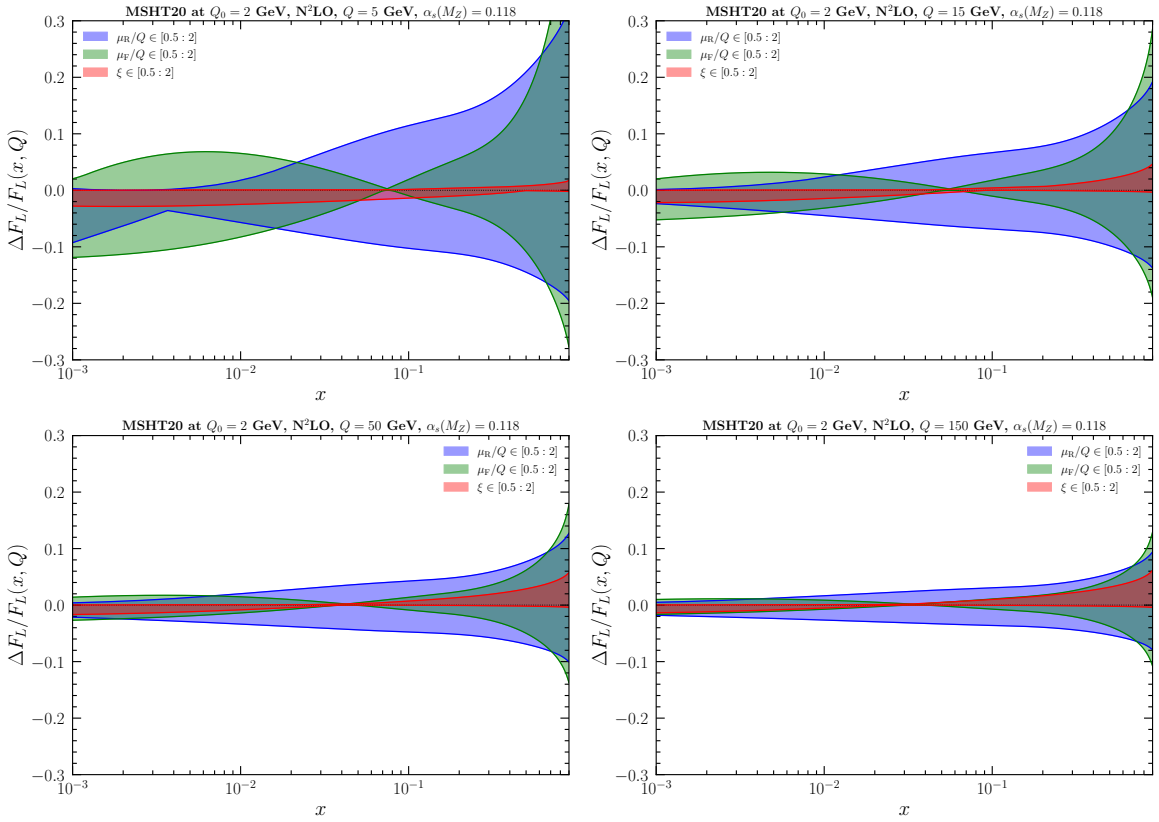

Figure 3.8: Same as Fig. 3.7, but at NNLO

We immediately notice that the μ_R band is a constant in Fig. 3.7. This is due to the fact that, since, as noted above, F_L vanishes at $\mathcal{O}(\alpha_s^0)$, the order at which we are actually calculating perturbation theory is effectively leading order (LO), not NLO. Nevertheless, the notation will remain the same as to avoid any confusion. Similarly to F_2, F_L also has a point at which the curves cross each other, whose position decreases in x as Q increases. Also similarly to F_2, the shape and growth of the ξ band are the same, i.e. it grows larger from around $x = 0.1$ to low x and high x in a "bow tie" shape. A difference from F_2, however, is that the xi band does not surpass the other bands in size.

The next graphs give equivalent plots, but plotted versus Q. Fig. 3.9 gives the NLO result, while Fig. 3.10 gives the NNLO result.

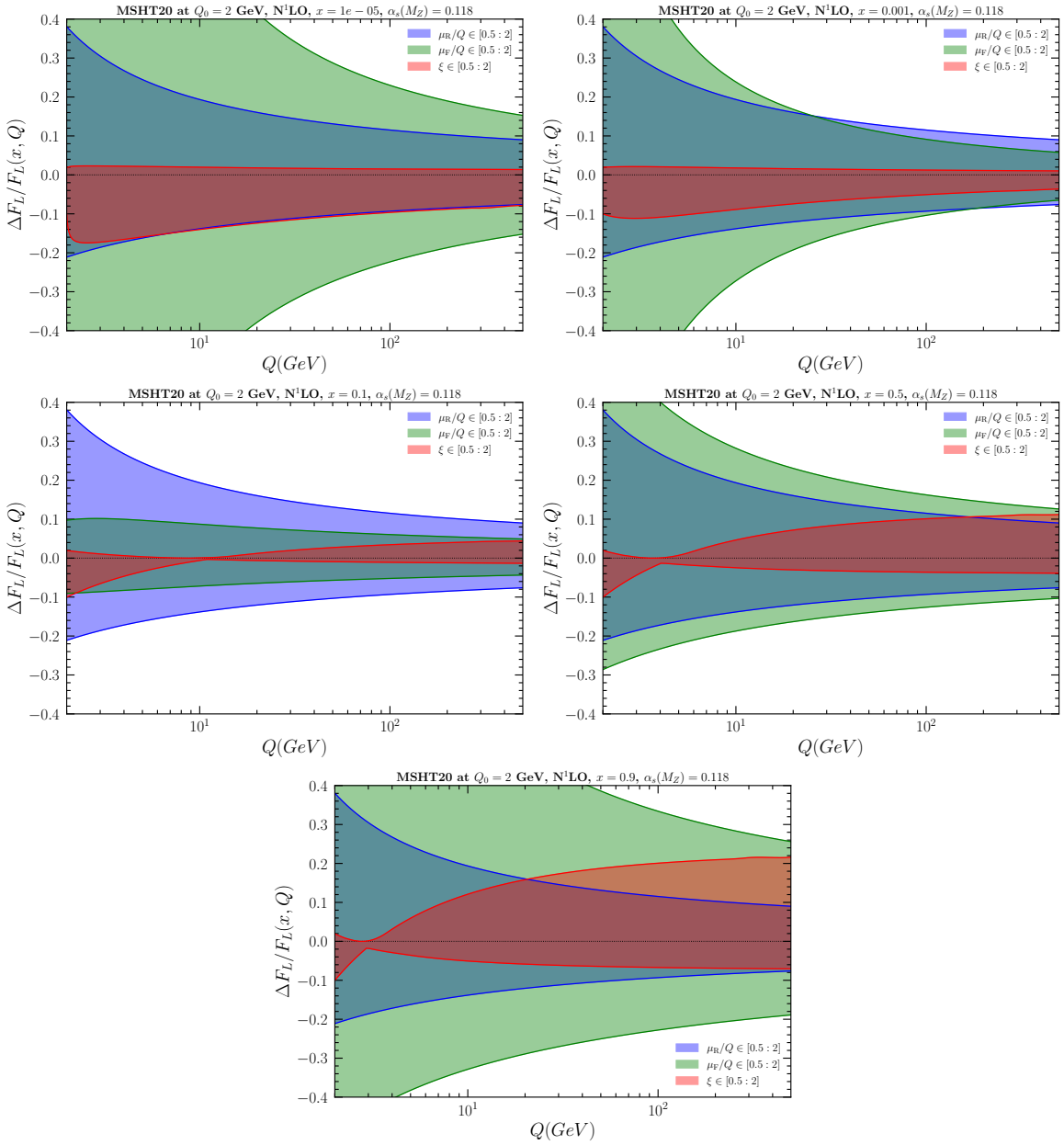

Figure 3.9: F_L at NLO at $x \in [10^{-5}, 10^{-3}, 0.1, 0.5, 0.9]$

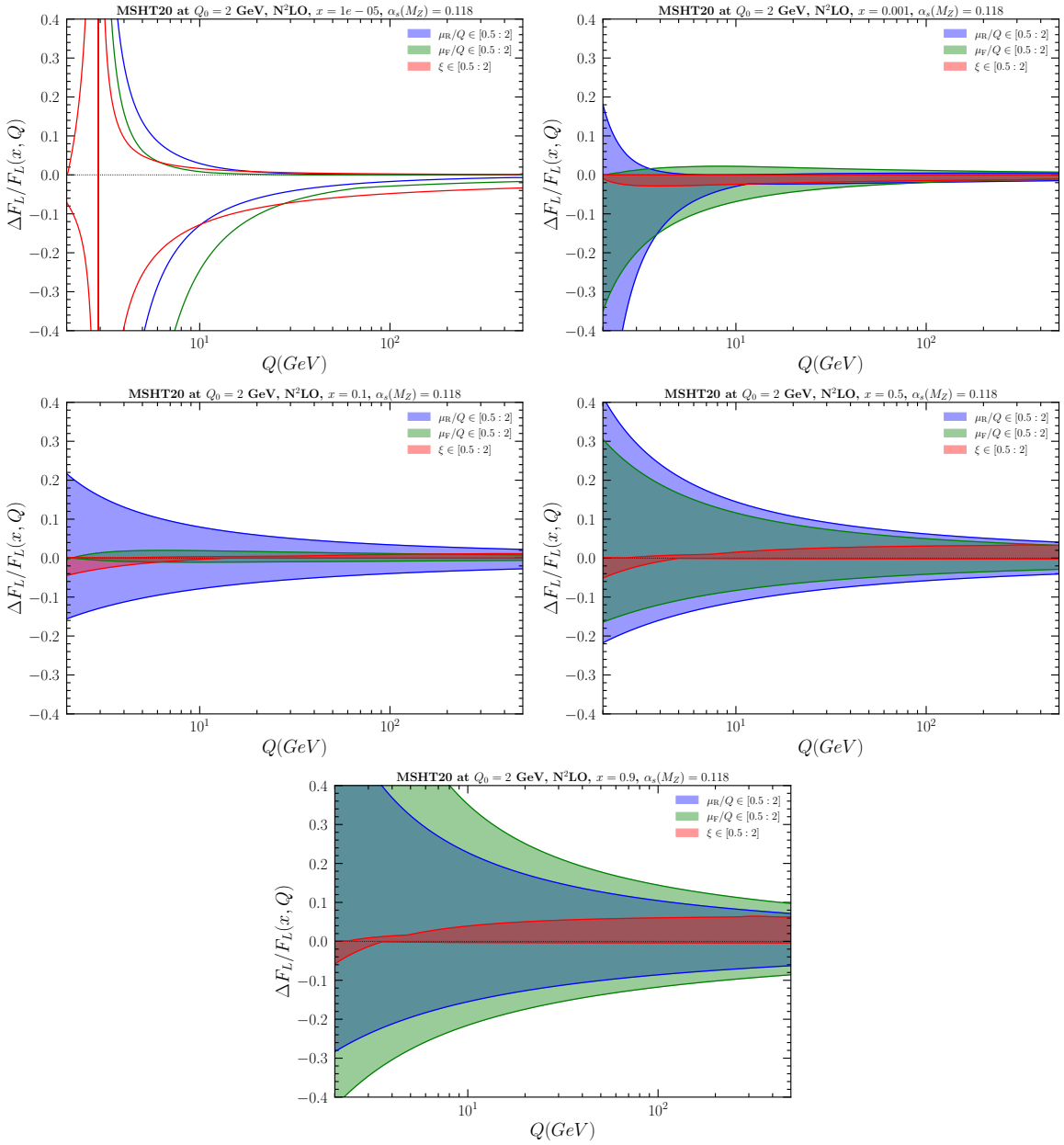

Figure 3.10: Same as Fig. 3.9, but at NNLO

We immediately notice the infinity on the top-left plot of Fig. 3.10. This means that the value of F_L somehow crossed zero and became negative. This phenomenon is connected to the gluon contribution and will be discussed in another section further on in the thesis. RGE effects are less prominent for F_L than for F_2 compared to other uncertainties. However, they should still be taken into account in high Q collider processes.

3.4 Coupling and PDF contributions to resummation scale uncertainties

The resummation scale appears in two places in the calculation of the structure function: the coupling and the PDFs. The previous calculations applied the resummation scale on both at the same time. In this section, the effect of the resummation scale ξ is studied individually on the strong coupling α_s and the PDFs. This method of comparison is meant to give some insight as to where the main contribution comes from.

Figs. 3.11-3.17 show the plots of the variation on both quantities at the same time in red, on α_s separately in green and on PDFs separately in purple.

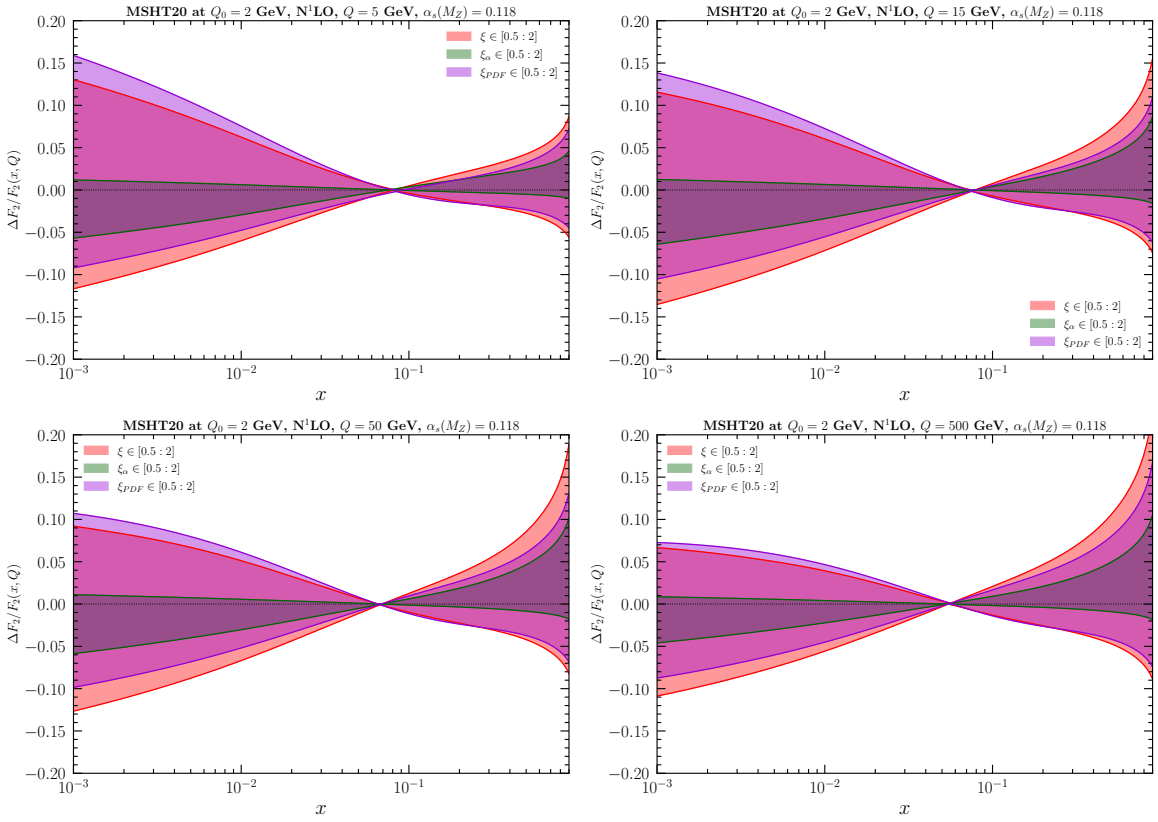

Figure 3.11: The relative difference of F_2 at **NLO** is shown for ξ applied simultaneously on α and PDFs, only on α_s and only on PDFs respectively in the red, green and purple band.

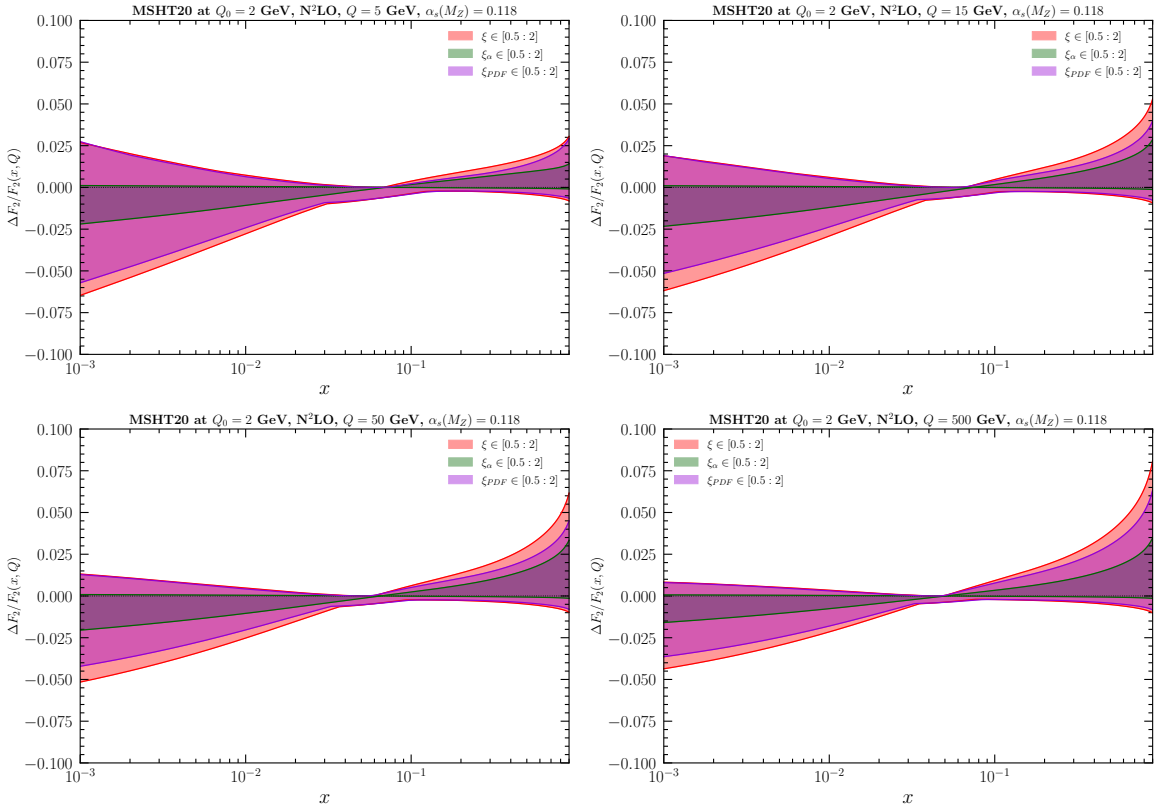

Figure 3.12: The same as in Fig. 3.11, but at **NNLO**. *The vertical scale here is different than the previous set of plots.*

At NLO and N^{2}LO, we note that the main contribution always comes from the PDF band. It also overshoots the ξ band at low x and undershoots in the other areas. We also note that the α_s band below and above $x = 0.1$ shows, respectively, an upper and lower bound very close to zero compared to the other two bands. There, the α_s contribution is near zero and the PDF band is superposed on to the ξ band.

Overall, the fact that the bands turn out to be mostly of comparable size whether they are computed for α_s and PDF together or separately provides a consistency check to the robustness of these RGE estimates.

3.5 Advancements up to N^{3}LO order

Calculations performed by several authors in the last few years [149, 150, 151, 152, 153] have made it possible to obtain splitting functions and hard scattering functions up to *approximate* N^{3}LO. This is done by taking into account Feynman diagrams up to four loops. N^{3}LO calculations are extremely difficult and long; it has taken over two decades to increase one order of the splitting functions. Furthermore, the hard-scattering functions needed to compute the structure functions, expressed in Eq. (1.41), are not fully complete. The procedure to finish everything requires transforming the splitting functions from x-space to Mellin space. The Mellin space is associated with a Mellin transform defined by Eq. (1.43). All Mellin moments of the hard-scattering functions need to be computed to get the exact N^{3}LO expression. Currently, only the first and last few have been calculated and the rest are interpolated, hence the approximate N^{3}LO. These N^{3}LO results have also been implemented in the APFEL++ [158] code. In this thesis I have then performed for the first time studies on the RGE systematics for the F_2 DIS structure function at N^{3}LO. These are reported in the next subsection. I have also performed studies at the same order in α_s for F_L, reported in the subsection following the next one.

3.5.1 F_2 at N^{3}LO order

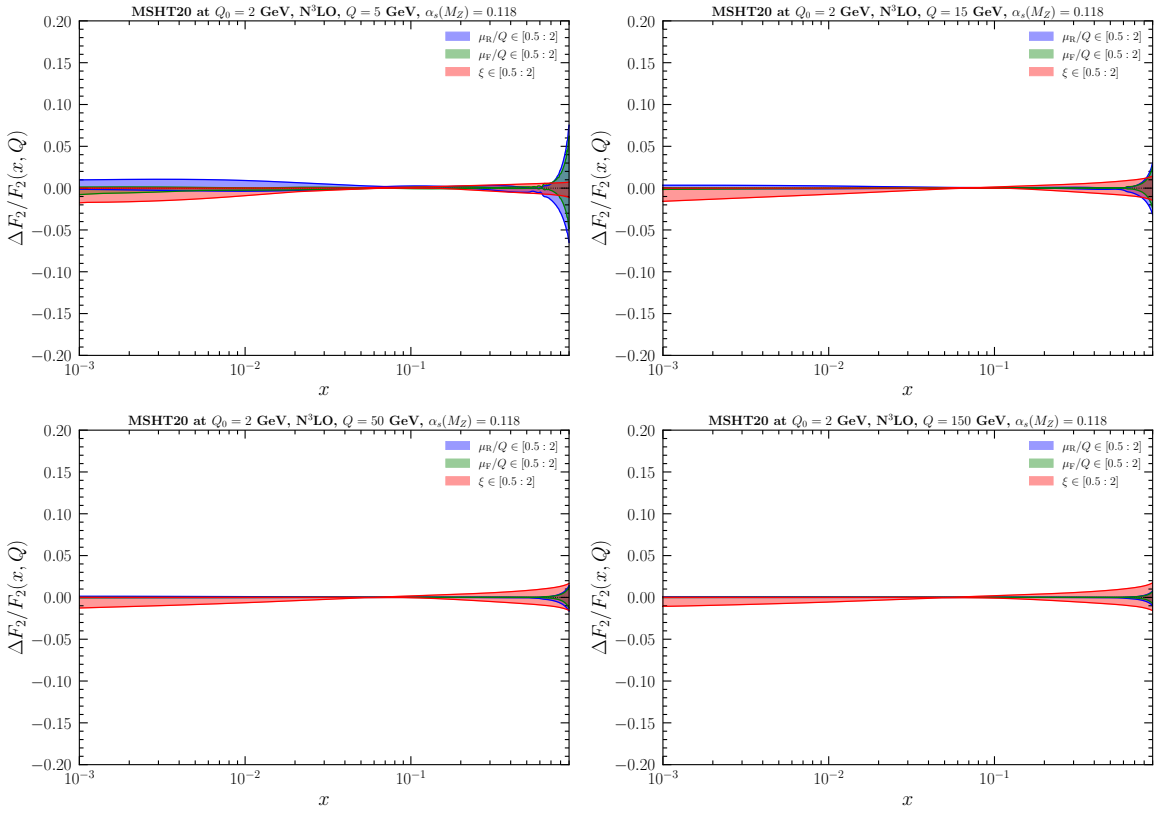

Figure 3.13: F_2 at **N^{3}LO** versus x, following the previous sets of plots in Figs. 3.2-3.3. For these analyses, the approximate N^{3}LO PDF sets from MSHT have been used.

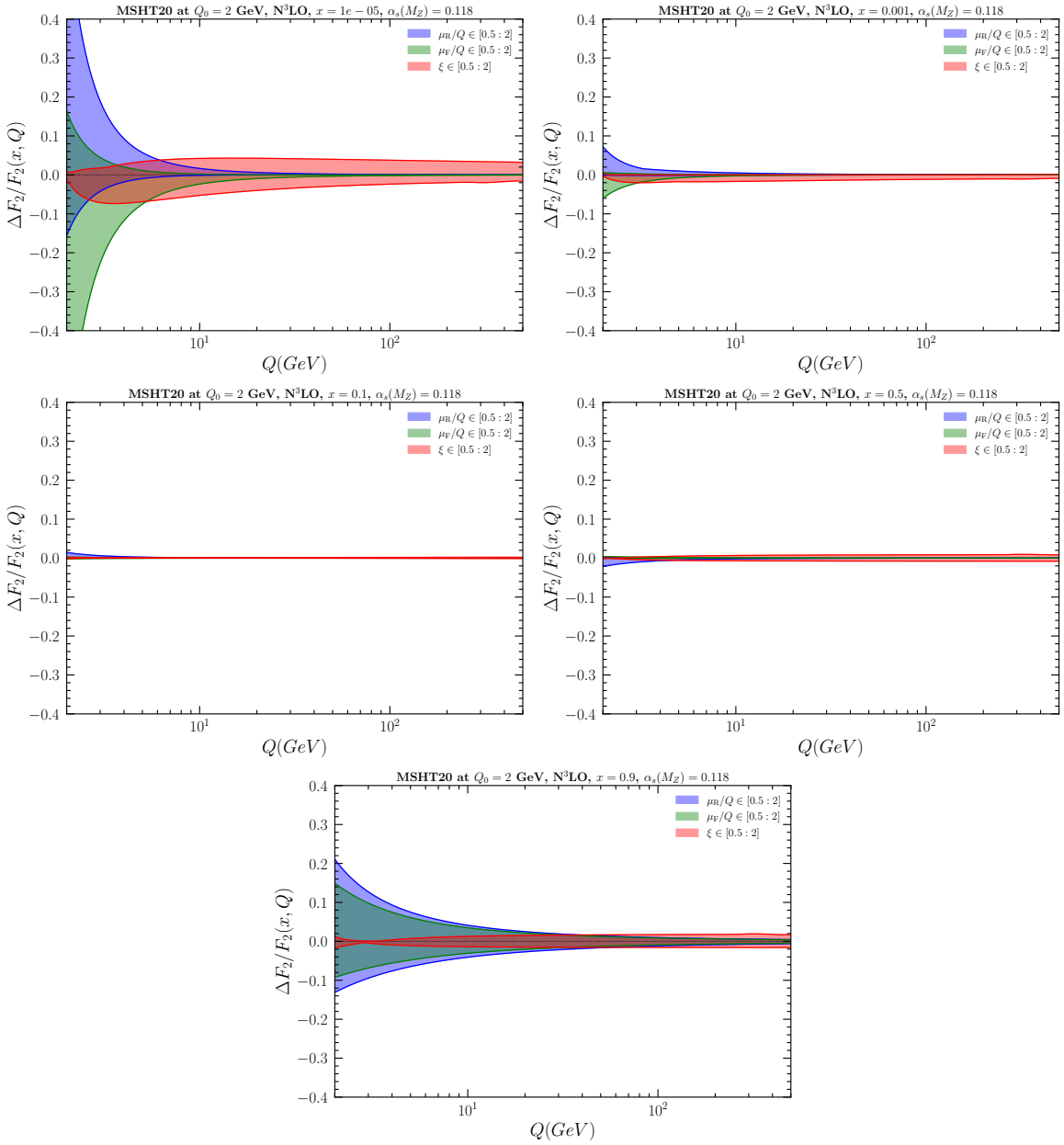

Figure 3.14: Same as Fig. 3.13, but versus Q.

Generally, all uncertainties become smaller when going to higher order. Also, following the same trend as the lower order plots, the ξ band reaches a minimum around $x = 0.1$ and increases when x goes away from that point. The behaviour over Q is also the same where it increases from around $Q = 2$ GeV and stagnates after around 10 GeV.

These results show that RGE effects continue to play a significant part in high Q precision collider phenomenology, much like the results for NLO and NNLO.

3.5.2 F_L at N^{3}LO order

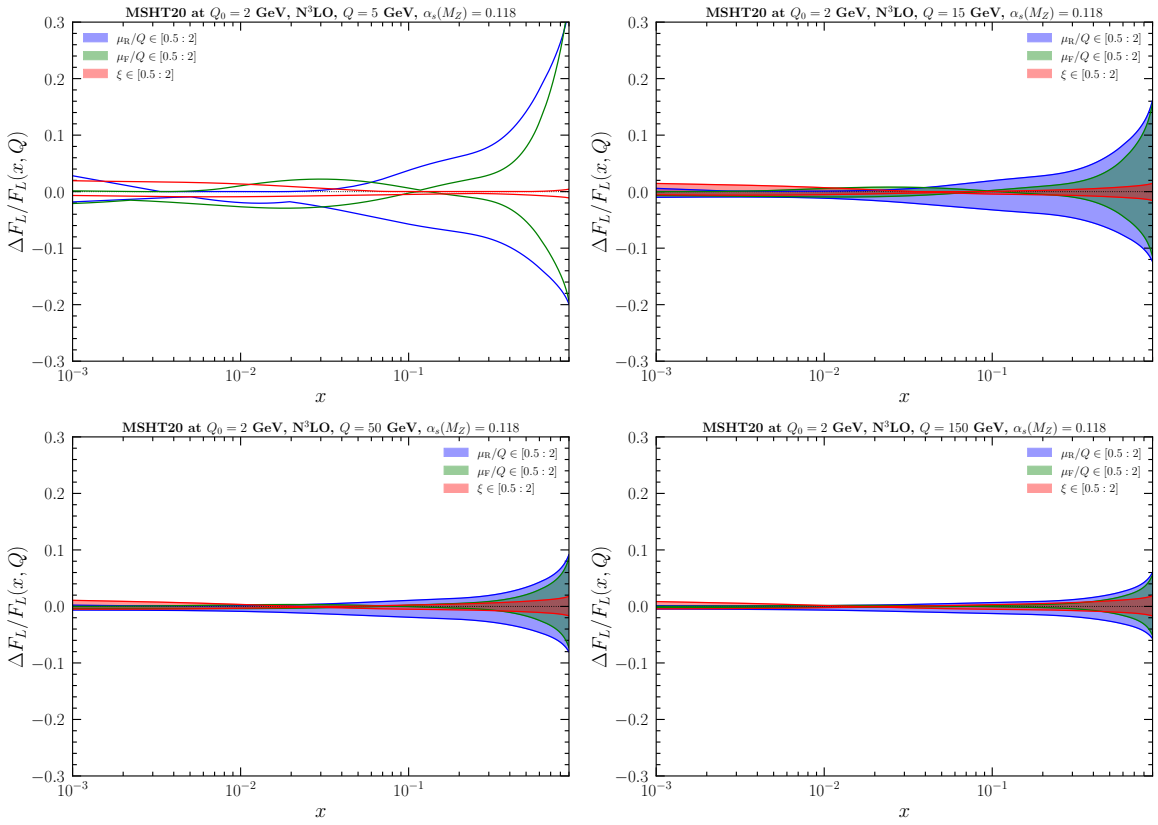

Figure 3.15: F_L at **N^{3}LO** versus x, following the previous sets of plots in Figs. 3.7-3.8.

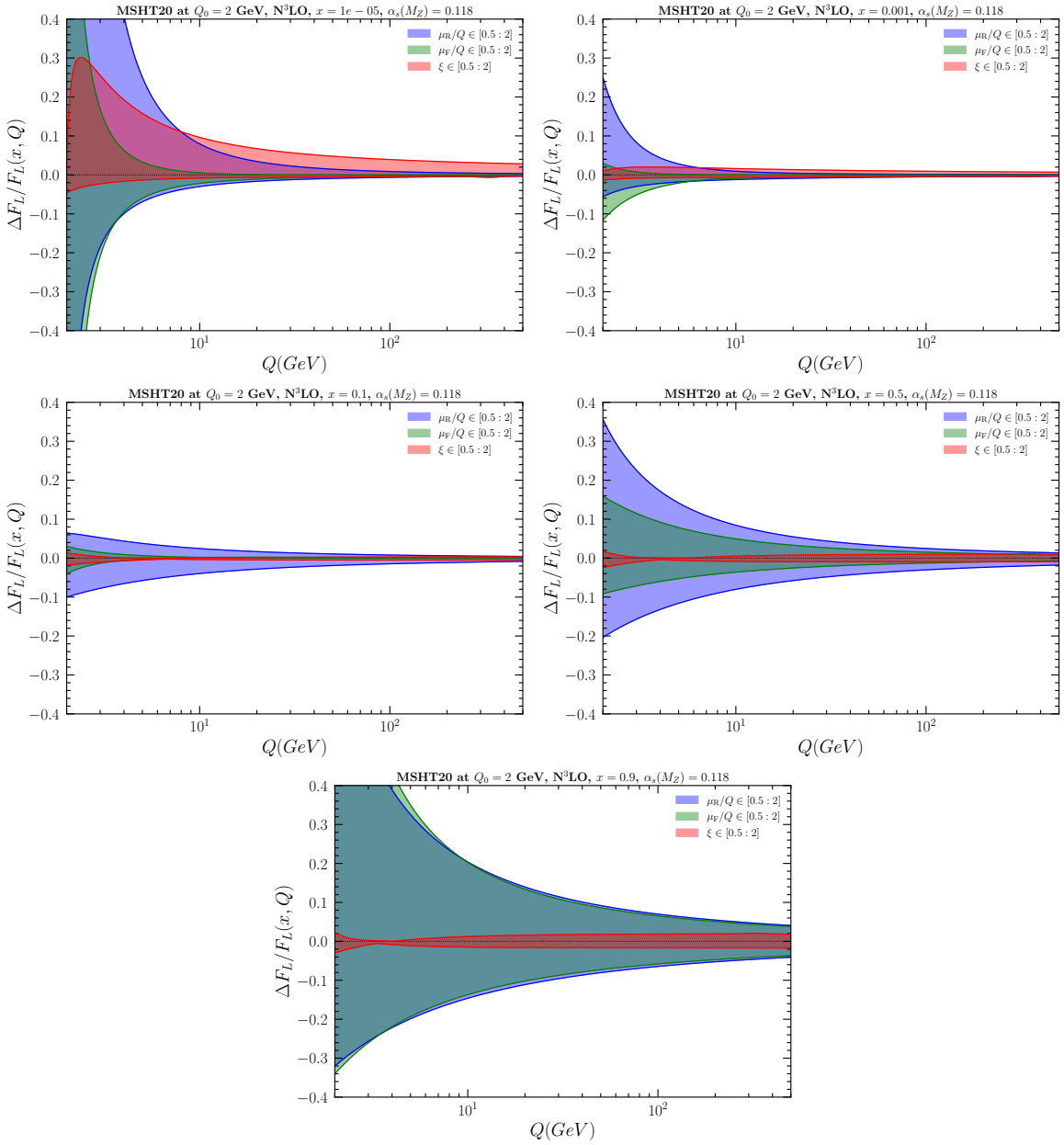

Figure 3.16: Same as Fig. 3.15, but versus Q.

For F_L, we see that the uncertainty bands have not shrunk as much as for F_2. The other chracteristics, such reaching a minimum around $x = 0.1$ and stagnating after $Q = 10$ GeV remain the same as for in NLO and NNLO. However, the ξ band seems larger than the other bands at low x, which was not the case before. In general, it can be concluded that the main characteristics of the curves are conserved through the perturbative orders, and the size does not differ much from NNLO and is of comparable size with the other bands.

3.5.3 Coupling and PDF contributions at N^{3}LO

We perform the same analysis as section 3.4 at N^{3}LO, where the alpha and PDF contributions are being considered separately.

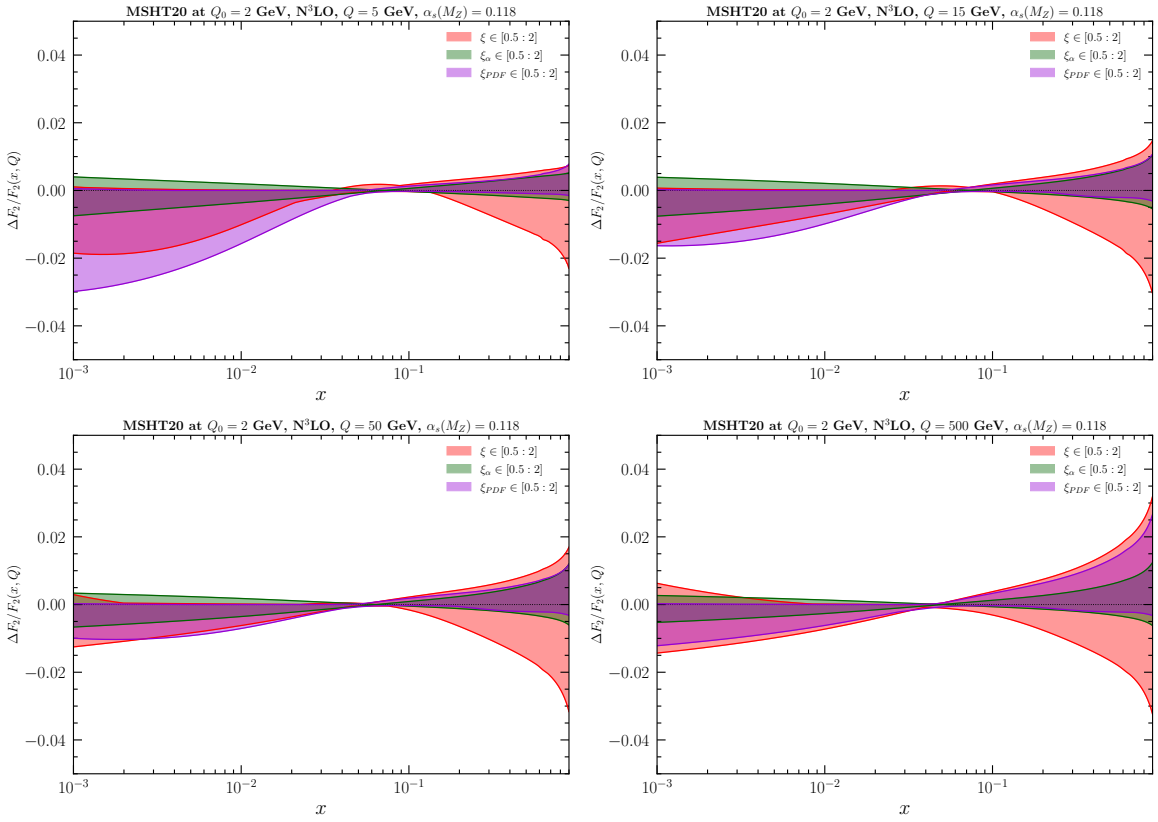

Figure 3.17: The continuation of Fig. 3.11 at **N^{3}LO** with aN^{3}LO PDFs. The red band shows the usual approach for resummation scale uncertainties for F_2; the green band shows variation from the α_s contribution; the purple band shows variation from the PDF contribution.

At low Q and low x, we see that the PDF band overshoots on the bottom side of the ξ band and that the α_s band overshoots on the top side. As Q grows (going to the next plot), the ξ band surpasses the other bands.

At high x, both the PDF and α_s bands have a sizable contribution. Both combine to make a larger ξ band.

3.6 Negative F_L and gluon PDF

In this section, the infinity in the first plot of Fig. 3.10 is investigated, which is shown again below in the first plot of Fig. 3.18. This plot shows $\Delta F_L/F_L$ at N^{2}LO for $x = 10^{-5}$. We used this definition to show the relative difference of F_L when varying different scales. Thus, an infinite value strongly suggests a zero in the denominator, so I plotted the value of the original F_L at N^{2}LO in the second plot of Fig. 3.18. F_L indeed crosses zero at small Q and

then becomes negative. We explore this behaviour further by plotting F_L over a larger range of x in the next two plots. We see that this effect occurs at small Q and small x.

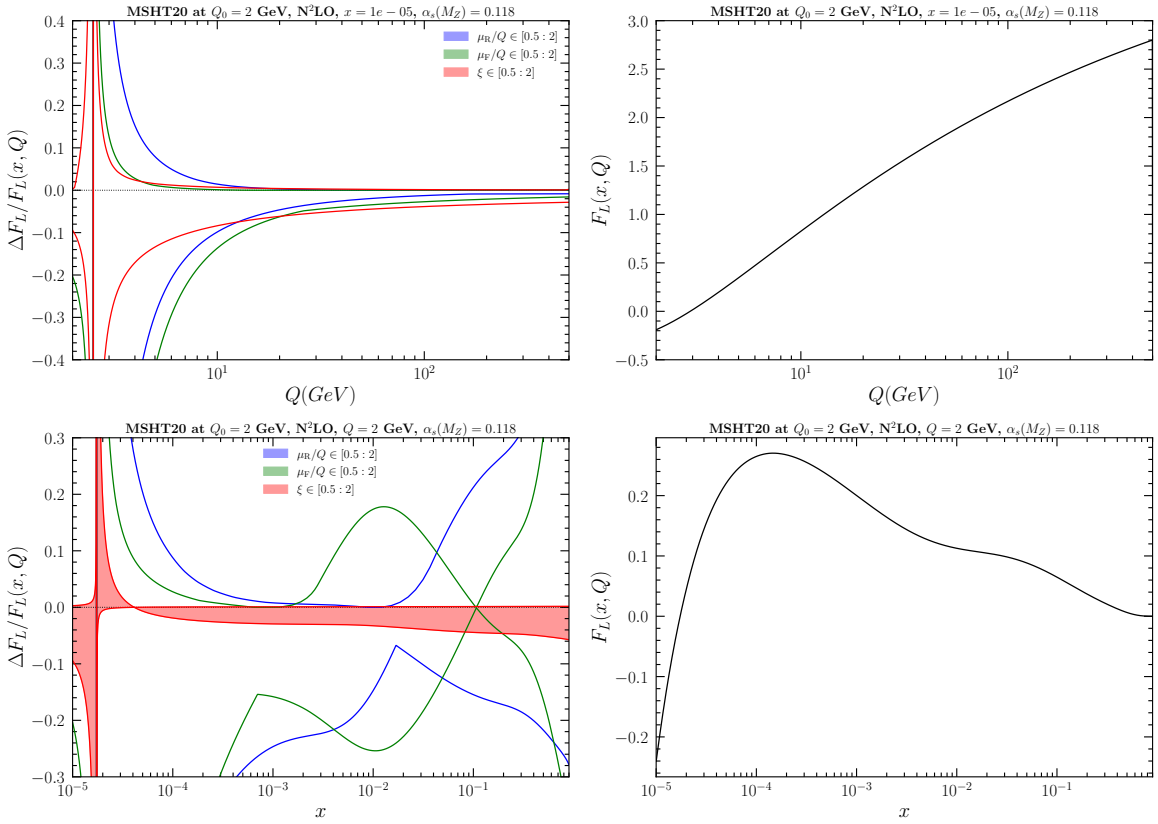

Figure 3.18: The two upper plots show the bands and original value of F_L at N^{2}LO at fixed $x = 10^{-5}$. The two bottom plots show the same, but at fixed $Q = 2$ GeV and over a larger range of x. F_L crosses zero in both plots.

For now, the reason as to why this happens is still not clear. That's why I tried using a different PDF set to see if this behaviour persists. Here, I chose *NNPDF40_an3lo_as1180* as an example. NNPDF is a collaboration that uses contemporary methods of artificial intelligence to determine PDFs of the proton. Their PDF sets are publicly available from the LHAPDF library. As can be seen, there are no more infinities or negativities anymore.

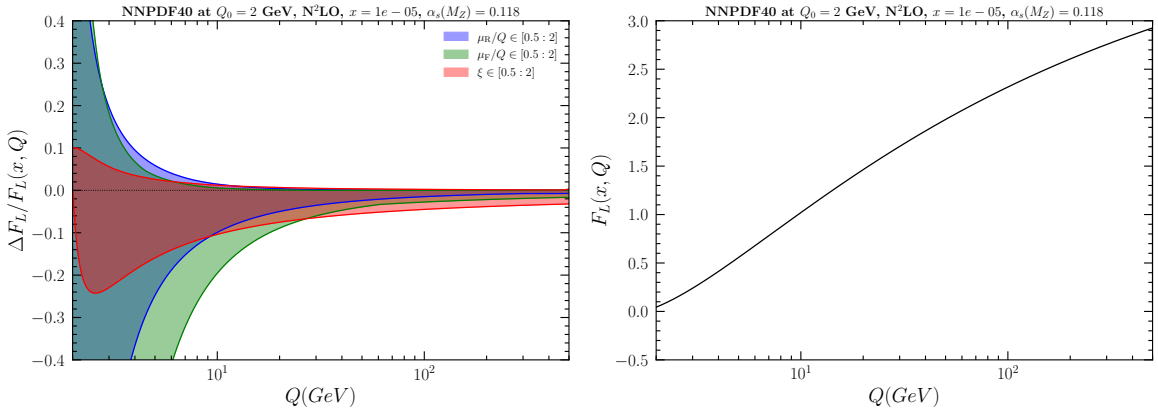

Figure 3.19: Same as Fig. 3.18, but with PDF set *NNPDF40_an3lo_as1180*. In the right plot, F_L approaches zero, but remains strictly positive. In turn, the left plot doesn't diverge anymore.

After some investigation and going through some papers, the origin of the inifinities is thought to stem from a negative gluon density at higher orders. In theory, nothing forbids the existence of such a negative gluon density, as it is a non-observable quantity that is extracted from an observable quantity such as the structure function, as seen in Eq. 1.41. However, by allowing this, the gluon density loses its probabilistic interpretation at higher orders. In the literature on global PDF fits it is discussed how a fit of the structure function without positivity constraint on the gluon pdf gives better results for an acceptable fit. While some study groups choose to impose positivity constraints on PDFs, others do not. At the moment, there is no definite answer for either approach. Recent discussions of the positivity can be found in [191, 192, 193].

In Fig. 3.20, I plotted the gluon PDFs for fixed x and fixed Q from MSHT and NNPDF and compared them. It is now clear that the gluon PDF is responsible for the negative F_L.

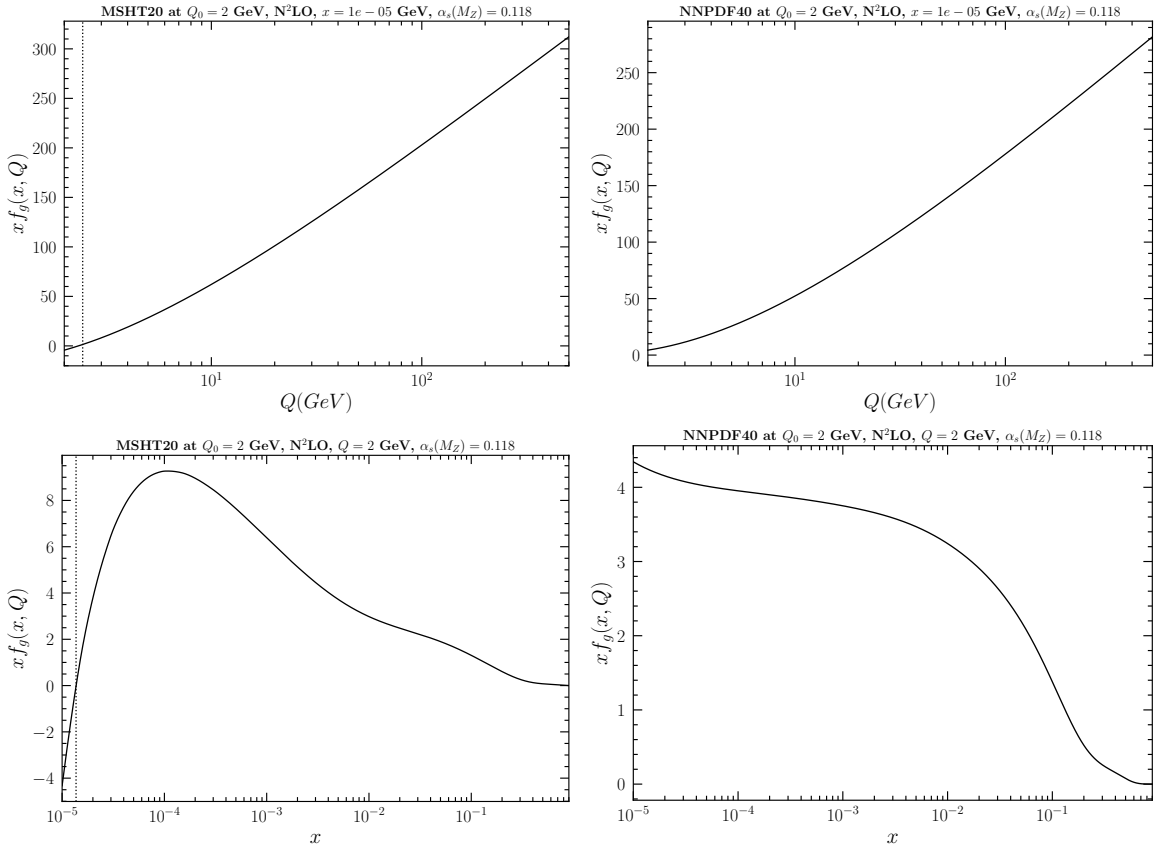

Figure 3.20: The first and second plots show the gluon PDF from, respectively, MSHT and NNPDF over Q. They are evolved from the initial value of $Q_0 = 2$ GeV. The point at which the gluon PDF from MSHT crosses zero is exactly where F_L also crosses zero, while for NNPDF the curve stays above zero. The third and fourth plots reflect the same results, but over x.

It's important to note that this phenomenon only happens for F_L and not for F_2. To explain this, we need to compare the different contributions to F_2 and F_L. For F_2 at every order, the gluon contribution is very small compared to quarks. For F_L, on the other hand, both the gluon and quarks contribution are zero at LO (see Eq. 1.39), and the gluon enters at NLO as a LO effect. This can be shown with Eqs. 1.41 and 1.49 with the expression of the coefficients given in [194].

3.7 Technical details of Apfelxx

During the process of writing the code, some technicalities were encountered. In this section, some of them are mentioned and discussed.

A first one is about tabulating PDFs at extreme values of Q and x. Because PDFs and α_s are only defined on a specific range due to numerical limitations, it is not possible to go outside this range. If one does go outside this range, then the program either crashes or gives unreliable results. There is, however, no need to extend these limits as it is deep into the non-perturbative region anyway, which is not in the confines of this thesis. The initial

parameters therefore need to be chosen accordingly, while keeping in mind that the different scales call on PDFs and α_s at a factor under and above the chosen energies. If one wants to compute a structure function at $Q = 0.9$ GeV, if $\mu_F = 0.5 * Q$ (or $\xi = 0.5$), one would be calling PDFs down at $0.9 * 0.5$ GeV, which is outside the tabulation region. Or, for $Q > 500$ GeV, if $\mu_F = 2 * Q$, the program also crashes. In practice, I set the parameter for $Q_{min} = 1.9$ GeV and $Q_{max} = 500$ GeV.

A second one is about the number of flavours (n_f) taken into consideration, e.g. in the beta functions of Eq. 2.69. It's possible to dynamically change n_f while doing the calculations by setting a set of threshold, being the quark masses. After the energy reaches a threshold, a subsequent extra quark will be taken into consideration. When changing n_f, a discrete jump occurs, as shown below in Fig. 3.21. Because n_f is not a variable we are investigating, it has

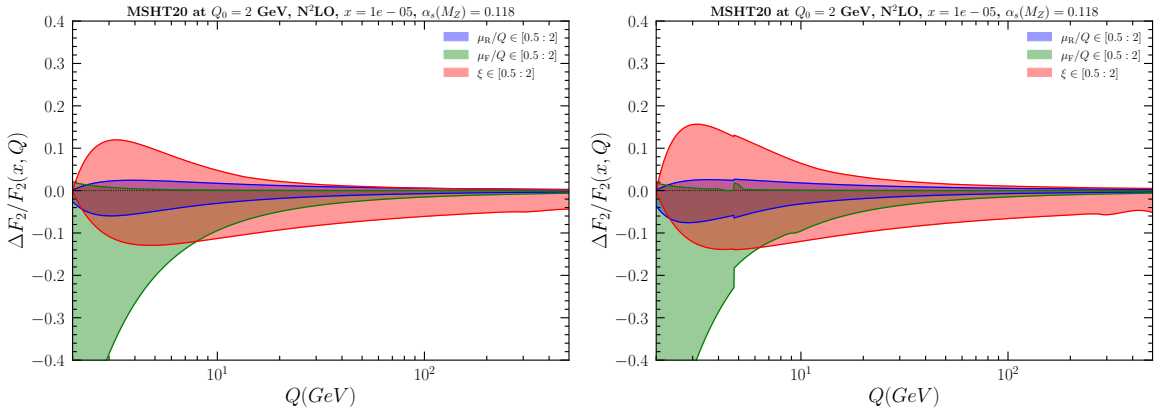

Figure 3.21: On the left is a plot with a constant $n_f = 5$, whereas on the right is the same plot where n_f changes from 4 to 5 at the energy of the bottom quark mass ($m_b = 4.75$ GeV). The sudden jump can be clearly seen at that energy.

been chosen as a constant at $n_f = 5$ for all plots for the sake of a smooth band.

A third one is about kinks, or non-smoothness, of the F_2 and F_L bands. As mentioned previously, bands contain all values across all variations. If one curve is at the limit of the band and gets crossed by another one, then this will be visible as a kink in the band. Fig. 3.22 shows the individual curves of a band forming such a kink.

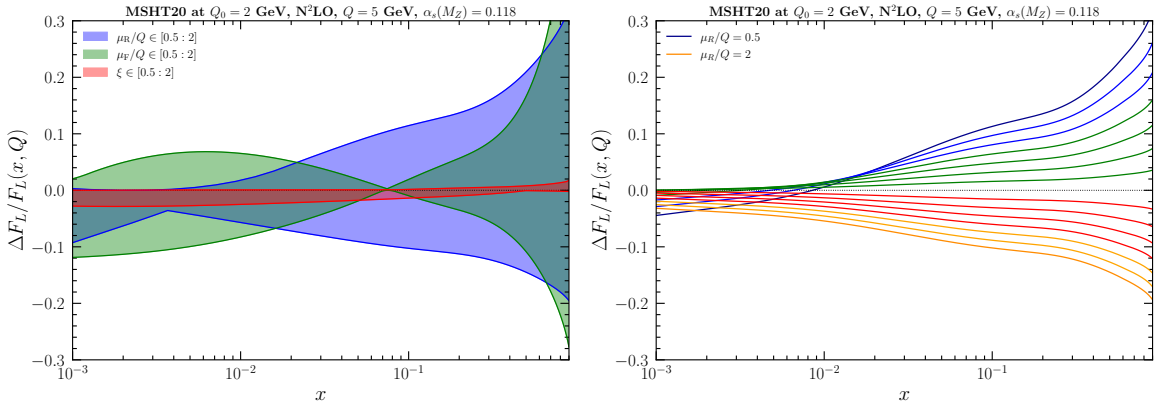

Figure 3.22: On the left is an example of a kink in the blue band. On the right are the individual curves that form the blue band. The darkblue curve at low x gets crossed by the orange curve and form a kink together in the band.

3.8 Summary and conclusion

In this chapter we have applied the methods for studying the perturbative RGE systematics, described in Chapter 2, to the case of DIS structure functions F_2 and F_L.

We have obtained numerical results for the RGE systematic uncertainties, working at different orders of perturbation theory, throughout the kinematic range in x and Q^2 relevant for the present measurements and for the planned future experiments. We have presented, on one hand, results at NLO and NNLO, finding that they agree with existing results in the literature, and, on the other hand, results at N^{3}LO, which are new, and have been achieved by employing the implementation in the APFEL++ [158] code of the recent four-loop perturbative results [149, 150, 151, 152, 153].

We have compared this source of systematics, parameterized by the resummation scale ξ, with the standard perturbative scale uncertainties controlled by the factorization and renormalization scales μ_F and μ_R. We find that resummation-scale effects are generally sizeable and should be taken into account in precision phenomenology. They have distinctive behaviours compared to μ_F and μ_R effects: while the latter dominate at low Q^2, the former dominate at high Q^2, and are especially important in the region of small Bjorken-x. For sufficiently large Q^2, they become dominant also at large Bjorken-x. The results which we have presented for F_2 are relevant for existing DIS measurements and current PDF analyses. The results which we have presented for the longitudinal structure function F_L are mostly relevant for future collider experiments such as the EIC, LHeC and FCC-eh.

Conclusion

The Standard Model (SM) is by far the most accurate and precise theory about the fundamentals of our world. Yet, many parts of the SM are still unexplored. Moreover, the SM leaves several questions unanswered, for which physics beyond the Standard Model (BSM) is needed. Future collider experiments, such as the HL-LHC, EIC and FCC, are planned to break through the current limits and push the theory to new boundaries. With this, during the next few decades it is hoped that many mysteries will be solved. A crucial factor to achieve this is the progress in the accuracy of our theoretical predictions.

This thesis has focused on a methodology to evaluate the theoretical systematic uncertainties associated with the use of QCD renormalization group evolution equations (RGEs) in theoretical predictions for collider processes. This methodology is based on the technique of introducing "resummation scales" in the solution of RGEs, and estimating theoretical RGE uncertainties in physical observables from the variation of such resummation scales. These effects can then be compared with those obtained from the variation of factorization and renormalization scales in QCD perturbation theory.

In the first part of the thesis, a short, compact overview of QCD and DIS in chapter 1 and the theory of RGE in chapter 2 has been given. Here, renormalization is introduced, and it is shown how it leads to RGEs, with intrinsic theoretical uncertainties. Both analytic and numerical solutions of RGEs are examined. In either case, resummation scales are defined, denoted by $\kappa\mu$ and $\xi\mu$ respectively, and their equivalence is studied.

The RGE uncertainties are present in the evolution of the strong coupling (α_s) and parton distribution functions (PDFs), through the Dokshitzer-Gribov-Lipatov-Altarelli-Parisi equations, and propagate through to the deep-inelastic scattering structure functions (F_2, F_L, F_T) of the proton. In the second part of the thesis, the above methodology for RGE systematics is applied to structure functions, using the code of APFEL++, and plots of F_2 and F_L are shown for a wide range of scales in Chapter 3. The obtained bands are generally of the same magnitude as the other well known theoretical uncertainties (the renormalization and factorization scales).

In Figs. 3.2 - 3.4, it can be consistently seen that **for F_2 the ξ band becomes the main contributor at low x and high x, and high Q**. The large size at low and high x is due to singularities in the splitting functions, while the large size at high Q is due to a cumulative effect. The high Q region is of high importance because future collider experiments will be able to access this high Q region for the first time. According to the plots, this region is where this new uncertainty will become more relevant. In Figs. 3.7-3.10, for F_L, the ξ band is relevant only at very high Q and high x.

I have hereby also shown plots of RGE uncertainties at N^{3}LO in Figs. 3.13 - 3.16. The previous analyses for F_2 and F_L stay true. We see that the bands are much smaller than

before because of going to a higher order, and we also notice that the contribution of ξ at low and high x and high Q is still the highest.

Bibliography

[1] Yuri L. Dokshitzer, Dmitri Diakonov and S. I. Troian. "Hard Processes in Quantum Chromodynamics". In: *Phys. Rept.* 58 (1980), pp. 269–395. DOI: 10.1016/0370-1573(80)90043-5.

[2] Alfred H. Mueller. "Perturbative QCD at High-Energies". In: *Phys. Rept.* 73 (1981), p. 237. DOI: 10.1016/0370-1573(81)90030-2.

[3] Guido Altarelli. "Partons in Quantum Chromodynamics". In: *Phys. Rept.* 81 (1982), p. 1. DOI: 10.1016/0370-1573(82)90127-2.

[4] A. Bassetto, M. Ciafaloni and G. Marchesini. "Jet Structure and Infrared Sensitive Quantities in Perturbative QCD". In: *Phys. Rept.* 100 (1983), pp. 201–272. DOI: 10.1016/0370-1573(83)90083-2.

[5] Yuri L. Dokshitzer et al. *Basics of perturbative QCD*. 1991.

[6] R. Keith Ellis, W. James Stirling and B. R. Webber. *QCD and collider physics*. Vol. 8. Cambridge University Press, Feb. 2011. ISBN: 978-0-511-82328-2, 978-0-521-54589-1. DOI: 10.1017/CBO9780511628788.

[7] Michael H. Seymour. "Quantum chromodynamics". In: *2004 European School of High-Energy Physics*. May 2005, pp. 49–94. arXiv: hep-ph/0505192.

[8] George F. Sterman. "QCD and jets". In: *Theoretical Advanced Study Institute in Elementary Particle Physics: Physics in D ≧ 4*. Dec. 2004, pp. 67–145. arXiv: hep-ph/0412013.

[9] George F. Sterman. "Quantum chromodynamics". In: (Dec. 2005). arXiv: hep-ph/0512344.

[10] George F. Sterman. "Some Basic Concepts of Perturbative QCD". In: *Acta Phys. Polon. B* 39 (2008). Ed. by R. Fiore, A. Papa and C. Royon, pp. 2151–2172. arXiv: 0807.5118 [hep-ph].

[11] George Sterman. "QCD at Short Distances: Jets and Factorization". In: *Acta Phys. Polon. B* 45.12 (2014). Ed. by Michal Praszalowicz, pp. 2205–2240. DOI: 10.5506/APhysPolB.45.2205. arXiv: 1412.5698 [hep-ph].

[12] John Collins. *Foundations of Perturbative QCD*. Vol. 32. Cambridge Monographs on Particle Physics, Nuclear Physics and Cosmology. Cambridge University Press, July 2023. ISBN: 978-1-00-940184-5, 978-1-00-940183-8, 978-1-00-940182-1. DOI: 10.1017/9781009401845.

[13] Wikipedia contributors. *Standard Model — Wikipedia, The Free Encyclopedia*. [Online; accessed 10-October-2024]. 2024. URL: https://en.wikipedia.org/w/index.php?title=Standard_Model&oldid=1248676010.

[14] V. N. Gribov and L. N. Lipatov. "Deep inelastic e p scattering in perturbation theory". In: *Sov. J. Nucl. Phys.* 15 (1972), pp. 438–450.

[15] Guido Altarelli and G. Parisi. "Asymptotic Freedom in Parton Language". In: *Nucl. Phys. B* 126 (1977), pp. 298–318. DOI: 10.1016/0550-3213(77)90384-4.

[16] Yuri L. Dokshitzer. "Calculation of the Structure Functions for Deep Inelastic Scattering and e+ e- Annihilation by Perturbation Theory in Quantum Chromodynamics." In: *Sov. Phys. JETP* 46 (1977), pp. 641–653.

[17] P. Achard et al. "Measurement of the running of the electromagnetic coupling at large momentum-transfer at LEP". In: *Physics Letters B* 623.1 (2005), pp. 26–36. ISSN: 0370-2693. DOI: https://doi.org/10.1016/j.physletb.2005.07.052. URL: https://www.sciencedirect.com/science/article/pii/S0370269305010439.

[18] V. Bertone, G. Bozzi and F. Hautmann. "Perturbative hysteresis and emergent resummation scales". In: *Phys. Rev. D* 105.9 (2022), p. 096003. DOI: 10.1103/PhysRevD.105.096003. arXiv: 2202.03380 [hep-ph].

[19] S Catani. "The resummation of soft gluons in hadronic collisions". In: *Nuclear Physics B* 478.1–2 (Oct. 1996), pp. 273–310. ISSN: 0550-3213. DOI: 10.1016/0550-3213(96)00399-9. URL: http://dx.doi.org/10.1016/0550-3213(96)00399-9.

[20] Stefano Catani et al. "Soft-gluon resummation for Higgs boson production at hadron colliders". In: *Journal of High Energy Physics* 2003.07 (July 2003), pp. 028–028. ISSN: 1029-8479. DOI: 10.1088/1126-6708/2003/07/028. URL: http://dx.doi.org/10.1088/1126-6708/2003/07/028.

[21] Giuseppe Bozzi et al. "Transverse-momentum resummation and the spectrum of the Higgs boson at the LHC". In: *Nuclear Physics B* 737.1–2 (Mar. 2006), pp. 73–120. ISSN: 0550-3213. DOI: 10.1016/j.nuclphysb.2005.12.022. URL: http://dx.doi.org/10.1016/j.nuclphysb.2005.12.022.

[22] Valerio Bertone, Giuseppe Bozzi and Francesco Hautmann. "Perturbative RGE systematics in precision observables". In: *Phys. Rev. D* 111.7 (2025), p. 074005. DOI: 10.1103/PhysRevD.111.074005. arXiv: 2407.20842 [hep-ph].

[23] P. A. Baikov, K. G. Chetyrkin and J. H. Kühn. "Five-Loop Running of the QCD Coupling Constant". In: *Physical Review Letters* 118.8 (Feb. 2017). ISSN: 1079-7114. DOI: 10.1103/physrevlett.118.082002. URL: http://dx.doi.org/10.1103/PhysRevLett.118.082002.

[24] F. Herzog et al. "The five-loop beta function of Yang-Mills theory with fermions". In: *Journal of High Energy Physics* 2017.2 (Feb. 2017). ISSN: 1029-8479. DOI: 10.1007/jhep02(2017)090. URL: http://dx.doi.org/10.1007/JHEP02(2017)090.

[25] R. Angeles-Martinez et al. "Transverse Momentum Dependent (TMD) parton distribution functions: status and prospects". In: *Acta Phys. Polon. B* 46.12 (2015), pp. 2501–2534. DOI: 10.5506/APhysPolB.46.2501. arXiv: 1507.05267 [hep-ph].

[26] John C. Collins and Davison E. Soper. "Parton Distribution and Decay Functions". In: *Nucl. Phys. B* 194 (1982), pp. 445–492. DOI: 10.1016/0550-3213(82)90021-9.

[27] John C. Collins and Davison E. Soper. "Back-To-Back Jets: Fourier Transform from B to K-Transverse". In: *Nucl. Phys.* B197 (1982), pp. 446–476. DOI: 10.1016/0550-3213(82)90453-9.

[28] John C. Collins and Davison E. Soper. "Back-To-Back Jets in QCD". In: *Nucl. Phys.* B193 (1981). [Erratum: Nucl. Phys.B213,545(1983)], p. 381. DOI: 10.1016/0550-3213(81)90339-4.

[29] John C. Collins, Davison E. Soper and George F. Sterman. "Factorization of Hard Processes in QCD". In: *Adv. Ser. Direct. High Energy Phys.* 5 (1989), pp. 1–91. DOI: 10.1142/9789814503266_0001. arXiv: hep-ph/0409313.

[30] F. Hautmann and Davison E. Soper. "Parton distribution function for quarks in an s-channel approach". In: *Phys. Rev. D* 75 (2007), p. 074020. DOI: 10.1103/PhysRevD.75.074020. arXiv: hep-ph/0702077.

[31] John C. Collins. "What exactly is a parton density?" In: *Acta Phys. Polon. B* 34 (2003), p. 3103. arXiv: hep-ph/0304122.

[32] F. Hautmann. "Endpoint singularities in unintegrated parton distributions". In: *Phys. Lett. B* 655 (2007), pp. 26–31. DOI: 10.1016/j.physletb.2007.08.081. arXiv: hep-ph/0702196.

[33] John C. Collins and F. Hautmann. "Infrared divergences and nonlightlike eikonal lines in Sudakov processes". In: *Phys. Lett. B* 472 (2000), pp. 129–134. DOI: 10.1016/S0370-2693(99)01384-2. arXiv: hep-ph/9908467.

[34] John C. Collins and F. Hautmann. "Soft gluons and gauge invariant subtractions in NLO parton shower Monte Carlo event generators". In: *JHEP* 03 (2001), p. 016. DOI: 10.1088/1126-6708/2001/03/016. arXiv: hep-ph/0009286.

[35] S. D. Drell and Tung-Mow Yan. "Massive Lepton Pair Production in Hadron-Hadron Collisions at High-Energies". In: *Phys. Rev. Lett.* 25 (1970). [Erratum: Phys.Rev.Lett. 25, 902 (1970)], pp. 316–320. DOI: 10.1103/PhysRevLett.25.316.

[36] Georges Aad et al. "Precise measurements of W- and Z-boson transverse momentum spectra with the ATLAS detector using pp collisions at $\sqrt{s} = 5.02$ TeV and 13 TeV". In: *Eur. Phys. J. C* 84.10 (2024), p. 1126. DOI: 10.1140/epjc/s10052-024-13414-0. arXiv: 2404.06204 [hep-ex].

[37] Armen Tumasyan et al. "Measurement of the mass dependence of the transverse momentum of lepton pairs in Drell-Yan production in proton-proton collisions at $\sqrt{s}$ = 13 TeV". In: *Eur. Phys. J. C* 83.7 (2023), p. 628. DOI: 10.1140/epjc/s10052-023-11631-7. arXiv: 2205.04897 [hep-ex].

[38] Roel Aaij et al. "Measurement of the Z boson production cross-section in pp collisions at $\sqrt{s} = 5.02$ TeV". In: *JHEP* 02 (2024), p. 070. DOI: 10.1007/JHEP02(2024)070. arXiv: 2308.12940 [hep-ex].

[39] E. Accomando et al. "Constraining Parton Distribution Functions from Neutral Current Drell-Yan Measurements". In: *Phys. Rev. D* 98.1 (2018). [Erratum: Phys.Rev.D 99, 079902 (2019)], p. 013003. DOI: 10.1103/PhysRevD.98.013003. arXiv: 1712.06318 [hep-ph].

[40] Elena Accomando et al. "Neutral current forward-backward asymmetry: from θ_W to PDF determinations". In: *Eur. Phys. J. C* 78.8 (2018). [Erratum: Eur.Phys.J.C 79, 453 (2019)], p. 663. DOI: 10.1140/epjc/s10052-018-6120-6. arXiv: 1805.09239 [hep-ph].

[41] Elena Accomando et al. "PDF Profiling Using the Forward-Backward Asymmetry in Neutral Current Drell-Yan Production". In: *JHEP* 10 (2019), p. 176. DOI: 10.1007/JHEP10(2019)176. arXiv: 1907.07727 [hep-ph].

[42] Juri Fiaschi et al. "Lepton-Charge and Forward-Backward Asymmetries in Drell-Yan Processes for Precision Electroweak Measurements and New Physics Searches". In: *Nucl. Phys. B* 968 (2021), p. 115444. DOI: 10.1016/j.nuclphysb.2021.115444. arXiv: 2103.10224 [hep-ph].

[43] Yao Fu et al. "Probing parton distribution functions at large x via Drell-Yan forward-backward asymmetry". In: *Phys. Rev. D* 109.5 (2024), p. 054006. DOI: 10.1103/PhysRevD.109.054006. arXiv: 2307.07839 [hep-ph].

[44] Mingzhe Xie et al. "Measurement of the proton structure parameters in the forward-backward charge asymmetry". In: *Phys. Rev. D* 107.5 (2023), p. 054008. DOI: 10.1103/PhysRevD.107.054008. arXiv: 2209.13143 [hep-ex].

[45] Siqi Yang et al. "Factorization of the forward-backward asymmetry and measurements of the weak mixing angle and proton structure at hadron colliders". In: *Phys. Rev. D* 106.3 (2022), p. 033001. DOI: 10.1103/PhysRevD.106.033001. arXiv: 2202.13628 [hep-ph].

[46] Yao Fu et al. "Further Reduction of the PDF Uncertainty in the High-Mass Drell-Yan Spectrum Utilizing Neutral and Charged Current Inputs". In: (Nov. 2025). arXiv: 2511.15683 [hep-ph].

[47] Juri Fiaschi et al. "Enhancing the Large Hadron Collider sensitivity to charged and neutral broad resonances of new gauge sectors". In: *JHEP* 02 (2022), p. 179. DOI: 10.1007/JHEP02(2022)179. arXiv: 2111.09698 [hep-ph].

[48] J. Fiaschi et al. "Z'-boson dilepton searches and the high-x quark density". In: *Phys. Lett. B* 841 (2023), p. 137915. DOI: 10.1016/j.physletb.2023.137915. arXiv: 2211.06188 [hep-ph].

[49] Elena Accomando et al. "Photon-initiated production of a dilepton final state at the LHC: Cross section versus forward-backward asymmetry studies". In: *Phys. Rev. D* 95.3 (2017), p. 035014. DOI: 10.1103/PhysRevD.95.035014. arXiv: 1606.06646 [hep-ph].

[50] Elena Accomando et al. "The effect of real and virtual photons in the di-lepton channel at the LHC". In: *Phys. Lett. B* 770 (2017), pp. 1–7. DOI: 10.1016/j.physletb.2017.04.025. arXiv: 1612.08168 [hep-ph].

[51] Víctor Bresó-Pla, Adam Falkowski and Martín González-Alonso. "A_{FB} in the SMEFT: precision Z physics at the LHC". In: *JHEP* 08 (2021), p. 021. DOI: 10.1007/JHEP08(2021)021. arXiv: 2103.12074 [hep-ph].

[52] Hamed Abdolmaleki et al. "Exploring SMEFT couplings using the forward-backward asymmetry in neutral current Drell-Yan production at the LHC". In: *Eur. Phys. J. C* 84.12 (2024), p. 1277. DOI: 10.1140/epjc/s10052-024-13480-4. arXiv: 2310.19638 [hep-ph].

[53] Yuri L. Dokshitzer, Dmitri Diakonov and S. I. Troian. "On the Transverse Momentum Distribution of Massive Lepton Pairs". In: *Phys. Lett. B* 79 (1978), pp. 269–272. DOI: 10.1016/0370-2693(78)90240-X.

[54] G. Parisi and R. Petronzio. "Small Transverse Momentum Distributions in Hard Processes". In: *Nucl. Phys. B* 154 (1979), pp. 427–440. DOI: 10.1016/0550-3213(79)90040-3.

[55] G. Curci and Mario Greco. "Large Infra-red Corrections in QCD Processes". In: *Phys. Lett. B* 92 (1980). Ed. by Mario Greco, pp. 175–178. DOI: 10.1016/0370-2693(80)90331-7.

[56] Guido Altarelli et al. "Vector Boson Production at Colliders: A Theoretical Reappraisal". In: *Nucl. Phys. B* 246 (1984). Ed. by Mario Greco, pp. 12–44. DOI: 10.1016/0550-3213(84)90112-3.

[57] John C. Collins, Davison E. Soper and George F. Sterman. "Transverse Momentum Distribution in Drell-Yan Pair and W and Z Boson Production". In: *Nucl. Phys. B* 250 (1985), pp. 199–224. DOI: 10.1016/0550-3213(85)90479-1.

[58] Stefano Camarda, Giancarlo Ferrera and Matthias Schott. "Determination of the strong-coupling constant from the Z-boson transverse-momentum distribution". In: *Eur. Phys. J. C* 84.1 (2024), p. 39. DOI: 10.1140/epjc/s10052-023-12373-2. arXiv: 2203.05394 [hep-ph].

[59] Stefano Camarda, Leandro Cieri and Giancarlo Ferrera. "Drell-Yan lepton-pair production: qT resummation at N3LL accuracy and fiducial cross sections at N3LO". In: *Phys. Rev. D* 104.11 (2021), p. L111503. DOI: 10.1103/PhysRevD.104.L111503. arXiv: 2103.04974 [hep-ph].

[60] Stefano Camarda et al. "DYTurbo: Fast predictions for Drell-Yan processes". In: *Eur. Phys. J. C* 80.3 (2020). [Erratum: Eur.Phys.J.C 80, 440 (2020)], p. 251. DOI: 10.1140/epjc/s10052-020-7757-5. arXiv: 1910.07049 [hep-ph].

[61] Francesco Coradeschi and Thomas Cridge. "reSolve — A transverse momentum resummation tool". In: *Comput. Phys. Commun.* 238 (2019), pp. 262–294. DOI: 10.1016/j.cpc.2018.11.024. arXiv: 1711.02083 [hep-ph].

[62] E. Accomando et al. "Production of Z'-boson resonances with large width at the LHC". In: *Phys. Lett. B* 803 (2020), p. 135293. DOI: 10.1016/j.physletb.2020.135293. arXiv: 1910.13759 [hep-ph].

[63] Joshua Isaacson, Yao Fu and C. -P. Yuan. "resbos2 and the CDF W mass measurement". In: *Phys. Rev. D* 110.9 (2024), p. 094023. DOI: 10.1103/PhysRevD.110.094023. arXiv: 2205.02788 [hep-ph].

[64] Georgios Billis, Johannes K. L. Michel and Frank J. Tackmann. "Drell-Yan Transverse-Momentum Spectra at N^{3}LL$'$ and Approximate N^{4}LL with SCETlib". In: (Nov. 2024). arXiv: 2411.16004 [hep-ph].

[65] Markus A. Ebert et al. "Drell-Yan q_T resummation of fiducial power corrections at N^{3}LL". In: *JHEP* 04 (2021), p. 102. DOI: 10.1007/JHEP04(2021)102. arXiv: 2006.11382 [hep-ph].

[66] Markus A. Ebert and Frank J. Tackmann. "Resummation of Transverse Momentum Distributions in Distribution Space". In: *JHEP* 02 (2017), p. 110. DOI: 10.1007/JHEP02(2017)110. arXiv: 1611.08610 [hep-ph].

[67] John Campbell and Tobias Neumann. "Third order QCD predictions for fiducial W-boson production". In: *JHEP* 11 (2023), p. 127. DOI: 10.1007/JHEP11(2023)127. arXiv: 2308.15382 [hep-ph].

[68] Thomas Becher and Tobias Neumann. "Fiducial q_T resummation of color-singlet processes at N^{3}LL+NNLO". In: *JHEP* 03 (2021), p. 199. DOI: 10.1007/JHEP03(2021)199. arXiv: 2009.11437 [hep-ph].

[69] Tobias Neumann and John Campbell. "Fiducial Drell-Yan production at the LHC improved by transverse-momentum resummation at N4LLp+N3LO". In: *Phys. Rev. D* 107.1 (2023), p. L011506. DOI: 10.1103/PhysRevD.107.L011506. arXiv: 2207.07056 [hep-ph].

[70] A. Bermudez Martinez et al. "Production of Z-bosons in the parton branching method". In: *Phys. Rev. D* 100.7 (2019), p. 074027. DOI: 10.1103/PhysRevD.100.074027. arXiv: 1906.00919 [hep-ph].

[71] A. Bermudez Martinez et al. "The transverse momentum spectrum of low mass Drell–Yan production at next-to-leading order in the parton branching method". In: *Eur. Phys. J. C* 80.7 (2020), p. 598. DOI: 10.1140/epjc/s10052-020-8136-y. arXiv: 2001.06488 [hep-ph].

[72] A. Bermudez Martinez et al. "Collinear and TMD parton densities from fits to precision DIS measurements in the parton branching method". In: *Phys. Rev. D* 99.7 (2019), p. 074008. DOI: 10.1103/PhysRevD.99.074008. arXiv: 1804.11152 [hep-ph].

[73] F. Hautmann et al. "Collinear and TMD Quark and Gluon Densities from Parton Branching Solution of QCD Evolution Equations". In: *JHEP* 01 (2018), p. 070. DOI: 10.1007/JHEP01(2018)070. arXiv: 1708.03279 [hep-ph].

[74] F. Hautmann et al. "Soft-gluon resolution scale in QCD evolution equations". In: *Phys. Lett.* B772 (2017), pp. 446–451. DOI: 10.1016/j.physletb.2017.07.005. arXiv: 1704.01757 [hep-ph].

[75] Xuan Chen et al. "Third-Order Fiducial Predictions for Drell-Yan Production at the LHC". In: *Phys. Rev. Lett.* 128.25 (2022), p. 252001. DOI: 10.1103/PhysRevLett.128.252001. arXiv: 2203.01565 [hep-ph].

[76] Wojciech Bizon et al. "The transverse momentum spectrum of weak gauge bosons at N ^{3} LL + NNLO". In: *Eur. Phys. J. C* 79.10 (2019), p. 868. DOI: 10.1140/epjc/s10052-019-7324-0. arXiv: 1905.05171 [hep-ph].

[77] Alessandro Bacchetta et al. "Unpolarized transverse momentum distributions from a global fit of Drell-Yan and semi-inclusive deep-inelastic scattering data". In: *JHEP* 10 (2022), p. 127. DOI: 10.1007/JHEP10(2022)127. arXiv: 2206.07598 [hep-ph].

[78] Alessandro Bacchetta et al. "Flavor dependence of unpolarized quark transverse momentum distributions from a global fit". In: *JHEP* 08 (2024), p. 232. DOI: 10.1007/JHEP08(2024)232. arXiv: 2405.13833 [hep-ph].

[79] Marcin Bury et al. "PDF bias and flavor dependence in TMD distributions". In: *JHEP* 10 (2022), p. 118. DOI: 10.1007/JHEP10(2022)118. arXiv: 2201.07114 [hep-ph].

[80] Francesco Hautmann, Ignazio Scimemi and Alexey Vladimirov. "Non-perturbative contributions to vector-boson transverse momentum spectra in hadronic collisions". In: *Phys. Lett. B* 806 (2020), p. 135478. DOI: 10.1016/j.physletb.2020.135478. arXiv: 2002.12810 [hep-ph].

[81] I. Bubanja et al. "The small k_{T} region in Drell-Yan production at next-to-leading order with the parton branching method". In: *Eur. Phys. J. C* 84.2 (2024), p. 154. DOI: 10.1140/epjc/s10052-024-12507-0. arXiv: 2312.08655 [hep-ph].

[82] F. Hautmann et al. "Collinear and TMD distributions with dynamical soft-gluon resolution scale". In: *JHEP* 06 (2025), p. 192. DOI: 10.1007/JHEP06(2025)192. arXiv: 2502.19380 [hep-ph].

[83] L. Moureaux et al. "Intrinsic k_T and soft gluons in Monte Carlo event generators". In: *2025 European Physical Society Conference on High Energy Physics*. Nov. 2025. arXiv: 2511.23291 [hep-ph].

[84] Wenxiao Zhan et al. "Coarse-grained binning in Drell-Yan transverse momentum spectra". In: *Phys. Rev. D* 111.3 (2025), p. 036018. DOI: 10.1103/PhysRevD.111.036018. arXiv: 2412.19060 [hep-ph].

[85] Wenxiao Zhan et al. "A p_T-ratio observable for studies of intrinsic transverse momentum of partons from Drell-Yan p_T spectra". In: *59th Rencontres de Moriond on QCD and High Energy Interactions: Moriond QCD 2025*. May 2025. arXiv: 2505.06973 [hep-ph].

[86] Artur Avkhadiev et al. "Determination of the Collins-Soper Kernel from Lattice QCD". In: *Phys. Rev. Lett.* 132.23 (2024), p. 231901. DOI: 10.1103/PhysRevLett.132.231901. arXiv: 2402.06725 [hep-lat].

[87] Min-Huan Chu et al. "Lattice calculation of the intrinsic soft function and the Collins-Soper kernel". In: *JHEP* 08 (2023), p. 172. DOI: 10.1007/JHEP08(2023)172. arXiv: 2306.06488 [hep-lat].

[88] Zhi-Fu Deng, Wei Wang and Jun Zeng. "Transverse-momentum-dependent wave functions and soft functions at one-loop in large momentum effective theory". In: *JHEP* 09 (2022), p. 046. DOI: 10.1007/JHEP09(2022)046. arXiv: 2207.07280 [hep-th].

[89] Hai-Tao Shu et al. "Universality of the Collins-Soper kernel in lattice calculations". In: *Phys. Rev. D* 108.7 (2023), p. 074519. DOI: 10.1103/PhysRevD.108.074519. arXiv: 2302.06502 [hep-lat].

[90] Dennis Bollweg et al. "Transverse-momentum-dependent pion structures from lattice QCD: Collins-Soper kernel, soft factor, TMDWF, and TMDPDF". In: (Apr. 2025). arXiv: 2504.04625 [hep-lat].

[91] A. Bermudez Martinez et al. "Soft-gluon coupling and the TMD parton branching Sudakov form factor". In: *Phys. Lett. B* 868 (2025), p. 139762. DOI: 10.1016/j.physletb.2025.139762. arXiv: 2412.21116 [hep-ph].

[92] A. Bermudez Martinez et al. "The Parton Branching Sudakov and its relation to CSS". In: *PoS* EPS-HEP2023 (2024), p. 270. DOI: 10.22323/1.449.0270.

[93] H. Yang et al. "Back-to-back azimuthal correlations in Z+jet events at high transverse momentum in the TMD parton branching method at next-to-leading order". In: *Eur. Phys. J. C* 82.8 (2022), p. 755. DOI: 10.1140/epjc/s10052-022-10715-0. arXiv: 2204.01528 [hep-ph].

[94] M. I. Abdulhamid et al. "Azimuthal correlations of high transverse momentum jets at next-to-leading order in the parton branching method". In: *Eur. Phys. J. C* 82.1 (2022), p. 36. DOI: 10.1140/epjc/s10052-022-09997-1. arXiv: 2112.10465 [hep-ph].

[95] A. Bermudez Martinez, F. Hautmann and M. L. Mangano. "Multi-jet merging with TMD parton branching". In: *JHEP* 09 (2022), p. 060. DOI: 10.1007/JHEP09(2022)060. arXiv: 2208.02276 [hep-ph].

[96] A. Bermudez Martinez, F. Hautmann and M. L. Mangano. "TMD evolution and multi-jet merging". In: *Phys. Lett. B* 822 (2021), p. 136700. DOI: 10.1016/j.physletb.2021.136700. arXiv: 2107.01224 [hep-ph].

[97] A. Bermudez Martinez, F. Hautmann and M. L. Mangano. "Multi-jet physics at high-energy colliders and TMD parton evolution". In: Sept. 2021. arXiv: 2109.08173 [hep-ph].

[98] Armando Bermudez Martinez and Francesco Hautmann. "Parton branching TMD method and multi-jet production". In: *PoS* ICHEP2020 (2021), p. 453. DOI: 10.22323/1.390.0453.

[99] S. Baranov et al. "CASCADE3 A Monte Carlo event generator based on TMDs". In: *Eur. Phys. J. C* 81.5 (2021), p. 425. DOI: 10.1140/epjc/s10052-021-09203-8. arXiv: 2101.10221 [hep-ph].

[100] H. Jung et al. "The CCFM Monte Carlo generator CASCADE version 2.2.03". In: *Eur. Phys. J. C* 70 (2010), pp. 1237–1249. DOI: 10.1140/epjc/s10052-010-1507-z. arXiv: 1008.0152 [hep-ph].

[101] F. Hautmann. "TMDs and Monte Carlo Event Generators". In: *PoS* SPIN2018 (2019). Ed. by Paolo Lenisa et al., p. 059. DOI: 10.22323/1.346.0059. arXiv: 1907.03353 [hep-ph].

[102] S. Dooling et al. "Longitudinal momentum shifts, showering, and nonperturbative corrections in matched next-to-leading-order shower event generators". In: *Phys. Rev. D* 87.9 (2013), p. 094009. DOI: 10.1103/PhysRevD.87.094009. arXiv: 1212.6164 [hep-ph].

[103] F. Hautmann and H. Jung. "Collinearity approximations and kinematic shifts in partonic shower algorithms". In: *Eur. Phys. J. C* 72 (2012), p. 2254. DOI: 10.1140/epjc/s10052-012-2254-0. arXiv: 1209.6549 [hep-ph].

[104] F. Hautmann and H. Jung. "Three-jet DIS final states from k(T)-dependent parton showers". In: *PoS* RADCOR2007 (2007). Ed. by Stefano Catani, Dimitri Colferai and Massimiliano Grazzini, p. 030. DOI: 10.22323/1.048.0030. arXiv: 0804.1746 [hep-ph].

[105] N. A. Abdulov et al. "TMDlib2 and TMDplotter: a platform for 3D hadron structure studies". In: *Eur. Phys. J. C* 81.8 (2021), p. 752. DOI: 10.1140/epjc/s10052-021-09508-8. arXiv: 2103.09741 [hep-ph].

[106] F. Hautmann et al. "TMDlib and TMDplotter: library and plotting tools for transverse-momentum-dependent parton distributions". In: *Eur. Phys. J.* C74 (2014), p. 3220. DOI: 10.1140/epjc/s10052-014-3220-9. arXiv: 1408.3015 [hep-ph].

[107] Andy Buckley et al. "LHAPDF6: parton density access in the LHC precision era". In: *Eur. Phys. J.* C75 (2015), p. 132. DOI: 10.1140/epjc/s10052-015-3318-8. arXiv: 1412.7420 [hep-ph].

[108] Richard D. Ball et al. "The PDF4LHC21 combination of global PDF fits for the LHC Run III". In: *J. Phys. G* 49.8 (2022), p. 080501. DOI: 10.1088/1361-6471/ac7216. arXiv: 2203.05506 [hep-ph].

[109] Richard D. Ball et al. "The path to proton structure at 1% accuracy". In: *Eur. Phys. J. C* 82.5 (2022), p. 428. DOI: 10.1140/epjc/s10052-022-10328-7. arXiv: 2109.02653 [hep-ph].

[110] Rabah Abdul Khalek et al. "Parton Distributions with Theory Uncertainties: General Formalism and First Phenomenological Studies". In: *Eur. Phys. J. C* 79.11 (2019), p. 931. DOI: 10.1140/epjc/s10052-019-7401-4. arXiv: 1906.10698 [hep-ph].

[111] S. Bailey et al. "Parton distributions from LHC, HERA, Tevatron and fixed target data: MSHT20 PDFs". In: *Eur. Phys. J. C* 81.4 (2021), p. 341. DOI: 10.1140/epjc/s10052-021-09057-0. arXiv: 2012.04684 [hep-ph].

[112] Tie-Jiun Hou et al. "New CTEQ global analysis of quantum chromodynamics with high-precision data from the LHC". In: *Phys. Rev. D* 103.1 (2021), p. 014013. DOI: 10.1103/PhysRevD.103.014013. arXiv: 1912.10053 [hep-ph].

[113] S. Alekhin et al. "Parton distribution functions, α_s, and heavy-quark masses for LHC Run II". In: *Phys. Rev. D* 96.1 (2017), p. 014011. DOI: 10.1103/PhysRevD.96.014011. arXiv: 1701.05838 [hep-ph].

[114] S. Alekhin et al. "HERAFitter". In: *Eur. Phys. J. C* 75.7 (2015), p. 304. DOI: 10.1140/epjc/s10052-015-3480-z. arXiv: 1410.4412 [hep-ph].

[115] H. Abdolmaleki et al. "xFitter: An Open Source QCD Analysis Framework. A resource and reference document for the Snowmass study". In: June 2022. arXiv: 2206.12465 [hep-ph].

[116] H. Abramowicz et al. "Combination of measurements of inclusive deep inelastic $e^{\pm}p$ scattering cross sections and QCD analysis of HERA data". In: *Eur. Phys. J. C* 75.12 (2015), p. 580. DOI: 10.1140/epjc/s10052-015-3710-4. arXiv: 1506.06042 [hep-ex].

[117] P. Azzi et al. "Report from Working Group 1: Standard Model Physics at the HL-LHC and HE-LHC". In: *CERN Yellow Rep. Monogr.* 7 (2019). Ed. by Andrea Dainese et al., pp. 1–220. DOI: 10.23731/CYRM-2019-007.1. arXiv: 1902.04070 [hep-ph].

[118] P. Agostini et al. "The Large Hadron–Electron Collider at the HL-LHC". In: *J. Phys. G* 48.11 (2021), p. 110501. DOI: 10.1088/1361-6471/abf3ba. arXiv: 2007.14491 [hep-ex].

[119] A. Abada et al. "FCC Physics Opportunities: Future Circular Collider Conceptual Design Report Volume 1". In: *Eur. Phys. J. C* 79.6 (2019), p. 474. DOI: 10.1140/epjc/s10052-019-6904-3.

[120] Yoshitaka Hatta et al. "Proceedings, Probing Nucleons and Nuclei in High Energy Collisions: Dedicated to the Physics of the Electron Ion Collider: Seattle (WA), United States, October 1 - November 16, 2018". In: (Feb. 2020). DOI: 10.1142/11684. arXiv: 2002.12333 [hep-ph].

[121] V. Bertone et al. "Resummation Scales and the Assessment of Theoretical Uncertainties in Parton Distribution Functions". In: *29th International Workshop on Deep-Inelastic Scattering and Related Subjects*. May 2022. arXiv: 2205.15900 [hep-ph].

[122] V. Bertone et al. "Structure functions and perturbative hysteresis". In: *PoS* EPS-HEP2023 (2024), p. 256. DOI: 10.22323/1.449.0256.

[123] S. Catani and F. Hautmann. "Quark anomalous dimensions at small x". In: *Phys. Lett. B* 315 (1993), pp. 157–163. DOI: 10.1016/0370-2693(93)90174-G.

[124] S. Catani and F. Hautmann. "High-energy factorization and small x deep inelastic scattering beyond leading order". In: *Nucl. Phys. B* 427 (1994), pp. 475–524. DOI: 10.1016/0550-3213(94)90636-X. arXiv: hep-ph/9405388.

[125] R. Keith Ellis, F. Hautmann and B. R. Webber. "QCD scaling violation at small x". In: *Phys. Lett. B* 348 (1995), pp. 582–588. DOI: 10.1016/0370-2693(95)00148-E. arXiv: hep-ph/9501307.

[126] Jeffrey R. Forshaw, R. G. Roberts and R. S. Thorne. "Analytic approach to small x structure functions". In: *Phys. Lett. B* 356 (1995), pp. 79–88. DOI: 10.1016/0370-2693(95)00812-Y. arXiv: hep-ph/9504336.

[127] Richard D. Ball and Stefano Forte. "Summation of leading logarithms at small x". In: *Phys. Lett. B* 351 (1995), pp. 313–324. DOI: 10.1016/0370-2693(95)00395-2. arXiv: hep-ph/9501231.

[128] J. Kwiecinski, Alan D. Martin and A. M. Stasto. "A Unified BFKL and GLAP description of F2 data". In: *Phys. Rev. D* 56 (1997), pp. 3991–4006. DOI: 10.1103/PhysRevD.56.3991. arXiv: hep-ph/9703445.

[129] M. Ciafaloni et al. "A Matrix formulation for small-x singlet evolution". In: *JHEP* 08 (2007), p. 046. DOI: 10.1088/1126-6708/2007/08/046. arXiv: 0707.1453 [hep-ph].

[130] Guido Altarelli, Richard D. Ball and Stefano Forte. "Small x Resummation with Quarks: Deep-Inelastic Scattering". In: *Nucl. Phys. B* 799 (2008), pp. 199–240. DOI: 10.1016/j.nuclphysb.2008.03.003. arXiv: 0802.0032 [hep-ph].

[131] C. D. White and R. S. Thorne. "A Global Fit to Scattering Data with NLL BFKL Resummations". In: *Phys. Rev. D* 75 (2007), p. 034005. DOI: 10.1103/PhysRevD.75.034005. arXiv: hep-ph/0611204.

[132] Richard D. Ball et al. "Parton distributions with small-x resummation: evidence for BFKL dynamics in HERA data". In: *Eur. Phys. J. C* 78.4 (2018), p. 321. DOI: 10.1140/epjc/s10052-018-5774-4. arXiv: 1710.05935 [hep-ph].

[133] Hamed Abdolmaleki et al. "Impact of low-x resummation on QCD analysis of HERA data". In: *Eur. Phys. J. C* 78.8 (2018), p. 621. DOI: 10.1140/epjc/s10052-018-6090-8. arXiv: 1802.00064 [hep-ph].

[134] S. Catani et al. "GLUON CONTRIBUTIONS TO SMALL x HEAVY FLAVOR PRODUCTION". In: *Phys. Lett. B* 242 (1990), pp. 97–102. DOI: 10.1016/0370-2693(90)91601-7.

[135] S. Catani et al. "High-energy factorization and small x heavy flavor production". In: *Nucl. Phys. B* 366 (1991), pp. 135–188. DOI: 10.1016/0550-3213(91)90055-3.

[136] S. Catani et al. "High-energy factorization in QCD and minimal subtraction scheme". In: *Phys. Lett. B* 307 (1993), pp. 147–153. DOI: 10.1016/0370-2693(93)90204-U.

[137] Paul Caucal et al. "Unveiling the sea: universality of the transverse momentum dependent quark distributions at small x". In: (Mar. 2025). arXiv: 2503.16162 [hep-ph].

[138] Paul Caucal et al. "Gluon splitting at small x: a unified derivation for the JIMWLK, DGLAP and CSS equations". In: (Oct. 2025). arXiv: 2510.08454 [hep-ph].

[139] Tolga Altinoluk, Jamal Jalilian-Marian and Cyrille Marquet. "Sudakov double logs in single-inclusive hadron production in DIS at small x from the color glass condensate formalism". In: *Phys. Rev. D* 110.9 (2024), p. 094056. DOI: 10.1103/PhysRevD.110.094056. arXiv: 2406.08277 [hep-ph].

[140] Yu Shi, Shu-Yi Wei and Jian Zhou. "Parton shower algorithm with the saturation effect". In: *Phys. Rev. D* 108.9 (2023), p. 096025. DOI: 10.1103/PhysRevD.108.096025. arXiv: 2307.04185 [hep-ph].

[141] Leszek Motyka and Mariusz Sadzikowski. "Twist decomposition of non-linear effects in Balitsky–Kovchegov evolution of proton structure functions". In: *Eur. Phys. J. C* 83.11 (2023), p. 1062. DOI: 10.1140/epjc/s10052-023-12241-z. arXiv: 2306.02118 [hep-ph].

[142] A. van Hameren et al. "Searching for saturation in forward dijet production at the LHC". In: *Eur. Phys. J. C* 83.10 (2023), p. 947. DOI: 10.1140/epjc/s10052-023-12120-7. arXiv: 2306.17513 [hep-ph].

[143] Haowu Duan, Alex Kovner and Michael Lublinsky. "Born-Oppenheimer renormalization group for high energy scattering: CSS, DGLAP and all that". In: *JHEP* 08 (2025), p. 137. DOI: 10.1007/JHEP08(2025)137. arXiv: 2412.05097 [hep-ph].

[144] Haowu Duan, Alex Kovner and Michael Lublinsky. "Born-Oppenheimer renormalization group for high energy scattering: the setup and the wave function". In: *JHEP* 08 (2025), p. 136. DOI: 10.1007/JHEP08(2025)136. arXiv: 2412.05085 [hep-ph].

[145] G. Curci, W. Furmanski and R. Petronzio. "Evolution of Parton Densities Beyond Leading Order: The Nonsinglet Case". In: *Nucl. Phys. B* 175 (1980), pp. 27–92. DOI: 10.1016/0550-3213(80)90003-6.

[146] W. Furmanski and R. Petronzio. "Singlet Parton Densities Beyond Leading Order". In: *Phys. Lett. B* 97 (1980), pp. 437–442. DOI: 10.1016/0370-2693(80)90636-X.

[147] S. Moch, J. A. M. Vermaseren and A. Vogt. "The Three loop splitting functions in QCD: The Nonsinglet case". In: *Nucl. Phys. B* 688 (2004), pp. 101–134. DOI: 10.1016/j.nuclphysb.2004.03.030. arXiv: hep-ph/0403192.

[148] A. Vogt, S. Moch and J. A. M. Vermaseren. "The Three-loop splitting functions in QCD: The Singlet case". In: *Nucl. Phys. B* 691 (2004), pp. 129–181. DOI: 10.1016/j.nuclphysb.2004.04.024. arXiv: hep-ph/0404111.

[149] G. Falcioni et al. "Four-loop splitting functions in QCD – The quark-quark case". In: *Phys. Lett. B* 842 (2023), p. 137944. DOI: 10.1016/j.physletb.2023.137944. arXiv: 2302.07593 [hep-ph].

[150] G. Falcioni et al. "Four-loop splitting functions in QCD – The gluon-to-quark case". In: *Phys. Lett. B* 846 (2023), p. 138215. DOI: 10.1016/j.physletb.2023.138215. arXiv: 2307.04158 [hep-ph].

[151] S. Moch et al. "Additional moments and x-space approximations of four-loop splitting functions in QCD". In: *Phys. Lett. B* 849 (2024), p. 138468. DOI: 10.1016/j.physletb.2024.138468. arXiv: 2310.05744 [hep-ph].

[152] Thomas Gehrmann et al. "The NfCF3 contribution to the non-singlet splitting function at four-loop order". In: *Phys. Lett. B* 849 (2024), p. 138427. DOI: 10.1016/j.physletb.2023.138427. arXiv: 2310.12240 [hep-ph].

[153] Thomas Gehrmann et al. "Complete N_f^2 contributions to four-loop pure-singlet splitting functions". In: *JHEP* 01 (2024), p. 029. DOI: 10.1007/JHEP01(2024)029. arXiv: 2308.07958 [hep-ph].

[154] J. McGowan et al. "Approximate N^{3}LO parton distribution functions with theoretical uncertainties: MSHT20aN^{3}LO PDFs". In: *Eur. Phys. J. C* 83.3 (2023). [Erratum: Eur.Phys.J.C 83, 302 (2023)], p. 185. DOI: 10.1140/epjc/s10052-023-11236-0. arXiv: 2207.04739 [hep-ph].

[155] Thomas Cridge, Lucian A. Harland-Lang and Robert S. Thorne. "Combining QED and approximate N^{3}LO QCD corrections in a global PDF fit: MSHT20qed_an3lo PDFs". In: *SciPost Phys.* 17.1 (2024), p. 026. DOI: 10.21468/SciPostPhys.17.1.026. arXiv: 2312.07665 [hep-ph].

[156] T. Cridge, L. A. Harland-Lang and R. S. Thorne. "The impact of LHC jet and Zp_T data at up to approximate N^{3}LO order in the MSHT global PDF fit". In: *Eur. Phys. J. C* 84.4 (2024), p. 446. DOI: 10.1140/epjc/s10052-024-12771-0. arXiv: 2312.12505 [hep-ph].

[157] Richard D. Ball et al. "The path to N^{3}LO parton distributions". In: *Eur. Phys. J. C* 84.7 (2024), p. 659. DOI: 10.1140/epjc/s10052-024-12891-7. arXiv: 2402.18635 [hep-ph].

[158] Valerio Bertone. *APFEL++: A new PDF evolution library in C++*. 2017. arXiv: 1708.00911 [hep-ph]. URL: https://arxiv.org/abs/1708.00911.

[159] Valerio Bertone, Stefano Carrazza and Juan Rojo. "APFEL: A PDF evolution library with QED corrections". In: *Computer Physics Communications* 185.6 (June 2014), pp. 1647–1668. ISSN: 0010-4655. DOI: 10.1016/j.cpc.2014.03.007. URL: http://dx.doi.org/10.1016/j.cpc.2014.03.007.

[160] F. Hautmann. "Heavy top limit and double logarithmic contributions to Higgs production at m(H)**2 / s much less than 1". In: *Phys. Lett. B* 535 (2002), pp. 159–162. DOI: 10.1016/S0370-2693(02)01761-6. arXiv: hep-ph/0203140.

[161] Marco Bonvini and Simone Marzani. "Double resummation for Higgs production". In: *Phys. Rev. Lett.* 120.20 (2018), p. 202003. DOI: 10.1103/PhysRevLett.120.202003. arXiv: 1802.07758 [hep-ph].

[162] S. Amoroso et al. "Longitudinal Z-boson polarization and the Higgs boson production cross section at the Large Hadron Collider". In: *Phys. Lett. B* 821 (2021), p. 136613. DOI: 10.1016/j.physletb.2021.136613. arXiv: 2012.10298 [hep-ph].

[163] F. E. Barattini, C. O. Dib and B. Guiot. "Heavy-hadron production based on k_t-factorization with scale-dependent fragmentation functions". In: *JHEP* 05 (2025), p. 115. DOI: 10.1007/JHEP05(2025)115. arXiv: 2501.17662 [hep-ph].

[164] Cyrille Marquet, Yu Shi and Bo-Wen Xiao. "Unified Resummation of Soft Gluon Radiation in Heavy Meson Pair Photoproduction". In: (Oct. 2025). arXiv: 2510.18949 [hep-ph].

[165] B. Guiot and A. van Hameren. "D and B-meson production using kt-factorization calculations in a variable-flavor-number scheme". In: *Phys. Rev. D* 104.9 (2021), p. 094038. DOI: 10.1103/PhysRevD.104.094038. arXiv: 2108.06419 [hep-ph].

[166] Benjamin Guiot. "Heavy-quark production with k_t-factorization: The importance of the sea-quark distribution". In: *Phys. Rev. D* 99.7 (2019), p. 074006. DOI: 10.1103/PhysRevD.99.074006. arXiv: 1812.02156 [hep-ph].

[167] A. V. Lipatov et al. "TMD gluon density in nuclei versus experimental data on heavy flavor production at LHC". In: *Phys. Lett. B* 850 (2024), p. 138486. DOI: 10.1016/j.physletb.2024.138486. arXiv: 2312.00365 [hep-ph].

[168] Jean-Philippe Lansberg, Maxim Nefedov and Melih A. Ozcelik. "Curing the high-energy perturbative instability of vector-quarkonium-photoproduction cross sections at order $\alpha\alpha_s^3$ with high-energy factorisation". In: *Eur. Phys. J. C* 84.4 (2024), p. 351. DOI: 10.1140/epjc/s10052-024-12588-x. arXiv: 2306.02425 [hep-ph].

[169] Jean-Philippe Lansberg, Maxim Nefedov and Melih A. Ozcelik. "Matching next-to-leading-order and high-energy-resummed calculations of heavy-quarkonium-hadroproduction cross sections". In: *JHEP* 05 (2022), p. 083. DOI: 10.1007/JHEP05(2022)083. arXiv: 2112.06789 [hep-ph].

[170] S. P. Baranov et al. "Forward J/ψ+J/ψ and J/ψ+ψ' production with high-energy factorization". In: *Phys. Rev. D* 110.5 (2024), p. 054001. DOI: 10.1103/PhysRevD.110.054001. arXiv: 2405.18054 [hep-ph].

[171] B. Guiot et al. "J/ψ production at NLO with a scale-dependent color-evaporation model". In: *Phys. Rev. D* 108.11 (2023), p. 114003. DOI: 10.1103/PhysRevD.108.114003. arXiv: 2306.11032 [hep-ph].

[172] A. A. Prokhorov et al. "Tree-level NLO corrections to inclusive ?′ production in High Energy Factorization". In: (Sept. 2025). arXiv: 2509.09416 [hep-ph].

[173] C. A. Flett et al. "Exclusive vector-quarkonium photoproduction at NLO in αs in collinear factorisation with evolution of the generalised parton distributions and high-energy resummation". In: *Phys. Lett. B* 859 (2024), p. 139117. DOI: 10.1016/j.physletb.2024.139117. arXiv: 2409.05738 [hep-ph].

[174] Heikki Mäntysaari et al. "Global Bayesian Analysis of J/? Photoproduction on Proton and Lead Targets". In: (July 2025). arXiv: 2507.14087 [hep-ph].

[175] A. A. Chernyshev, M. A. Nefedov and V. A. Saleev. "New evidence for the BFKL dynamics in Mueller-Navelet dijet production via matching of the RG-invariant solution with high-energy factorization". In: (June 2025). arXiv: 2506.10458 [hep-ph].

[176] Pedro Agostini, Tolga Altinoluk and Néstor Armesto. "Next-to-eikonal corrections to dijet production in Deep Inelastic Scattering in the dilute limit of the Color Glass Condensate". In: *JHEP* 07 (2024), p. 137. DOI: 10.1007/JHEP07(2024)137. arXiv: 2403.04603 [hep-ph].

[177] Pieter Taels et al. "Dijet photoproduction at low x at next-to-leading order and its back-to-back limit". In: *JHEP* 10 (2022), p. 184. DOI: 10.1007/JHEP10(2022)184. arXiv: 2204.11650 [hep-ph].

[178] M. Deak et al. "Forward Jet Production at the Large Hadron Collider". In: *JHEP* 09 (2009), p. 121. DOI: 10.1088/1126-6708/2009/09/121. arXiv: 0908.0538 [hep-ph].

[179] M. Deak et al. "Jets in the forward region at the LHC". In: *44th Rencontres de Moriond on QCD and High Energy Interactions*. Aug. 2009, pp. 361–364. arXiv: 0908.1870 [hep-ph].

[180] M. Deak et al. "Forward-Central Jet Correlations at the Large Hadron Collider". In: (Dec. 2010). arXiv: 1012.6037 [hep-ph].

[181] M. Deak et al. "Forward Jets and Energy Flow in Hadronic Collisions". In: *Eur. Phys. J. C* 72 (2012), p. 1982. DOI: 10.1140/epjc/s10052-012-1982-5. arXiv: 1112.6354 [hep-ph].

[182] F. Hautmann, M. Hentschinski and H. Jung. "Forward Z-boson production and the unintegrated sea quark density". In: *Nucl. Phys. B* 865 (2012), pp. 54–66. DOI: 10.1016/j.nuclphysb.2012.07.023. arXiv: 1205.1759 [hep-ph].

[183] Maxim A. Nefedov and Vladimir A. Saleev. "High-Energy Factorization for Drell-Yan process in pp and $p\bar{p}$ collisions with new Unintegrated PDFs". In: *Phys. Rev. D* 102 (2020), p. 114018. DOI: 10.1103/PhysRevD.102.114018. arXiv: 2009.13188 [hep-ph].

[184] Shu-yi Wei. "Exploring the non-perturbative Sudakov factor via Z^0 -boson production in pp collisions". In: *Phys. Lett. B* 817 (2021), p. 136356. DOI: 10.1016/j.physletb.2021.136356. arXiv: 2009.06514 [hep-ph].

[185] Krzysztof Golec-Biernat and Tomasz Stebel. "Drell–Yan production with the CCFM-K evolution". In: *Eur. Phys. J. C* 80.5 (2020), p. 455. DOI: 10.1140/epjc/s10052-020-8026-3. arXiv: 1911.10103 [hep-ph].

[186] Krzysztof Golec-Biernat, Leszek Motyka and Tomasz Stebel. "Forward Drell-Yan and backward jet production as a probe of the BFKL dynamics". In: *JHEP* 12 (2018), p. 091. DOI: 10.1007/JHEP12(2018)091. arXiv: 1811.04361 [hep-ph].

[187] Cyrille Marquet, Shu-Yi Wei and Bo-Wen Xiao. "Probing parton saturation with forward Z^0-boson production at small transverse momentum in p+p and p+A collisions". In: *Phys. Lett. B* 802 (2020), p. 135253. DOI: 10.1016/j.physletb.2020.135253. arXiv: 1909.08572 [hep-ph].

[188] Wolfgang Schäfer and Antoni Szczurek. "Low mass Drell-Yan production of lepton pairs at forward directions at the LHC: a hybrid approach". In: *Phys. Rev. D* 93.7 (2016), p. 074014. DOI: 10.1103/PhysRevD.93.074014. arXiv: 1602.06740 [hep-ph].

[189] Pieter Taels. "Forward production of a Drell-Yan pair and a jet at small x at next-to-leading order". In: *JHEP* 01 (2024), p. 005. DOI: 10.1007/JHEP01(2024)005. arXiv: 2308.02449 [hep-ph].

[190] F. Hautmann et al. "A parton branching with transverse momentum dependent splitting functions". In: *Phys. Lett. B* 833 (2022), p. 137276. DOI: 10.1016/j.physletb.2022.137276. arXiv: 2205.15873 [hep-ph].

[191] John Collins, Ted C. Rogers and Nobuo Sato. "Positivity and renormalization of parton densities". In: *Phys. Rev. D* 105.7 (2022), p. 076010. DOI: 10.1103/PhysRevD.105.076010. arXiv: 2111.01170 [hep-ph].

[192] Alessandro Candido et al. "On the positivity of $\overline{\text{MS}}$ parton distributions". In: *Eur. Phys. J. C* 84.3 (2024), p. 335. DOI: 10.1140/epjc/s10052-024-12681-1. arXiv: 2308.00025 [hep-ph].

[193] Alessandro Candido, Stefano Forte and Felix Hekhorn. "Can $\overline{\text{MS}}$ parton distributions be negative?" In: *JHEP* 11 (2020), p. 129. DOI: 10.1007/JHEP11(2020)129. arXiv: 2006.07377 [hep-ph].

[194] S. Moch, J.A.M. Vermaseren and A. Vogt. "The longitudinal structure function at the third order". In: *Physics Letters B* 606.1–2 (Jan. 2005), pp. 123–129. ISSN: 0370-2693. DOI: 10.1016/j.physletb.2004.11.063. URL: http://dx.doi.org/10.1016/j.physletb.2004.11.063.